UCGE Reports
Number 20155

Ionosphere Weighted Global Positioning System Carrier Phase Ambiguity Resolution

(URL: http://www.geomatics.ucalgary.ca/links/GradTheses.html)

Department of Geomatics Engineering

By

George Chia Liu

December 2001

Calgary, Alberta, Canada

THE UNIVERSITY OF CALGARY

IONOSPHERE WEIGHTED GLOBAL POSITIONING SYSTEM CARRIER PHASE AMBIGUITY RESOLUTION

by

GEORGE CHIA LIU

A THESIS
SUBMITTED TO THE FACULTY OF GRADUATE STUDIES
IN PARTIAL FULFILLMENT OF THE REQUIREMENTS FOR THE
DEGREE OF MASTER OF SCIENCE

DEPARTMENT OF GEOMATICS ENGINEERING

CALGARY, ALBERTA
OCTOBER, 2001

Abstract

Integer Ambiguity constraint is essential in precise GPS positioning. The performance and reliability of the ambiguity resolution process are being hampered by the current culmination (Y2000) of the eleven-year solar cycle. The traditional approach to mitigate the high ionospheric effect has been either to reduce the inter-station separation or to form ionosphere-free observables. Neither is satisfactory: the first restricts the operating range, and the second no longer possesses the "integerness" of the ambiguities. A third generalized approach is introduced herein, whereby the zero ionosphere weight constraint, or *pseudo-observables*, with an appropriate weight is added to the Kalman Filter algorithm.

The weight can be tightly *fixed* yielding the model equivalence of an independent L1/L2 dual-band model. At the other extreme, an infinite *floated* weight gives the equivalence of an ionosphere-free model, yet perserves the ambiguity integerness. A stochastically tuned, or *weighted*, model provides a compromise between the two extremes. The reliability of ambiguity estimates relies on many factors, including an accurate functional model, a realistic stochastic model, and a subsequent efficient integer search algorithm. These are examined closely in this research.

Two days of selected Swedish GPS Network data sets from ionospherically active (up to 15 ppm) and moderate (up to 4 ppm) days, forming a maximum baseline length of 400 km, have been analyzed. All three ionosphere weight models yielded a 90% range of correct widelane ambiguities within three minutes, regardless of inter-

station distance.

Of the three ionospheric weighting schemes analyzed, the weighted model appears to be the optimal choice, with smaller instantaneous estimate errors and possessing the convergence characteristic. Upon parameter removal of the resolved widelane ambiguities, the precision of L1 ambiguity estimates improved between a few precent to 59 percent for baselines over one hundred kilometres. However, the improvement is not sufficient for resolving the L1 ambiguities.

Acknowledgements

First and foremost, I wish to thank many individuals at the Geomatics Department at the University of Calgary. Without the continuous encouragement and support from my supervisor, Professor G. Lachapelle, this thesis would not have been possible. Further gratitude extents to my colleague, Luiz-Paulo Fortes, and Dr. Susan Skone for many constructive discussions.

Second, I would like to thank Dr. Stefan Schaer at the Astronomical Institute at the University of Berne, for responding to many of my email questions related to ionosphere modelling. His prompt and unequivocal replies are much appreciated. I would also like to thank Professor Peter Teunissen at the Delft University of Technology for his valuable advise related to the integer ambiguity resolution and providing the Matlab version of the LAMBDA code.

Lastly, further acknowledgements extend to the Swedish National Geodetic Survey for providing the GPS data sets, the Onsala Astronomical Institute for the water vapour radiometer and meteorological data, the Scripps Institute of Oceanography for the orbit data, and the Astronomical Institute of the University of Berne for the Global Ionosphere Models.

Table of Contents

List of Tables

List of Figures

Notations

List of Acronyms

ADOP	Ambiguity Dilution of Precision.
AS	Anti-Spoofing.
BIM	Broadcast Ionosphere Model.
C/A-code	Coarse/Acquisition-code.
CODE	Centre for Orbit Determination in Europe, Astronomical Institute of the University of Berne, Switzerland.
DCB	differential code bias.
FARA	Fast Ambiguity Resolution Approach.
FASF	Fast Ambiguity Search Filter.
GIM	Global Ionosphere Map.
GPS	Global Positioning System.
IGS	International GPS Service.
IONEX	IONosphere Map EXchange Format.
LAMBDA	Least-squares AMBiguity Decorrelation Adjustment.
LC	Linear combination.
LT	Local Time.
MJD	Modified julian day.
P-code	Precise-code.
ppm	parts per million.
PRN	pseudo-random noise.
RINEX	Receiver INdependent EXchange Format.
RMS	root-mean-square.
SA	Selective Availability.
SIRF	Square-Root Information Filter.
SLM	Single-layer model.
SNR	Signal-to-Noise Ratio.
TEC	Total electron content.
TECU	Total electron content unit, $10^{16}m^{-2}$.
TID	Travelling Ionospheric Disturbance.
TZD	Total zenith delay.
UT	Universial time.
VTEC	Vertical total electron content.
WVR	Water vapour radiometer.
Y-code	Encrypted P-code.

List of Symbols

c	speed of light, 299792458.0 m/s.
L1	Link 1 carrier phase measurement in metre.
L2	Link 2 carrier phase measurement in metre.
L3	Ionosphere-free LC measurement in metre.
L4	Geometry-free LC measurement in metre.
H_k	Design matrix at epoch k.
I	Ionospheric delay in metres.
K_k	Kalman gain matrix at epoch k.
Kp	Global weighted index of geomagnetic fluctuations.
N_{L1}	L1 integer ambiguity, $\lambda_{L1} \approx 19.0$ cm.
N_{L2}	L2 integer ambiguity, $\lambda_{L2} \approx 24.4$ cm.
N_{NL}	NL integer ambiguity, $\lambda_{NL} \approx 10.7$ cm.
N_{WL}	WL integer ambiguity, $\lambda_{WL} \approx 86.2$ cm.
NL	Narrowlane.
P1	P-code measurement on L1 in metre.
P2	P-code measurement on L2 in metre.
P_r1	Reconstructed P1 in presence of AS.
P_r2	Reconstructed P2 in presence of AS.
P_k	(Co)variance of state vector.
Q_k	(Co)variance of system.
R_k	(Co)variance of measurements.
WL	Widelane.
v_k	Measurement error at epoch k.
w_k	System error at epoch k.
x_k	State vector at epoch k.
z_k	Measurement vector at epoch k.
Φ_k	State transition matrix at epoch k.
$[\ .\ ]_k^-$	Predicted $[\ .\ ]$ at epoch k.
β	Conversion scale factor from L2 ionospheric delay to L1, ≈ 1.647.
λ	Ambiguity wavelength.

List of Operators and Other Notations

$\mathbf{D}$	Double difference operator.
$\mathbf{R}$	(Co)variance matrix of measurements operator.
$\mathbf{W}$	Elevation weight operator.
∂	Jacobian operator.
$[\ .\ ]_i^k$	Zero difference between satellite k and receiver i.
$[\ .\ ]_i^{kl}$	Single difference between satellite k and l at receiver i.
$[\ .\ ]_{ij}^{kl}$	Double difference between k, l satellite pair and i, j receiver pair.

Chapter 1

Introduction

1.1 Background

The *NAVigation Satellite Timing And Ranging Global Positioning System* (NAVSTAR GPS) is a space-borne all-weather navigation system, developed and maintained by the U.S. Department of Defense (DoD). Its primary purpose is to provide position, velocity, and timing data for the U.S. and allied forces anywhere on or near the Earth, continuously. The U.S. Congress recognizes the economic potential and has allowed civilians to use this system with restrictions.

Since declared an operational system in 1994, civilian use has grown exponentially, in many applications, while the cost and size of a receiver has reduced significantly. The GPS technology has fostered an estimated eight billion U.S. dollars annual global market in related goods and services, and the growth was expected to double within two years after President Clinton's decision to deactivate the intentional degradation of civilian signal known as the *Selective Availability* (SA) (White House Press, 2000). Today, the GPS technology is becoming an integral component of the global information infrastructure with civilian benefits in transportation, emergency response, land management, recreational travel, space guidance, and timing. The benefits have prompted the GPS modernization program in which additional civilian signals will be incorporated into the next two generations of GPS satellites

(Sandhoo et al., 2000).

A nominal constellation of 24 GPS satellites orbit around the earth at an altitude of 20,200 km in six orbital planes inclined at 55 degrees with respect to the equator. This configuration provides a global coverage with four to eight simultaneously observable satellites 15 degrees above the local horizon. The orbital periods are approximately 11 hours 58 minutes, equivalent to a half sidereal day (Rothacher and Mervert, 1996). Each satellite provides a platform for various redundant equipment necessary for positioning that includes radio transceivers, computers, atomic clocks, solar panels, and a propellant system. The heart of the GPS satellite is the stable atomic clock from which all ranging measurements are derived.

GPS is a military system design for dual use. The *Standard Positioning Service* (SPS) offers better than 36 m horizontal and 77 m vertical accuracy standards at 95% for civilians, while the *Precision Positioning Service* (PPS) is limited to authorized users with complete access to the encrypted precise, P-code on both frequencies, *Link 1* (L1,f=1575.42 MHz) and *Link 2* (L2,f=1227.6 MHz) (DoD, 2001). GPS receiver manufacturers and the research community have devised techniques to access the P-code and algorithms to exploit the millimetre accuracy of carrier phase measurements.

The ultimate attainable accuracy from GPS is at the centimetre level or better by using the interferometry approach provided that the integer carrier-phase cycle biases (commonly referred to the cycle ambiguities) can be resolved and constrained.

The natural wavelengths of the L1 and L2 signals are $\lambda_{L1} \approx 19$ cm and $\lambda_{L2} \approx 24$ cm. Because of their narrow wavelengths, direct and instantaneous estimation of these biases using the code range measurements is not possible. The traditional approach had been long static occupation allowing time for the ambiguities to converge to near integers. Typical occupation time can be hours, depending on baseline length and atmospheric conditions, and is far too restrictive for many applications, notably for kinematic platform positioning. An artificial observable, *widelane* (WL) with much wider wavelength, $\lambda_{WN} \approx 86$ cm, can be generated by linear combination of the two fundamental frequencies to help near-instant ambiguity resolution at the cost of induced noise level to the position estimates by almost six times that of fixed L1 solution.

Current precise L1 ambiguity fixed *Real-Time Kinematic* (RTK) positioning is restricted to ranges of up to several kilometres from a single reference station, due to the build up of distance-dependent atmospheric errors. Recent developments of a multi-reference approach has shown a consistent reduction of residual errors of up to 60% in code and phase measurements in Norway (Raquet et al., 1998), Canada (Fortes et al., 2000a), Brazil (Fortes et al., 2000b), and Japan (Lachapelle et al., 2000).

The sunspot number is directly related to the heightened solar activities. The Norway Experiment was conducted in late September of 1997 near the beginning of Sunspot Cycle Number 23 under a low ionosphere activity period (Figure 1.1). The widelane ambiguities were successfully resolved at above 90-percentile for baselines

up to 220 km. However, the success rate dropped drastically under active ionosphere conditions in Brazil located near the equatorial anomaly region in August, 1999 during the proximity of the solar maximum. The widelane ambiguity resolution success rate dropped to about 60-percentile for baselines between 100 km and 200 km. The likely contributing factor for the poor performance may be that the rapid fluctuations of the *Total Electron Content* (TEC), commonly referred to as scintillation, present along the signal path can induce white noise characteristics in the user's measurements, and may not be deterministically modelled by a network of reference stations.

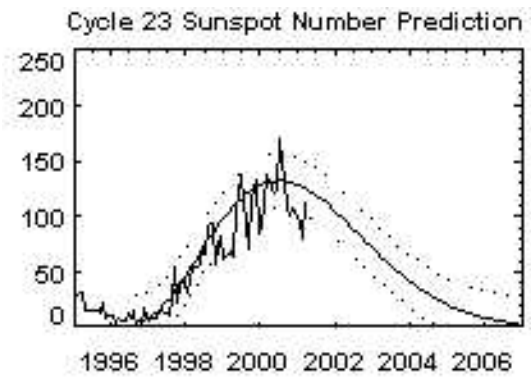

Figure 1.1: Current Sunspot Cycle Number 23 (NASA, 2001)

1.2 Motivation

The GPS ambiguity resolution process is in fact composed of two parts: the mathematical modelling, and the integer search. Ambiguities are all first estimated as real values by a mathematical representation of the functional and stochastic models.

And the success of the integer ambiguity search is much dependent on the statistical reliability of the estimated real values obtained from the first part.

The presently available *On-the-Fly* (OTF) ambiguity search capability required by centimetre-level kinematic surveying is restricted to about several km due to an insufficient mathematical model accounting for the buildup of differential ionosphere error as we are near the peak of the 11-year cycle, and to a lesser extent the residual differential troposphere error. The inclusion of an ionosphere parameter and its associated stochastic behaviour are usually present in all sophisticated algorithms that are capable of resolving ambiguities over several hundreds of km (Bock et al., 1986; Blewitt, 1989; Mervart, 1995). The typical strategy employed is a two-step bootstrap operation: 1)widelane ambiguities search, and 2) constraining the widelane integer (N_{WL}) ambiguity for the subsequent *Narrow-Lane* (NL) integer (N_{NL}) ambiguity search. The N_{WL} search is performed first because of its higher success probability due to the 86.2 cm wavelength versus NL's 10.7 cm. Both L1 and L2 ambiguities can be derived arithmetically once both N_{WL} and N_{NL} ambiguities are found. Bock (ibid) suggests introducing a white-noise model with appropriate distance-dependent stochastic weighting to represent each double difference ionosphere parameter during the first N_{WL} search step, then discarding it in the second step when the *ionosphere-free* (L3) observables are introduced. The *Quasi-Ionosphere-Free* (QIF) approach proposed by Mervart resolves the L1 and L2 ambiguities directly using the L3 observables. The search looks for the combination of N_{L1} and N_{L2} integer candidates that best match the real narrow-lane ambiguity values. Unfortunately, all the algorithms mentioned are intended for geodynamic research applications with static

occupations that can extend for hours or days. The long occupation time enables the higher noise level of ionosphere-free (L3), $\sigma_{L3} \approx 3\sigma_{L1}$ observables to resolve the 10.7 cm narrow-lane ambiguities.

A wealth of research has been focused on the ambiguity search with OTF capability, and there seems no standard procedure for integer search algorithms. Invariably, all search criteria are based on integer least-squares with one of or a combination of many optimization strategies. The *Fast Ambiguity Search Filter* (FASF) uses a recursive computation process to reduce the search space and performs parameter removal once an integer is found (Chen, 1994). The *Least-squares Ambiguity Search Technique* (LAST) only searches for a subset of integers to reduce the computational burden, and the remaining integers are computed based on the integer estimates of the primary set (Hatch, 1990). The sequential *Square-Root Information Filter* (SRIF) optimizes the search time through Cholesky factorization (Landau and Euler, 1992). The *Least-squares AMBiguity Decorrelation and Adjustment* (LAMBDA) is a two-step process where the decorrelation transformation is applied to the variance-covariance matrix of ambiguities, and then the integers are searched through conditional least-squares in hyper-ellipsoidal space, rather than in cubic space (Teunissen, 1995; deJong and Tiberius, 1996).

The inclusion of an ionosphere parameter is seldom found in kinematic GPS software packages that require a near-instant ambiguity resolution capability. A recent publication has claimed successful fast L1 ambiguity resolution over a single 100 km baseline using a very limited and cycle-slip free sample of one hour at 30 seconds data

set, in conjunction with precise orbits (Odijk, 1999). The success can be attributed to the inclusion of a white-noise ionosphere model in the algorithm by introducing zero pseudo-observations with associated stochastic weighting. Ambiguities were successfully resolved within 7.5 minutes in eight independent runs. The observations consist of dual-band carrier phase and P-code measurements. The ambiguities were resolved using the LAMBDA algorithms.

1.3 Objectives

This thesis investigates the impact on fast ambiguity resolution performance, both for N_{L1} and N_{WL} ambiguities, by introducing weighted pseudo-observations to model the ionosphere delay under low and high conditions over the *Swedish GPS Network*, known as the SWEPOS (Figure 1.2). The SWEPOS network comprises 25 stations, each equipped with two geodetic quality Ashtech Z-XII dual frequency GPS receivers sharing a common *International GPS Service* (IGS) standard chokering antenna equipped with a Dorne Margolin element. The SWEPOS network is chosen for the research because of its relatively dense network, with inter-station separations not exceeding 160 km, and the availability of dual-band carrier phase and reconstructed P-code measurements at 1 Hz. These are all well suitable for fast ambiguity resolution.

Two days (April 7 and June 21, 2000) of GPS data observed during high and low ionosphere activities are selected for the analysis (Figure 1.3). The Kp index

Figure 1.2: Swedish SWEPOS Network (SWEPOS, 2001)

is a 3-hour planetary geomagnetic index of activity generated from the 12 or 13 global magnetometer stations, with most of the observatories located in the Northern Hemisphere. The level of ionosphere activity is directly related to the dynamics of the free electron content in the upper atmosphere and is detectable by the surface magnetometers. The Kp index is a measure of global geomagnetic activity; therefore it may not register localized disturbances. Kp indices of below and above 4 are considered as low and high activities, respectively. The indices for April 7 are extremely

high at Kp indices up to 8, while for June 21, the Kp indices are below 3 (NOAA, 2001).

Presently, the software packages available at the Geomatics Department do not include the ionosphere parameter and the dual-band carrier phase measurements are not simultaneously included in the observation model. Because of these shortcomings, it was decided to develop a true dual-frequency prototype software package capable of accommodating ionosphere parameters in order to stochastically model white-noise ionosphere characteristics, and capable of resolving N_{L1} and N_{WL} ambiguities using sequential filtering and LAMBDA decorrelation and search algorithms.

1.4 Outline

- Chapter 2 provides an overview of the GPS signal structure, receiver designs, and tracking techniques under normal and SA conditions. It also provides an overview of the fundamental observation models, and introduces various linearly combined artificial observations that can be formed.

- Chapter 3 focuses on atmosphere delay modelling. It describes the two currently available ionosphere models: 1) the eight parameter Broadcast Ionosphere Model (BIM) coefficients present in the broadcast orbit message, and 2) the *Global Ionosphere Map* (GIM) provided by the IGS and computed from the global GPS tracking network. Some of the troposphere delay models are discussed.

- Chapter 4 describes the implemented algorithms used in this analysis. An overview of Kalman Filter algorithms is provided. Proper treatment of non-linear mathematical functions for a faster solution convergence is discussed. An overview of the LAMBDA ambiguity decorrelation and search algorithms is provided.

- Chapter 5 investigates the stochastic characteristics of the observables such as the elevation and distance dependence, the cross-measurement correlation, and the time correlation. It is often assumed that GPS measurements are statistically independent, and this is far from truth under AS conditions. A strong cross-correlation is detected between the L1 and L2 phase measurements, as a result of codeless/semi-codeless tracking techniques. Lastly, the chapter examines the double difference ionosphere and residual troposphere delay errors as a function of distance.

- Chapter 6 presents the impact of incorporating a stochastic ionosphere model on ambiguity resolution performance, both in N_{L1} and N_{WL}, over various baseline lengths under quiet and active ionosphere conditions. It will also investigate the effect on position and N_{L1} ambiguity estimates by constraining the N_{WL}, and the effect on position estimates by applying the integer constrained ionosphere-free (L3) observables.

- And lastly, Chapter 7 provides the conclusions and recommendations.

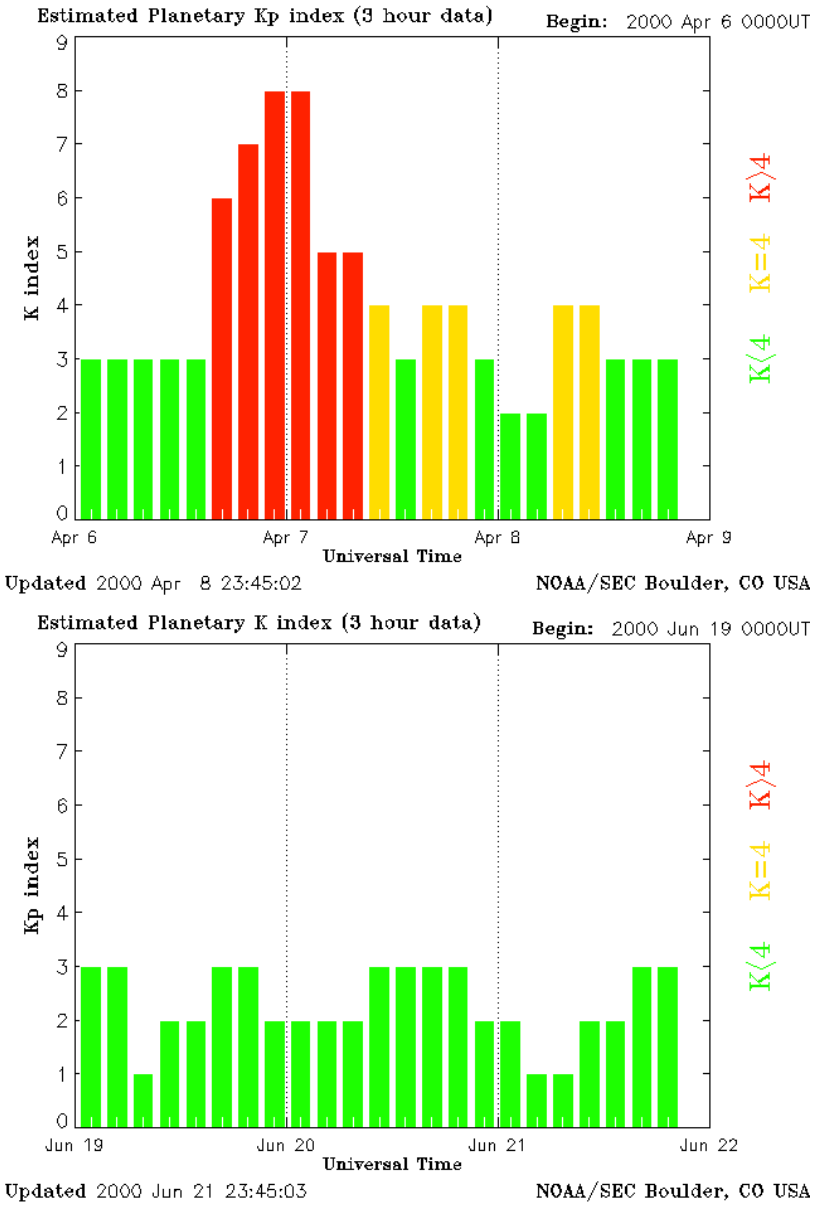

Figure 1.3: Kp Indices, April 7 and June 21 2000 (NOAA, 2001)

Chapter 2

GPS Signals, Observables, and Errors

2.1 Signal Structure

The current operational Block II and IIR satellites transmit a complex radio signal centered on two frequencies, L1 ($f_{L1} = 1575.45$ MHz) and L2 ($f_{L2} = 1226.60$ MHz). Both are located within a portion of the L band reserved for satellite-based positioning systems set aside by the International Telecommunications Union. Transmitting radio signals at these frequencies is a compromise between ionosphere dispersion and *space-loss*. Dispersion is inversely proportional to the square of the radio frequency, while the dB signal loss due to space loss is exponentially related. Single frequency users will experience up to 30 m of range delay at zenith on L1 during night time, and a small portable antenna is sufficient to track both GPS L1 and L2 signals. The separation between selected frequencies is sufficiently wide for dual frequency users to remove the first-order ionosphere dispersion effect accounting for 99% and narrow enough that only a single receiving antenna is needed (Langley, 1998a).

GPS is a one-way ranging system, that is, GPS signals are passively transmitted from satellites to an unlimited number of users. The L1 and L2 carriers are pure sinusoidal waves, which by themselves are not sufficient to fix a position in real-time because of the ambiguous phase cycles and unknown satellite positions. Therefore, additional signals are multiplexed on two L1/L2 carriers using the *binary biphase*

modulation technique and spread out over a bandwidth of 20 MHz for direct ranging and positioning. Modulated signals are the *precise-code* (P-code), and coarse ranging information *coarse/acquisition-code* (C/A-code). The ranging data are in a binary sequence of *pseudo-random numbers* (PRN) generated by mathematical algorithms present in hardware device referred as the *tapped feedback registers*. Although the sequence appears random, a receiver can duplicate it. All GPS satellites transmit signals on the same L1/L2 frequencies. And each individual PRN signal is orthogonal to each other and can be extracted using the *Code Division Multiple Access* (CDMA) technique that relies on the strong auto-correlation properties (Spilker, 1996).

The C/A-code sequence has a chip length of 1,023 bits at a clock rate of 1.023 MHz, and repeats itself every 1 ms. The C/A-code sequence is unique for each satellite. In contrast, the P-code sequence has a chip length of 15,345,000 bits at a clock rate of 10.23 MHz that does not repeat itself for 266.4 days. Each satellite shares the same P-code sequence, but each is assigned with a one-week segment. The faster clock rate of P-code provides better resolution than the C/A-code by a factor of 10. Using a standard code correlation technique found in most receivers provides standard deviations of typically 1 m for the C/A-code and 0.1 m for the P-code. The broadcast message contains the satellite orbit ephemeris, constellation almanac, satellite clock corrections, satellite status, and ionosphere corrections. The message is transmitted at 50 bps data stream added to the C/A-code and P-code using a modulo-2 addition and requires 30 seconds to complete the transmission of information necessary for an initial position fix. However, a complete message requires 12.5 minutes to transmit.

The L1 carrier wave is multiplexed with two spread spectrum C/A-code and P-code signals through *phase-quadrature*, where the C/A-code is modulated on the in-phase component of the L1 carrier, while the P-code is modulated on a 90 degrees rotated quadrature phase. Only the P-code is modulated on the L2 carrier wave. Current activation of *Anti-Spoofing* (AS) denies civilian access to the P-code by encrypting it with an additional secret W-code sequence. The resultant sequence is referred as the Y-code. The resultant L1 and L2 signals, S_{L1} and S_{L2}, can be represented by:

$$S_{L1}(t) = A_{Y,L1}Y(t)D(t)cos(\omega_1 t + \phi_{L1}) + A_C C(t)D(t)sin(\omega_1 t + \phi_{L1}) \tag{2.1}$$

$$S_{L2}(t) = A_{Y,L2}Y(t)D(t)cos(\omega_2 t + \phi_{L2}) \tag{2.2}$$

where, $A_{Y,L1}$ and $A_{Y,L2}$ are the respective L1 and L2 amplitudes of the encrypted P(Y)-code; A_C is the amplitude of C/A-code; $D(t)$ is the broadcast message; $Y(t) = P(t)W(t)$ is the encrypted Y-code sequence; $C(t)$ is the C/A-code sequence; $D(t)$ is the broadcast message sequence; $\omega_{L1,L2}$ is the L1 or L2 frequency; and $\phi_{L2,L2}$ is the L1 or L2 phase noise error. The synthesis of the GPS signals is best described by Figure 2.1.

In order to deny full system accuracy for non-authorized users, the U.S. Dept. of Defense officially implemented the *Selective Availability* (SA) in 1990 by applying errors in the broadcast orbit parameters and dithering the satellite clock frequency. The SA was officially turned off on May 2, 2000, by the Presidential Decision Directive to make GPS more responsive to civil and commercial users worldwide. Figure

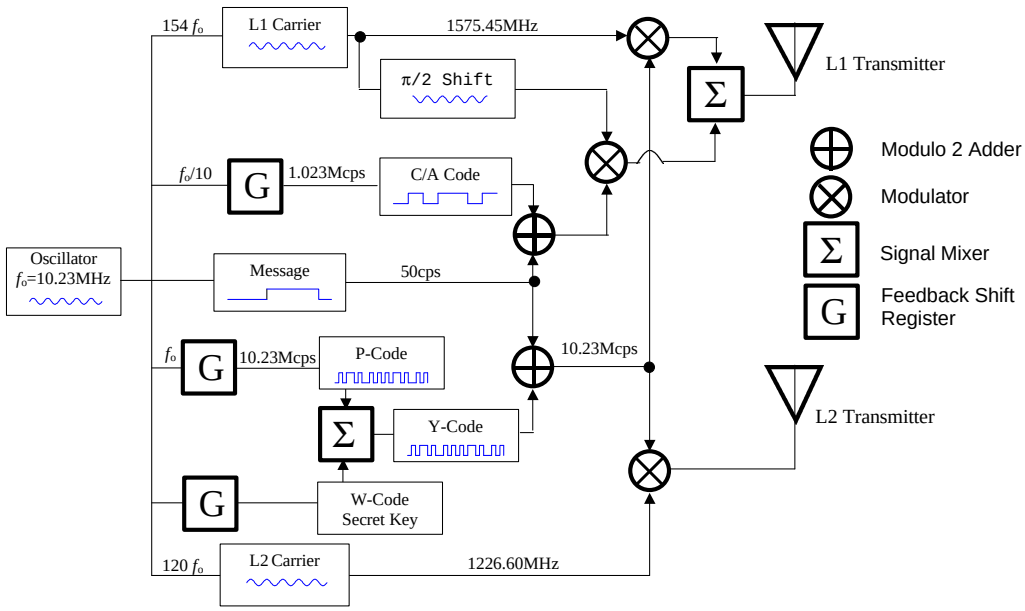

Figure 2.1: GPS Signal Structure

2.2 illustrates the effect of SA on single-point positioning at Station Onsala over one hour at 1 Hz. The GPS receiver is equipped with an external hydrogen maser clock reference. The figures on the top and bottom rows are based on precise orbit and ionosphere-free P-code measurements taken on Sept 16, 1998, and June 21, 2000, respectively. The range error plots shown on the right column are the observed ranges minus the true ranges adjusted with the computed GPS receiver clock offsets. The range derived from the precise orbit and published station position is considered as

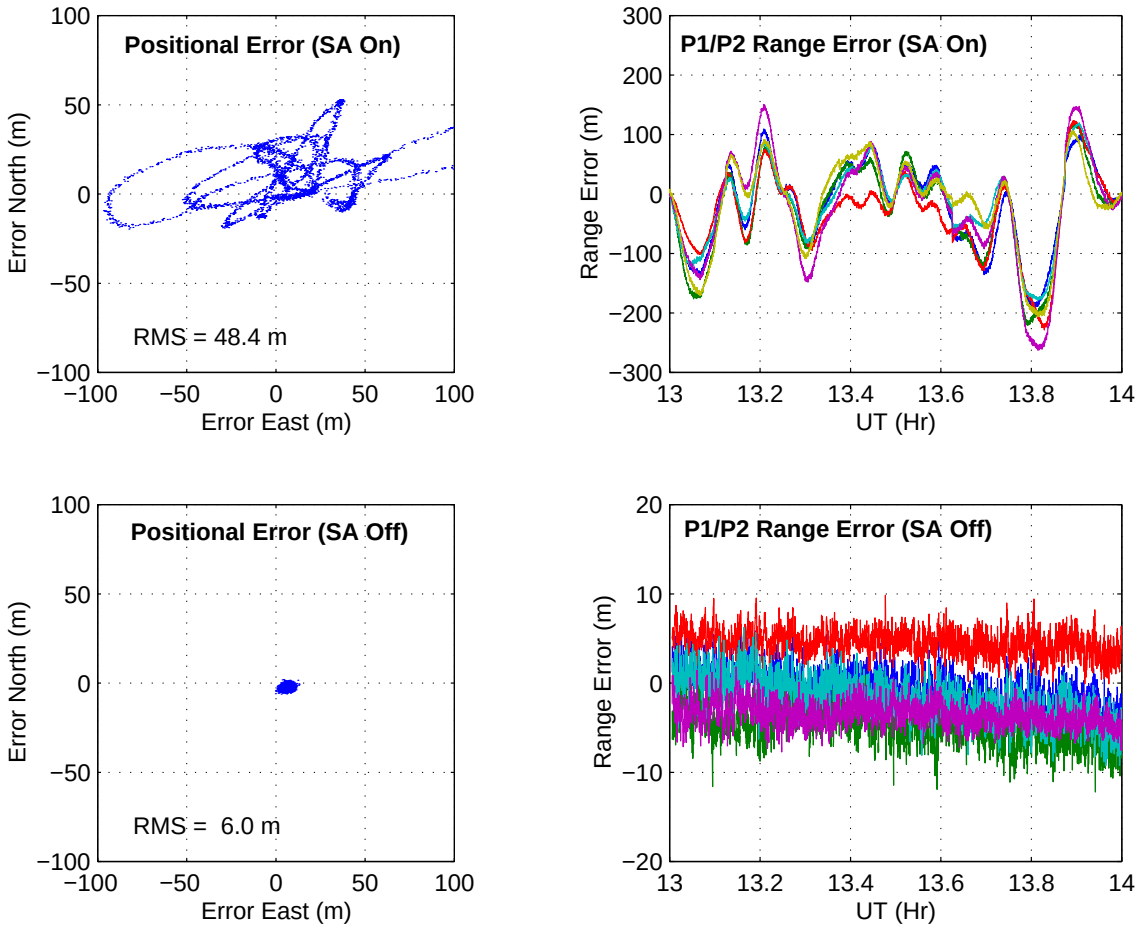

Figure 2.2: SA Effect on Position and Range

the true range.

2.2 Signal Processing

The fundamental purpose of GPS receiver hardware is the extraction of ranges, reconstruction of the carrier phase, and decoding of the broadcast message, all from

the electromagnetic energy transmitted from the orbiting satellites at 20,200 km altitudes. Specifically, the range measurements are the time offsets between the receiver generated and incoming PRN binary sequences, and the carrier phase measurements are the subsequent reconstructed carrier waves after the modulated PRN codes are removed. Under the current AS environment, direct matching of Y-code and reconstruction of L2 carrier phase, can't be done directly by unauthorized users. Many manufacturers, however, have devised a number of tracking techniques to indirectly access the restricted signals with a variable level of performance. A GPS unit includes the following components: Antenna, RF Section, Microprocessor, Control Device, Storage Device, and Power Supply. The attainable measurement accuracy is a result of the signal propagation environment and the hardware design. The next two subsections detail the Antenna and various tracking techniques in the RF Section that affect the measurement performance.

2.2.1 Antenna

The antenna element, tuned to the exact GPS frequencies, absorbs, resonates and converts the incoming electromagnetic energy to electrical current that can be processed by the electronic components. There are many element types: monopole, dipole, quadrifilar helices, spiral helices, slots, and microstrips. The most common type, microstrip, has a circular or square metallic patch printed on a circuit board.

Multipath is one of the common sources of error in GPS measurement. The phenomenon occurs when one or multiple reflected signals arrive at antenna resulting

in the corruption of pseudorange and/or carrier phase measurements. There are a number of ways to mitigate the effect. One way is to avoid placing antenna near reflective objects. Using a ground plane can effectively shade the ground reflected rays arriving at the antenna. A ground plane can simply be a flat metallic material, or a multiple concentric rings spaced by an even fraction of a wavelength to choke off the reflective rays arriving laterally. The later is referred as the *chokering* ground plane. Another way to mitigate the effect is through antenna design. The antenna gain pattern can be shaped such that little or no antenna gain exists near the horizon where the multipath is much more dominant. The incoming GPS signal is *right-hand circular polarized* (RHCP), and the single reflected rays have the polarization reversed to LHCP. An antenna can be designed to optimize the axial ratio to discriminate and reject the reverse polarized rays. Multipath can be further rejected in the *delay-lock loop* DLL (see below) using the narrow correlator and wide precorrelation bandwidth (Van Dierendonck, 1996).

For the millimetre high precision, such as in deformation and geodynamic applications, the stability of the phase centre is critical, and its directional dependence can be modelled. As well, L1 and L2 phase centres are not co-incidental in most antenna designs as a result of separate elements being used. Therefore, the calibrated phase centre positions need to be accounted for during the data processing. One recent innovative antenna design has the microstrip patch printed in a spiral shape with the successive whirls tuned to the L1 and L2 frequencies (Kunysz, 1999). As a result, both phase centres are identical, and such a characteristic is ideal for a mobile platform.

2.2.2 RF Section

All precision GPS receivers today have a dedicated channel for tracking each satellite per frequency. Geodetic quality receivers today have as many as 24 channels, capable of tracking 12 dual-band satellite signals continuously with wide dynamics. All incoming GPS signals arrive on the same L1/L2 frequencies, and separating individual PRN code from an ensemble of signals is possible by the *delay loop lock* (DLL) that cross-correlates each replica code generated by the receiver. With the introduction of the narrow-correlator C/A-code tracking technique, where the spacing between the early and late correlation is narrowed to 0.05 chip length, the accuracy has improved to the level of P-code measurements (Van Dierendonck et al., 1992). The time shift between the two sequences, scaled by the speed of light, yields the spatial range between the receiver and the transmitting satellite. However, the measured distance is time biased due to the different clock references used by the transmitter and the receiver. As a result, the measured range is referred to as the *pseudorange*. After stripping away the modulated PRN, the broadcast message is decoded through a high-pass filter. After the removal of modulation, the Doppler-shifted carrier phase is sent to the *phase lock loop* (PLL), where both complete and fractions of carrier measurements are made (Langley, 1991).

Direct cross-correlation of the Y-code, either on L1 or L2, and the reconstruction of the L2 carrier phase are not possible under current AS activation. GPS receiver manufacturers offer ways to circumvent the encrypted PRN code with a variable

degree of signal strength loss.

The earliest approach found in the first generation of geodetic quality receiver, i.e. Micrometer (Counselman and Gourevitch, 1981) was the *squaring* technique. The L2 carrier phase is mixed by itself through squaring. The resultant wave is a pure L2 carrier free of modulation, with doubled wavelength and *signal-to-noise ratio* (SNR) degradation of 30 dB. The halved L2 wavelength, $\lambda_{L2} = 24.4/2 = 12.2$ cm significantly increases the multi-dimensional ambiguity search space; hence, decreases the probability of success.

The *cross-correlation* technique is based on the fact the encrypted code on both L1 and L2 are identical. The pseudorange is extracted by determining the relative time shift from the cross-correlation function with respect to L1. The L2 carrier is reconstructed in a similar manner from the beat frequency carrier. The propagation delay experienced by both will not be the same depending on the ionosphere conditions that need to be adjusted. The tracking degrades drastically in high ionosphere conditions, as reported in the equatorial regions. One clear advantage here is that the whole wavelength is preserved and the stronger L1 SNR signal is optimized. However, a degradation of 27dB exists as compared to the direct code correlation technique.

Two additional techniques, based on variations of the squaring and cross-correlating described above, are termed *semi-codeless squaring* and *semi-codeless cross-correlation*. The encrypted Y-code is a composite of known P-code and the secrete W-code.

Knowing the approximate chipping rate for the W-code permits the narrowing of predetection bandwidth to 500 KHz. A receiver can indirectly track the Y-code by cross-correlating the generated P-code using predetection bandwidth of 500 KHz, instead of 50 Hz in direct P-code cross-correlation. Narrower predetection bandwidth minimizes measurement noise. Either squaring the signal itself or cross-correlating between dual-band signals accomplishes the subsequent reconstruction of L2 carrier. As in any squaring technique, the modulation is removed and the wavelength is halved, but signal degradation is 17 dB (Van Dierendonck, 1994). The semi-codeless correlation is the most effective tracking technique under the presence of AS, with signal degradation of 14 dB. It is the technique employed in Ashtech Z-XII GPS receiver, under the trademark, Z-tracking^{TM} (Ashjaee and Lorenz, 1993). According to Ashtech, the definition of Z-tracking is,

> "Ashtech's proprietary (patented) process for mitigating or eliminating the effects of DoD Anti-Spoofing (AS) and thereby retaining receiver lock and tracking capability at all times on the satellites in view. This technique separately matches the Y-Code on L1 and L2 against a different, locally generated P-Code, a correlation that exposes the encrypting code on each frequency. Both carriers also contain the encrypting code, hence with sufficient signal integration the encrypting signal bit is estimated for L1 and L2 and each is fed to the other frequency, thus removing the encrypting code from each carrier frequency, which can then be measured."

2.3 GPS Observation Models

2.3.1 Fundamental GPS Observation Equations

$$P_i^k = \rho_i^k + c(\Delta t_i - \Delta t^k) + c(b^k + b_i) + \Delta\rho_{i,trop}^k + \Delta\rho_{i,ion}^k + \Delta\rho_{i,orbit}^k + \Delta\rho_{i,mpP}^k + \epsilon_P \quad (2.3)$$

$$L_i^k = \rho_i^k + c(\Delta t_i - \Delta t^k) + \lambda B_i^k + \Delta\rho_{i,trop}^k - \Delta\rho_{i,ion}^k + \Delta\rho_{i,orbit}^k + \Delta\rho_{i,mpL}^k + \epsilon_L \quad (2.4)$$

where,

P_i^k is the code measurement between receiver, i, and satellite, k, either C/A-code, P-code on L1, or on L2 (m),

L_i^k is either the L1 or L2 carrier phase measurement (m),

ρ_i^k is the geometrical distance (m),

c is speed of light constant (m/s),

Δt_i and Δt^k are clock offsets (s),

$\Delta\rho_{i,trop}^k$ is geometrical signal delay due to the troposphere (m),

$\Delta\rho_{i,ion}^k$ is geometrical signal delay due to the ionosphere (m),

$\Delta\rho_{i,orbit}^k$ is geometrical orbital error (m),

$\Delta\rho_{i,mpP}^k$ is code multipath error (m),

$\Delta\rho_{i,mpL}^k$ is carrier phase multipath error (m),

b^k and b_i are the receiver and satellite hardware delay biases (s),

ϵ_P is the code measurement noise (m),

ϵ_L is the carrier phase measurement noise (m),

λ is carrier phase wavelength (m/cycle), and,

B_i^k is the initial carrier phase bias (cycle).

For brevity, the multipath effects and the measurement noise are assumed to be

zero. The remaining geometrical terms, such as the clock, tropospheric delay, and the orbital error, are grouped according to

$$\rho_i'^k = \rho_i^k + \underbrace{c(\Delta t_i - \Delta t^k) + \Delta\rho_{i,trop}^k + \Delta\rho_{i,orbit}^k}_{\Delta\rho_{i,geom}^k} \tag{2.5}$$

And, the fundamental observables in metres are reduced to

$$L_{i,1}^k = \rho_i'^k - I_i^k + \lambda_{L1} B_{i,1}^k \tag{2.6}$$

$$L_{i,2}^k = \rho_i'^k - \xi I_i^k + \lambda_{L2} B_{i,2}^k \tag{2.7}$$

$$P_{i,1}^k = \rho_i'^k + I_i^k + c(b^{k,1} + b_{i,1}) \tag{2.8}$$

$$P_{i,2}^k = \rho_i'^k + \xi I_i^k + c(b^{k,2} + b_{i,2}) \tag{2.9}$$

where,

superscript k and subscript i refer to between satellite k and station i, $L_{i,1}^k, L_{i,2}^k$ are the carrier phase measurements on L1 and L2 (m),

$P_{i,1}^k$ is either the C/A or P-code measurements on L1 (m),

$P_{i,2}^k$ is the P-code measurements on L2 (m),

c is speed of light constant (m/s),

$\rho_i'^k$ is the geometrical distance including all geometrical errors (Equation 2.5) (m),

ξ is the scale factor for converting from L2 ionosphere delay to L1 ($\xi = f_1^2/f_2^2 \approx 1.647$) (unitless),

I is the ionosphere delay, $\Delta\rho_{i,ion}^k$, referenced to L1 (m),

$B_{i,1}^k, B_{i,2}^k$ are the respective carrier phase biases on L1 and L2 (cycle),

$b^{k,1}, b^{k,2}$ are the respective L1 and L2 satellite hardware biases (s), and,

$b_{i,1}, b_{i,2}$ are the respective L1 and L2 receiver hardware biases (s).

Note that the ionosphere effect causes the carrier phase propagation to advance and the code signal to be delayed. Their magnitudes are identical with opposite sign. Strictly, the bias terms, $B^k_{i,1,2}$ are actually non-integer quantities as they contain the hardware biases and the phase windup effect, i.e. $B^k_i = \lambda(N^k_i + \delta N^k_i) + c(b^k + b_i)$, and the integer nature of N^k_i can't be extracted unless the measurements are differenced (Schaer, 1999). The circularly polarized carrier wave experiences the *Faraday Rotation*, δN, as it travels through the ionosphere, which results in a minute phase shift. The amount of rotation at 1 GHz level is below the carrier phase measurement noise, less than a tenth of a millimetre according to following equation and can be neglected:

$$\delta N = \frac{kB_L TEC}{f^2} \tag{2.10}$$

where, δN is the rotation in radians, B_L is the mean longitudinal magnetic field intensity at mean ionospheric height usually taken at 400 km in unit of nT, k is a constant at 2.36E-5, and *Total Electron Density* (TEC) in unit of electrons/m^2.

2.3.2 Forming Differences

Single Difference can either be taken between two satellites or between two receivers. And it can be applied to both carrier and code measurements. The result of single difference is the elimination of systematic biases, either the satellite clock and satellite hardware biases if differencing between receivers i and j, or the receiver clock and receiver hardware biases, if differencing between a satellite pair, k and l. Single difference between a receiver pair also reduces the orbital and atmospheric

errors.

$$L_{i,j}^{k} = L_{i}^{k} - L_{j}^{k} \tag{2.11}$$

$$P_{i,j}^{k} = P_{i}^{k} - P_{j}^{k} \tag{2.12}$$

Double Difference between two single difference observables with common base satellite and base receiver, results in an effective elimination of all systematic clock and hardware biases. The cycle ambiguity terms become, or very close to, integer quantities, i.e. $B_{ij,1,2}^{kl} \Rightarrow N_{ij,1,2}^{kl}$. Figure 2.3 illustrates one double difference observable between satellite and station pairs.

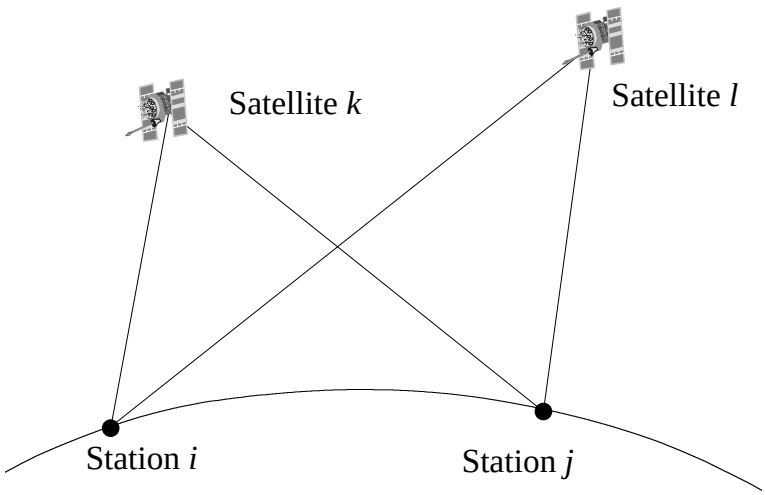

Figure 2.3: Double Difference

$$L_{ij}^{kl} = L_{ij}^{k} - L_{ij}^{l} \tag{2.13}$$

$$P_{ij}^{kl} = P_{ij}^{k} - P_{ij}^{l} \tag{2.14}$$

$$L_{ij,1}^{kl} = \rho_{ij}^{\prime kl} - I_{ij}^{kl} + \lambda_{L1} N_{ij,1}^{kl} \tag{2.15}$$

$$L_{ij,2}^{kl} = \rho_{ij}^{\prime kl} - \xi I_{ij}^{kl} + \lambda_{L2} N_{ij,2}^{kl} \tag{2.16}$$

$$P_{ij,1}^{kl} = \rho_{ij}^{\prime kl} + I_{ij}^{kl} \tag{2.17}$$

$$P_{ij,2}^{kl} = \rho_{ij}^{\prime kl} + \xi I_{ij}^{kl} \tag{2.18}$$

The troposphere delay is spatially dependent, with more sensitivity in the vertical component, and directionally dependent with respect to the ray path. The bulk of the effect can be removed using one of the many troposphere models in conjunction with surface meteorological measurements or from a standard set. However, the residual error will be present, in addition to the residual orbital errors. The double difference geometrical range, Equation 2.5, simplies to, $\rho_{ij}^{\prime kl} = \rho_{ij}^{kl} + \delta T_{ij}^{kl}$.

2.3.3 Linearly Combined Observations

Various artificial observations can be formed from dual-frequency observations through *linear combination* (LC) by applying the following equation:

$$LC = \kappa_1 L1 + \kappa_2 L2 \tag{2.19}$$

Each LC observation has its own unique characteristics with respect to wavelength and sensitivity to troposphere and ionosphere delay effects and is useful in certain applications. While an infinite number of LC observations can be formed, the most common three LC are: the *ionosphere-free* (L3) that removes the first-order dispersive ionosphere effect and is particularly useful in troposphere delay estimation; the *geometry-free* (L4) that removes all the geometrical errors including the troposphere, orbital, and clock offset errors, and is useful for ionosphere delay estimations; and, the widelane (WL) with wavelength of 86 cm eases the cycle ambiguity process.

The ability to form these various LC observations makes a dual-frequency receiver much more powerful than a single-frequency unit, both in ambiguity resolution and in accuracy performance over longer baselines.

There are drawbacks with the LC observations. One is the induced measurement noise that is a direct consequence of combining two fundamental observations, L1 and L2. Another is the possible loss of integer nature of the ambiguities, depending on κ_1 and κ_2 coefficients employed.

Ionosphere-Free Linear Combination (L3) removes the ionospheric effect. Its double difference form can be expressed in unit of metres by the following:

$$\begin{aligned} L_{ij,3}^{kl} &= \kappa_{1,3} L_{ij,1}^{kl} + \kappa_{2,3} L_{ij,2}^{kl} && (2.20) \\ &= \rho_{ij}^{'kl} + B_{ij,3}^{kl} && (2.21) \\ P_{ij,3}^{kl} &= \kappa_{1,3} P_{ij,1}^{kl} + \kappa_{2,3} P_{ij,2}^{kl} && (2.22) \\ &= \rho_{ij}^{'kl} && (2.23) \end{aligned}$$

where the dimensionless constants,

$$\kappa_{1,3} = +\frac{f_1^2}{f_1^2 - f_2^2} \approx +2.546 \quad (2.24)$$

$$\kappa_{2,3} = -\frac{f_2^2}{f_1^2 - f_2^2} \approx -1.546 \quad (2.25)$$

$B_{ij,3}^{kl}$ is a real number in unit of metres and can't be expressed in form of λN. It has a numerical equivalence of

$$B_{ij,L3}^{kl} = \kappa_{1,3} \lambda_{L1} N_{ij,L1}^{kl} + \kappa_{2,3} \lambda_{L2} N_{ij,L2}^{kl} \quad (2.26)$$

Geometry-Free Linear Combination (L4) is completely free of geometrical terms as shown in Equation 2.5 that includes the geometrical range between the satellite and the receiver, clock offsets, and the troposphere delay. This LC does not require the orbital information when processing. However, the undifferenced observation, often known as *one-way* and used in global ionosphere modelling, will contain the so-called *differential code bias* (DCB) error terms and is simultaneously estimated along with ionosphere delay. DCB is the inherent hardware interfrequency biases between L1 and L2 signals that are present in both satellites and receivers. The level of DCB in the satellites is typically at the ±3 ns. And a receiver, the Turbo Rogue SNR8000 for example, has a level of ±10 ns (Wilson and Mannucci, 1993). The undifferenced geomtry-free L4 and P4 LC are expressed by the following equations in unit of metres:

$$L^k_{i,4} = \kappa_{1,4} L^k_{i,1} + \kappa_{2,4} L^k_{i,2} \tag{2.27}$$

$$= -\xi_4 I^k_i + B^k_{1,4} \tag{2.28}$$

$$P^k_{i,4} = \kappa_{1,4} P^k_{i,1} + \kappa_{2,4} P^k_{i,2} \tag{2.29}$$

$$= +\xi_4 I^k_i + c(\Delta b^k - \Delta b_i) \tag{2.30}$$

where,

the coefficients are $\kappa_{1,4} = +1$ and $\kappa_{2,4} = -1$ (unitless),

the bias term is $B^k_{1,4} = \lambda_{L1} B^k_{i,1} - \lambda_{L2} B^k_{1,2}$,

Δb^k is the satellite DCB between L1 and L2 (s),

Δb_i is the receiver DCB between L1 and L2 (s),

I is the ionosphere delay referenced to L1 (m), and

the constant is $\xi_4 = 1 - f_1^2/f_2^2 \approx -0.647$ (unitless)

And for double difference, all DCB terms are eliminated:

$$L_{ij,4}^{kl} = -\xi I_{ij}^{kl} + B_{ij,4}^{kl} \tag{2.31}$$

$$P_{ij,4}^{kl} = +\xi_4 I_{ij}^{kl} \tag{2.32}$$

The ambiguity term, $B_{ij}^{kl} = \lambda_{L1} N_{ij,L1}^{kl} - \lambda_{L2} N_{ij,L2}^{kl}$, can't be expressed in terms of λN; therefore, the bias term is expressed in a real number in unit of cycles.

Widelane Linear Combination (WL) is expressed in unit of metres by the following:

$$L_5 = \kappa_{1,5} L_1 + \kappa_{2,5} L_2 \tag{2.33}$$

$$P_5 = \kappa_{1,5} P_1 + \kappa_{2,5} P_2 \tag{2.34}$$

where the dimensionless constants,

$$\kappa_{1,5} = +\frac{f_1}{f_1 - f_2} \approx +4.529 \tag{2.35}$$

$$\kappa_{2,5} = -\frac{f_2}{f_1 - f_2} \approx -3.529 \tag{2.36}$$

$$\tag{2.37}$$

In terms of double difference, we have

$$L_{ij,5}^{kl} = \rho_{ij}^{'kl} - \xi_5 I_{ij}^{kl} + \lambda_{WL} N_{ij,WL}^{kl} \tag{2.38}$$

$$P_{ij,5}^{kl} = \rho_{ij}^{'kl} + \xi_5 I_{ij}^{kl} \tag{2.39}$$

where, $N_{ij,5}^{kl}$ is an integer ambiguity (cycle),

$\xi_5 = -f_1/f_2 \approx -1.283$ is the scale factor converting the ionospheric delay from L2 to L1, and

$\lambda_{WL} = c/(f_1 - f_2) \approx 0.862$ m.

WL ambiguity has one useful arithematical relationship with respect to its L1 and L2 counterparts:

$$N_{ij,WL}^{kl} = N_{ij,L1}^{kl} - N_{ij,L2}^{kl} \tag{2.40}$$

L3 linear combination is typically combined with WL linear combination in resolving the N_{L1} or N_{L2} integer ambiguities. Because of the 86 cm wavelength, it has a higher success rate in resolving the ambiguities. Once they are found, the NL, $\lambda_{NL} \approx 10.7$ cm, is introduced to bootstrap and resolve the L1 ambiguities using the following relationship in unit of metres: Substitute into Equation 2.21 yields,

$$L_{ij,3}^{kl} = \rho_{ij}^{'kl} + \frac{f_{L2}^2 \lambda_{L2}}{f_{L1}^2 - f_{L2}^2} N_{ij,WL}^{kl} + \underbrace{\frac{f_{L1}^2 \lambda_{L1} - f_{L2}^2 \lambda_{L2}}{f_{L1}^2 - f_{L2}^2}}_{\lambda_{NL}} N_{ij,1}^{kl} \tag{2.41}$$

Once N_{L1} ambiguities are resolved, one may apply Equation 2.20 to remove the ionosphere effect. For shorter baselines, less than 20 km or so, where the ionosphere effect can be effectively removed by differencing, one could attain better precision using the pure L1 carrier phase because of lower measurement noise.

Characteristics of Linear Combined Observations are summarized in Table 2.1. It provides noise characteristics relative to the L1 carrier. The noise levels of the fundamental carriers, L1 and L2 are assumed identical. The measurement noise

is derived from the error propagation law assuming absence of cross-correlation, i.e. $\sigma_{LC}^2 = (\kappa_1 \sigma_{L1})^2 + (\kappa_2 \sigma_{L2})^2$.

Table 2.1: Summary of LC and Their Characteristics

LC	Description	λ (m)	κ_1	κ_2	Ionosphere Error Relative to L1	Noise Ratio Relative to L1
L1	L1 Carrier	0.190	1.000	0.000	1.000	1.000
L2	L2 Carrier	0.244	0.000	1.000	1.647	1.000
L3	Ionosphere-Free LC	$-^{\dagger}$	2.546	-1.546	0.000	2.978
L4	Geometry-Free LC	$-^{\ddagger}$	1.000	-1.000	-0.647	1.414
WL	Widelane LC	0.862	4.529	-3.529	-1.283	5.742

† L3 wavelength can't be expressed numerically in terms of λN, but it is often associated with narrowlane, i.e. $\lambda_{NL} \approx$10.7 cm (refer to Equation 2.41),

‡ L4 ambiguity term can't be expressed in form of λN (refer to Equation 2.31).

Chapter 3

Atmospheric Effects And Modelling

GPS signals are dispersed and refracted as they travel through layers of earth's atmosphere. The uppermost *ionosphere* layer is an electronically charged medium that causes radio signals to disperse, implying that the degree of refraction depends on the frequency. The signal then travels through the electronically neutral lower *stratosphere* and *troposphere* layers. *Ultra-High Frequency* (UHF) signals, including the GPS signals, are not dispersed in these layers, but both L1 and L2 signals are equivalently refracted due to the increasing dense atmosphere as they reach the surface. The dispersion of a radio wave in the ionosphere is primarily a function of free-electrons present along its ray path, and the refraction in the troposphere is related to the neutral molecular density.

The boundaries of atmospheric layers (see Figure 3.1) are not clearly defined. The troposphere extends from the ground level to between 9 km in the Polar Regions to 16 km in the Equatorial Regions. This variable region is the *tropopause*. The *stratosphere* extends from the upper boundary of the tropopause to about 50 km. In the absence of ionized particles, all these neutral layers are commonly lumped together and simply referred as troposphere in GPS literatures. The lower boundary of the ionosphere starts at about 50 km and extends to above 1000 km.

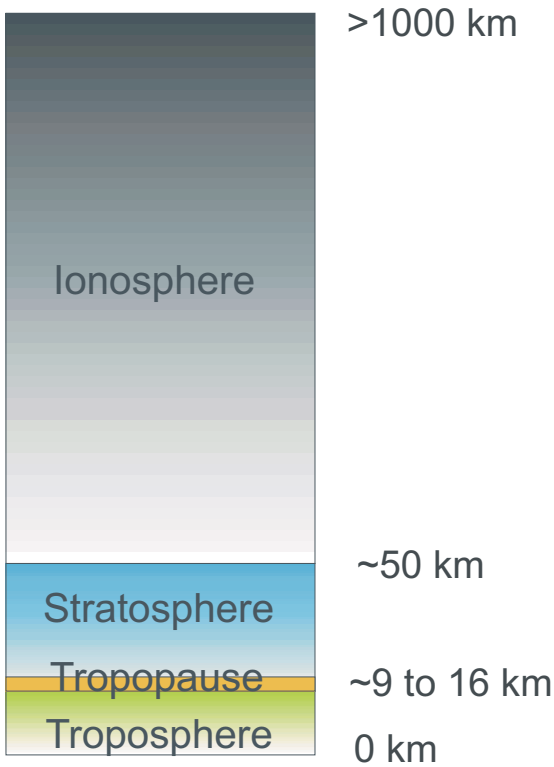

Figure 3.1: Atmosphere Layers

3.1 Ionosphere

3.1.1 Ionization Processes

The ionospheric structure is highly dynamic and can vary one to two orders of magnitude in its electron content. The solar radiation plays a key role in the formation of free electrons. The *Extreme Ultra-Violet* (EUV) and the X-ray spectrums are responsible for the ionization process that causes the electrons to break away from the gaseous O, O_2 and N_2 molecules. The charged particles are then subjected to geomagnetic field, which gyrate around the field lines, drift azimuthally, and react

with other ions and gaseous species. The electron content present in the ionosphere is a dynamic equilibrium of the photochemical ionization and recombination. The molecular absorption of the solar ultraviolet radiation increases with increasing altitude, while the atmospheric density decreases owing to decreasing gravity. And different species absorb EUV and X-ray at varying rates. All these contributing factors result in a stratification of density layers, termed D, E, F1, and F2. The F1 and F2 layers are produced by the EUV radiation, with the F1 layer vanishing at night in the absence of solar radiation. The underlying D and E layers are produced by the X-ray radiation, with the D layer vanishing at night. The maximum electron density is usually found in the F2 layer, and it is the predominant source of ionospheric errors.

The Earth's Magnetic Field

The Solar-Geomagnetic reference frame is often the choice of referencing system when working with the TEC, because the ionized particles interact with the solar radiation and geomagnetic field, and the global TEC distribution is much more stable in the solar reference frame than the earth-fixed one. The geomagnetic dips are the intersections between the Earth's surface and the geomagnetic dipole axis. The intersection between the plane through the earth centre perpendicular to the dipole axis and the Earth's surface is the geomagnetic equator. According to the International Geomagnetic Reference Frame (IGRF95), current geomagnetic poles are located at N79.4° and W71.6° and drift about +0.03° and -0.07° annually (Schaer, 1999). Alternatively, the poles can be calculated as a function of the *Modified Julian*

Day (MJD) using the following expression (Skone, 1998):

$$\phi_{dip} = 78.8 + 4.283E - 2\frac{MJD - 46066}{365.25} \tag{3.1}$$

$$\lambda_{dip} = 289.1 - 1.413E - 2\frac{MJD - 46066}{365.25} \tag{3.2}$$

And the conversion from the geographic to the geomagnetic coordinates, $(\phi, \lambda) \Rightarrow (\Phi, \Lambda)$ is carried out by:

$$\sin\Phi = \sin\phi \sin\phi_{dip} + \cos\phi \sin\phi_{dip} \cos(\lambda - \lambda_{dip}) \tag{3.3}$$

$$\sin\Lambda = \frac{\cos\phi \sin(\lambda - \lambda_{dip})}{\cos\phi} \tag{3.4}$$

Solar Cycle

Sunspots are the cooler, dark spots that appear on sun surface. Their frequency is a good indicator for the solar activities that influences Earth's ionospheric characteristics. They have been observed since the early 1600's with daily counts starting in 1749. The number shows a distinct 11 year cycle. According to Figure 1.1, we are currently receding from Cycle Number 23, that had peaked in the middle of year 2000.

The structure of the ionosphere varies in response to solar electromagnetic and corpuscular radiation. Heightened solar activity is typically associated with an increase of solar flares and coronal mass ejection. A solar flare is a sudden release of electromagnetic energy and may include corpuscular radiation. A sudden increase of X-ray emissions causes a large increase in daylight ionization in the lower ionosphere layers. The coronal mass eruption typically occurs once a week during the solar minimum and increase to an average of 2 to 3 times daily near the solar maximum. If the predominant electron and proton corpuscular ejection is directed toward earth,

we may experience a *Geomagnetic Storm* that disrupts the Earth's magnetic field. The arriving charged particles interact with Earth's magnetic field and can cause significant changes to the morphology of the ionosphere. A variation of such effect known as the *Substorm* occurs primarily in the polar and auroral regions, lasting for several hours (Langley, 2000).

Total Electron Content (TEC) Variability

The driving force for the dynamics of TEC is the interaction between photochemical and transport processes. The TEC is often measured in *TEC Unit* (TECU). One TECU is equivalent to $10E16\ electrons/m^2$ contained in a vertically reduced 1 m^2 column. In the absence of solar radiation, the maximum recombination of free electrons and ions occur at night giving the lowest TEC level. The transport process is the dominant source for the equatorial anomaly ($\Phi = \pm 20^{\circ}$), or the *fountain effect*, in which the drifting of free electrons interacts with the geomagnetic field to produce mass movement of ionization vertically and azimuthally. The auroral regions also experience some anomalies owing to the interaction of free electrons arriving from the magnetosphere.

Figure 3.2 shows the degree of TECU variability taken from four seasonal solstices and equinoxes at three different geographical locations. The TEC estimates are taken from spherical harmonic models whose GIM coefficients were estimated from GPS double difference carrier phase observables. The right and left columns illustrate the global variations two years prior and during the solar maximum. The

three selected sites are the IGS stations: 1) Thule, Greenland ($\Phi = N87°$), 2) Priddis, Canada ($\Phi = N58°$), and 3) Fortaleza, Brazil ($\Phi = N05°$). There had been a factor of three increases in TEC count during the two year period at the mid-latitude and the Polar Regions. In the equatorial region, the increase is at a factor of two. All exhibit diurnal variations, with an exception in the polar region, before the solar maximum, with little daily fluctuation. The minimum and maximum TEC occur at 05:00 and 14:00 local time (LT). In the equatorial region, there appear two cycles of diurnal fluctuation (i.e. two peaks). First, the TEC drops after first dominant daily maximum, rises slowly again at 22:00 LT, peaking at midnight before dropping to a daily minimum at 05:00 LT. The secondary peak is about one-third or more of the daily maximum, and does not appear in other regions. According to the plots, a single frequency user could experience up to 10 to 110 TECU, or 1.6 to 17.9 m L1 range error near the solar maximum in the equatorial region. The distinct two-hour discontinuities shown in the plots are the result of the two-hourly spherical harmonic coefficient sets.

3.1.2 Ionospheric Effects on GPS Signals

Wave propagation velocity through a medium is characterized by the index of refraction:

$$n = \frac{c}{v} \tag{3.5}$$

where, c is the speed of light in vacuum, and v is the velocity in medium.

The index of refraction through the ionosphere is expressed by a complex Appleton-

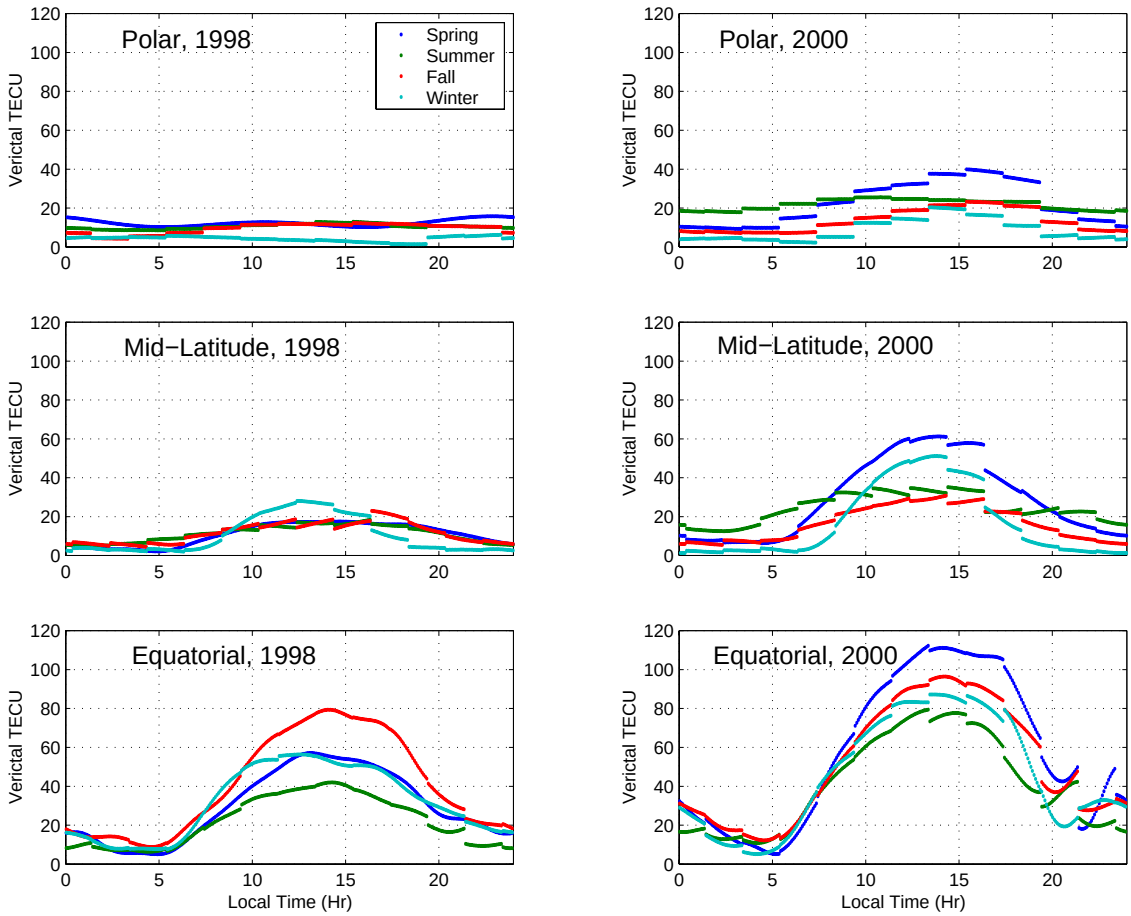

Figure 3.2: Spatial and Temporal TEC Variations

Hartree formula that accounts for many factors including the ambient magnetic field, plasma frequency, and gyro frequency. A simplified expression can be derived for GPS signals, ignoring higher terms. The higher terms only contribute 1 to 2 mm of vertical range error (Brunner and Gu, 1991). The first-order term of phase refractive index can be expressed by (Hoffmann-Wellenhof et al., 1992):

$$n_p = 1 - \frac{40.28N}{f^2} \tag{3.6}$$

And the propagation velocity for the superimposed code signal is characterized by the group delay, whose index of refraction is:

$$n_g = n_p + f\frac{dn_p}{df} \tag{3.7}$$

$$= 1 + \frac{40.28N}{f^2} \tag{3.8}$$

where, N is the electron density (count per cubic metre).

The resultant travel time through the nonhomogeneous ionospheric medium to a receiver is a total integration of infinitesimal path length, i.e.

$$dt = \int_S \frac{n_{p,g}}{c} dS \tag{3.9}$$

Inserting Equations 3.6 or 3.8 into 3.9 and multiplying by the speed of light yields the following relationships for advanced carrier phase and delayed code measurements:

$$\rho_{phase} = c \cdot dt + \delta\rho_{geom} \tag{3.10}$$

$$= \int_S (1 - \frac{40.28N}{f^2}) dS + \delta\rho_{geom} \tag{3.11}$$

$$\rho_{phase} = \rho - \frac{40.28}{f^2} \underbrace{\int_S N dS}_{TEC} + \delta\rho_{geom} \tag{3.12}$$

Similarly for code,

$$\rho_{code} = \rho + \frac{40.28}{f^2} \underbrace{\int_S N dS}_{TEC} + \delta\rho_{geom} \tag{3.13}$$

where, ρ is the true geometrical distance, $\int_S N dS$ is the TEC, and, $\delta\rho_{geom}$ is the geometrical errors including the tropospheric, orbital, clock, and multipath effects.

Note that 1 TECU induces approximately 0.163 m of ionospheric path delay on L1 and 0.267 m on L2.

3.1.3 TEC Modelling And Parameterization

The ionospheric effect on GPS signals can be characterized by the TEC using Equations 3.12 or 3.13, and most researchers utilize *one-way phase level to code*, exploiting the precision of geometry-free L4 phase measurement. Instead of solving for the ambiguity, it is adjusted by a constant to match the absolute level of code (Mannucci et al., 1993). Because of the interfrequency biases in both the receiver and the satellite hardware, DCB's are estimated in conjunction with the TEC's. Years of calibration history showed DCB's in the Turbo Rogue receivers are relatively stable (± 1 ns) so long as internal hardware components are not altered. Ignoring the satellite and receiver hardware DCB's can induce respective errors of ± 9 and ± 30 TECU (Wilson and Mannucci, 1993), and these DCB values can be estimated using an array of GPS stations, such as that of Canadian Active Control System to a precision of ± 0.5 ns (Gao et al., 1993). Typically, the DCB estimations are carried out in the evenings when the ionosphere is least active. One may neglect the DCB's by double differencing the L4 measurements. TEC estimation is an inverse problem that the station coordinates and the ambiguities are constrained.

Single Layer Mapping Function

The *single layer model* (SLM) is based on an assumption that the all-free electrons are confined to a shell of infinitesimal thickness at the centroid height (Figure 3.3), where 50% of electrons are above and 50% below this height. The ionosphere mapping function is related to the pierce point where the GPS signal path penetrates this fictitious shell. The shell height actually has both temporal and spatial variations.

Based on the *International Reference Ionosphere 1990* (IRI90) model, the predicted ionospheric shell height can vary between daytime 300 km and nighttime 400 km at station Onsala ($\phi = N57°$) during solar minimum. And the range shifts to 500 km and 600 km during the solar maximum. The shell height appears much more stable 16° south in Madrid, where the diurnal variation is nearly null during the solar minimum, and about 100 km lower during the solar maximum (Komjathy and Langley, 1996).

The slant TEC estimates taken at the pierce points are reduced to geocentric vertical, i.e. reduced to the vertical normal at the pierce point with respect to the fictitious shell. The single layer model, of course, is an approximation and can lead to several TEC of error if the horizontal gradient is significant (Mannucci et al., 1993).

The standard *Single Layer Mapping Function formulation* and its simplified counterpart, *Broadcast Mapping Function*, are as follows:

Single Layer Mapping (SLM) Function :

$$F(z) = \frac{1}{cos(z')} = \frac{1}{\sqrt{1 - sin^2(z')}} \tag{3.14}$$

$$sin(z') = \frac{R}{R+H} sin(z) \tag{3.15}$$

Broadcast Mapping Function :

$$F(E) = 1.0 + 16.0(0.53 - E)^3 \tag{3.16}$$

where, $R \approx 6378$ km earth radius, H is the shell height, z is the satellite zenith angle, z' is the satellite zenith angle at the pierce point, and E is the elevation referenced

to the horizon in unit of semi-circles (1 semi-circle = 180°).

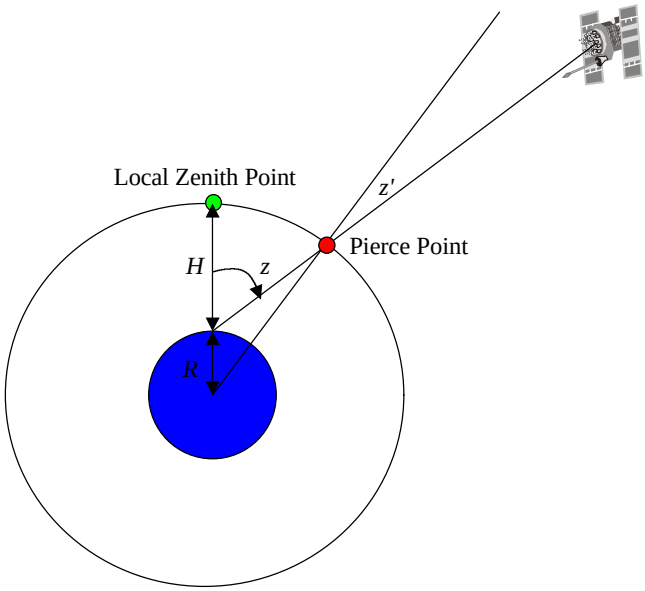

Figure 3.3: Single Layer Model (SLM)

The simpler Broadcast Mapping Function is specifically intended for real-time broadcast (Klobuchar, 1996) and agrees with the SLM Function by 1.8% at a shell height of 400 km for zenith angles at 80° (Figure 3.4). One should note that the shell height is not fixed and can be as high as 600 km as indicated in the IRI90 model. And at this height, the Broadcast Mapping Function would depart from the SLM counterpart by 18.0%. In terms of range, a 60 TECU at the mid-latitude during the current peak would induce 7.72 m of L1 range error at the zenith. Converting it to the slant delay at a zenith angle of 80° would produce a difference of 4.0 m between SLM Mapping Function and the Broadcast Mapping Function. Table 3.1

summarizes the comparison between the two mapping functions.

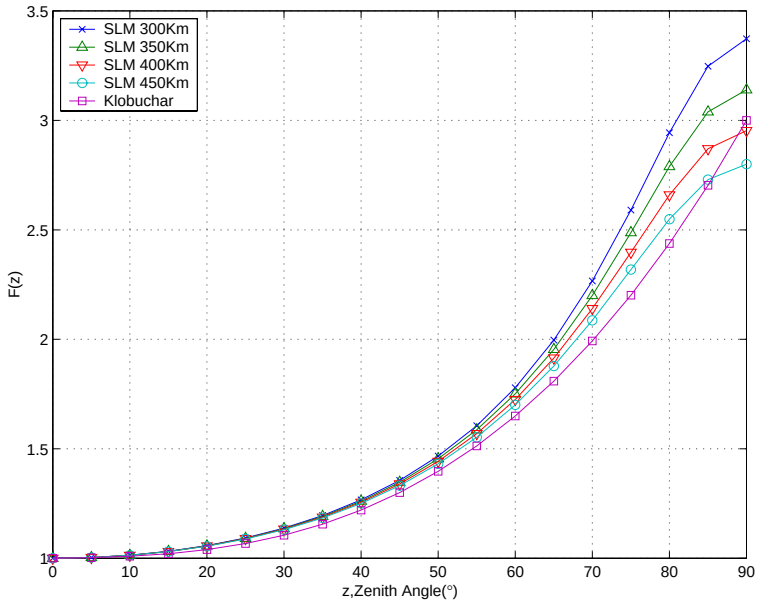

Figure 3.4: Mapping Functions At Various Shell Heights

Table 3.1: SLM Function Vs Broadcast Mapping Function at z=80°

	F	%	L1 Delay (m)	%
Broadcast Mapping Function	2.709	-	26.3	-
SLM Function @ 400 km	2.661	1.8	25.9	0.4
SLM Function @ 600 km	2.296	18.0	22.3	4.0

Ionosphere Modelling

The TEC parameters are estimated at the shell pierce points. Therefore, a double differenced observable comprising four one-way measurements has four pierce points to estimate. The expanded form of double difference L4 observation equation is

expressed by:

$$L_{i,j,4}^{k,l} = K(1 - \frac{f_1^2}{f_2^2})\left\{ \begin{array}{c} F(z_i^k)E_v(\beta_i^k, s_i^k) - F(z_i^l)E_v(\beta_i^l, s_i^l) \\ -F(z_j^k)E_v(\beta_j^k, s_j^k) + F(z_j^l)E_v(\beta_j^l, s_j^l) \end{array} \right\} + B_{i,j,4}^{k,l} \qquad (3.17)$$

where, K is a constant $\approx$ -0.163 m/TECU, $E_v(\beta_i^k, s_i^k)$ is the vertical TEC in unit of TECU at the pierce point, β is the geomagnetic latitude at the pierce point, s is the geomagnetic longitude at the pierce point referenced to local time, i.e. s = UT-12, where UT is referenced to the observer's location, and the mapping function F is based on SLM taken normally at the height of 400 km.

The quantity $E_v(\beta, s)$ is the parameter we wish to estimate at the pierce point. With sufficient observations, several parameterization techniques can be used to model the TEC at the shell surface. Some of the examples are: Taylor's expansion series; spherical harmonic expansion series; and partition of shell surface to a finite number of spherical triangular or rectangular cells, where the TEC is estimated.

Broadcast Ionosphere Model

The *Broadcast Ionsophere Model* (BIM) is a simple half-cosine function based on two sets of four coefficients, describing the worldwide ionospheric amplitude and period, can remove about 50% of the ionospheric range error in real-time. These coefficients included in the navigation message are updated about once a day. The model assumes the diurnal peaks at 14:00 LT with constant night time delay of E_{min} = 5 ns at L1 ($\approx$ 9.2 TECU).

The amplitude of the half-cosine function is computed from the following:

$$E_{amp}(\beta) = \begin{cases} \frac{c}{\xi}\sum_{i=0}^{3} a_i\beta^i & \text{if} \geq 0 \\ 0 & \text{if} < 0 \end{cases} \tag{3.18}$$

And for the period, τ,

$$\tau(\beta) = \begin{cases} \sum_{i=0}^{3} b_i\beta^i & \text{if} > \tau_{min} \\ \tau_{min} & \text{if} < \tau_{min} \end{cases} \tag{3.19}$$

Finally, the TECU at the pierced point (β,s),

$$E_v(\beta, s) = \begin{cases} E_{min} + E_{amp}(\beta)cos(s') & \text{if } |s'| < \frac{\pi}{2} \\ E_{min} & \text{if } |s'| \geq \frac{\pi}{2} \end{cases} \tag{3.20}$$

where, $\tau_{min} = 20$ Hr, the local time of the ionospheric point $s = \Lambda_{IP}/15 + T_{UT}$, and the phase angle $s' = 2\pi(s-2)$.

IGS Global Ionosphere Models

Five IGS analysis centers produce *Global Ionosphere Map* (GIM) estimations conforming to the IONosphere map EXchange (IONEX) format, a standard developed by the IGS community (Schaer, 1998), and estimations are available from the NASA's Crustal Dynamics Data Information System(CDDIS) ftp site[1]. The contributing agencies include:

- the Center for Orbit Determination in Europe, CODE (Switzerland)

[1]ftp://cddisa.gsfc.nasa.gov/pub/gps/products/IONEX

- the Natural Resources Canada, NRCan (Canada)
- the European Space Agency , ESA (Germany)
- the Jet Propulsion Laboratory, JPL (USA)
- the Polytechnical University of Catalonia, UPC (Spain)

The IONEX files express the TEC in grid form in increments of 2 hours with a typical spacing of 2.5° latitude by 5° longitude. The estimates from the contributing agencies can vary drastically both in amplitude and gradient. Discrepancies of several TECU or more are common. The factors may include different techniques employed, different station distribution, different mask angle, and fixing to false shell height. The number of global stations used to derive the estimation varied from 49 by the ESA to 97 stations by the JPL.

The CODE facility at the Astronomical Institute of University of Berne also post the GIM in a much more compact format using a set of 12 degree by 8 order spherical harmonic coefficients[2] (Schaer, 1997):

$$E_v(\beta, s) = \sum_{n=0}^{n_{max}} \sum_{m=0}^{n} \Gamma_{nm} P_{nm} sin\beta \left\{ \widetilde{C}_{nm} cos(ms) + \widetilde{S}_{nm} sin(ms) \right\} \tag{3.21}$$

$$\Gamma_{nm} = \sqrt{\frac{(n-m)!(2n+1)(2-\delta_{(}0m)}{(n+m)!}} \tag{3.22}$$

Where, $s = \Lambda - \Lambda_o$ is the sun-fixed geomagnetic longitude at the ionospheric pierced point, n_{max} is the maximum degree of the harmonic expansion, Γ_{nm} are normalization factors, P_{nm} are the classical unnormalized Legendre functions, a_{nm}, b_{nm} are

[2]ftp://ftp.unibe.ch/aiub/BSWUSER/ATM/

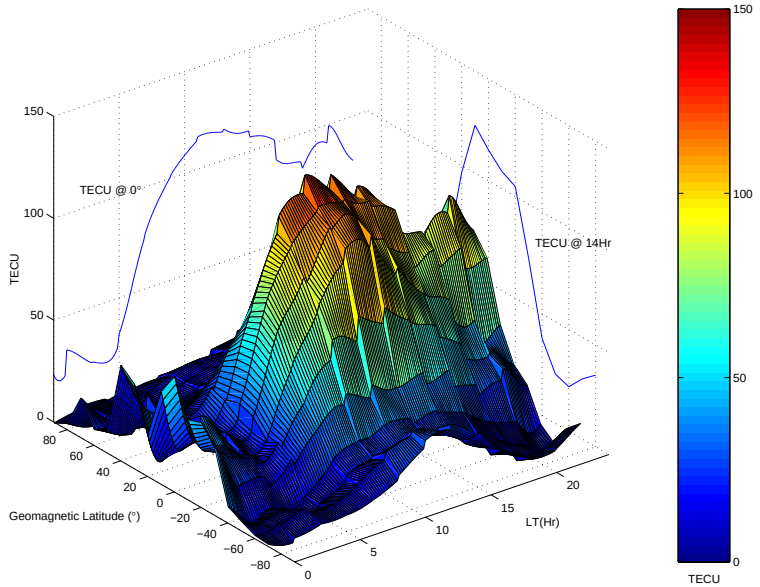

Figure 3.5: CODE Global Ionosphere Map (GIM), April 7, 2000

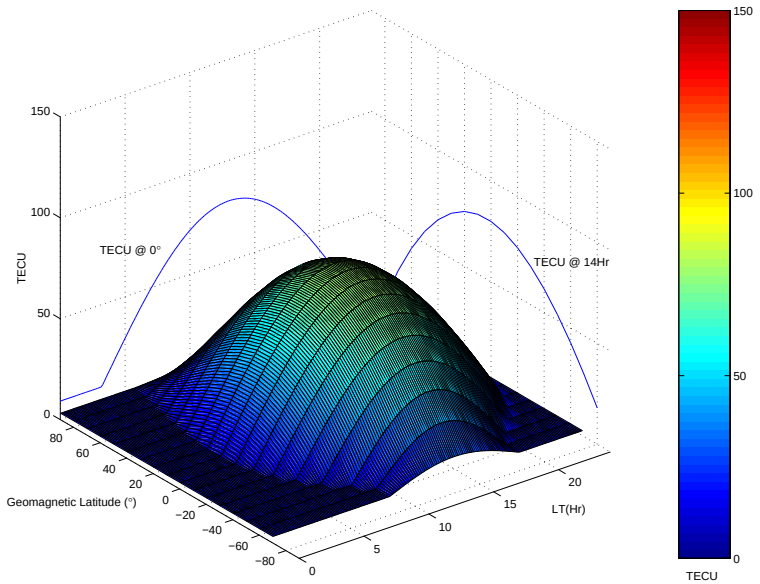

Figure 3.6: Broadcast Ionosphere Model (BIM), April 7, 2000

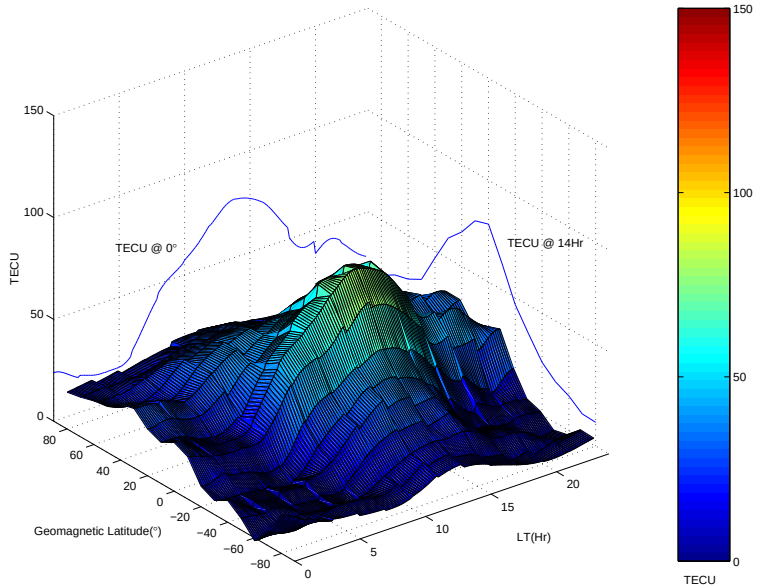

Figure 3.7: CODE Global Ionosphere Map (GIM), June 21, 2000

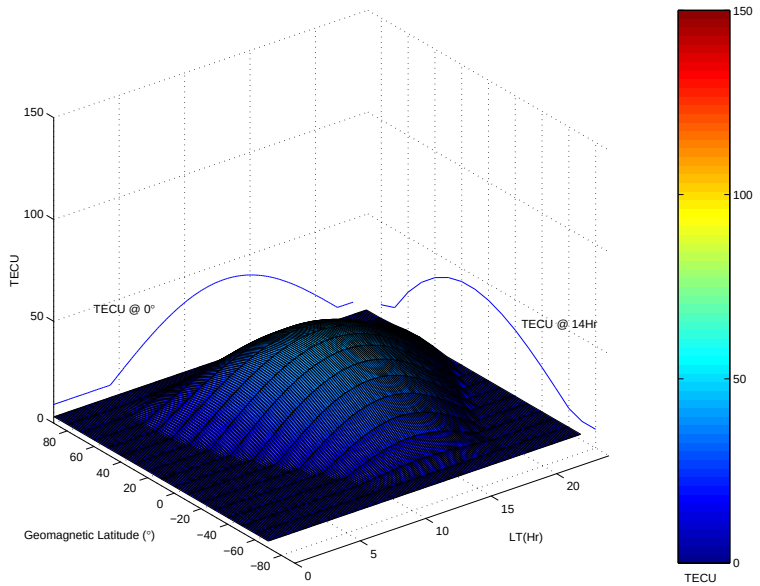

Figure 3.8: Broadcast Ionosphere Model (BIM), June 21, 2000

the coefficients of the spherical harmonic expansion, and δ is the Kronecker delta function.

For a comparison, Figures 3.5, 3.6, 3.7, and 3.8 show the global ionospheric delay based on the GIM and the BIM for both April 7 and June 21, 2000.

3.1.4 Application of Ionosphere Models

The global TEC differences between the BIM and the GIM vary as much as 60 TECU on April 7, an active day, and 40 TECU during on June 21, a quiet day. The impacts on double difference carrier phase with application of the ionosphere models are illustrated by Figure 3.9 over a 145 km baseline between ONSA and VANE and Figure 3.10 over a 35 km basline between ONSA and GOTE. The tropospheric delay corrections using the Modified Hopfield model with the standard meteorological parameters were applied.

The GIM are based on two-hour averaged estimation in post-mission mode. The corrected double difference measurements are consistently better than both uncorrected and the BIM corrected counterparts. Over the 145 km baseline, the application of GIM on L1 carrier phase reduced the RMS error by 8% on the active day and by 37%. The RMS reduction is also apparent at a shorter 35 km baseline at 2% on the active day and 34% on the quiet day.

The BIM are intended for single-frequency pseudorange users to reduce about

50% of the ionospheric delays and are based on prediction. They are not designed for high precision carrier phase corrections. Regardless, their impact on L1 carrier phase is investigated, and the results are somewhat mixed. The error RMS is increased by 5% during the active day, but reduced by 20% during the quiet day over the 145 km. Similarly, the RMS is increased by 2% on the active day and reduced by 15% on the quiet day over the 35 km baseline.

Both BIM and GIM are deterministically derived, implying that both would not cope well with rapid temporal and spatial variations and irregularities. The BIM correction coefficients, consist of eight parameters, are updated on a daily basis at best (Klobuchar, 1996). The GIM coefficients are computed daily and are available with a delay of about four days (Schaer, 1997).

3.2 Troposphere

The tropospheric delay can be separated into two components. The hydrostatic delay is responsible for most of the effect, accounting for about 90% of total path delay at 2.3 to 2.4 m at the zenith. The hydrostatic delay, though it has a small water vapour contribution, is referred as the *dry* delay. The dry delay can be estimated to better than 1 mm with surface pressure to an accuracy of 0.3 mBar (Duan et al., 1996). The *wet* delay is highly variable both spatially and temporally making it more difficult to estimate and predict. It can't be eliminated effectively by differencing unless the network is small (<20 km) with little inter-station height difference. Its

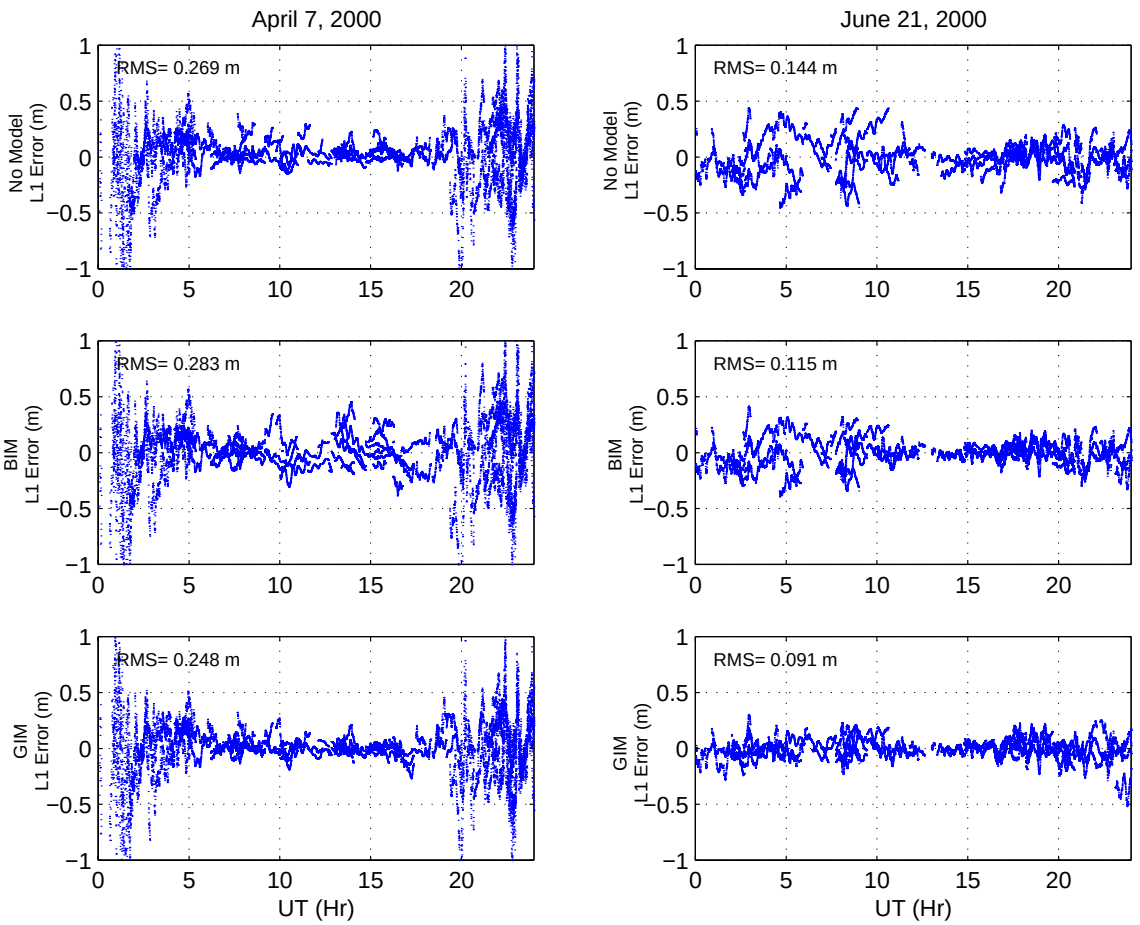

Figure 3.9: The Impact of Ionosphere Models on Double Difference L1 Measurements Over 145 km Baseline, ONSA-VANE

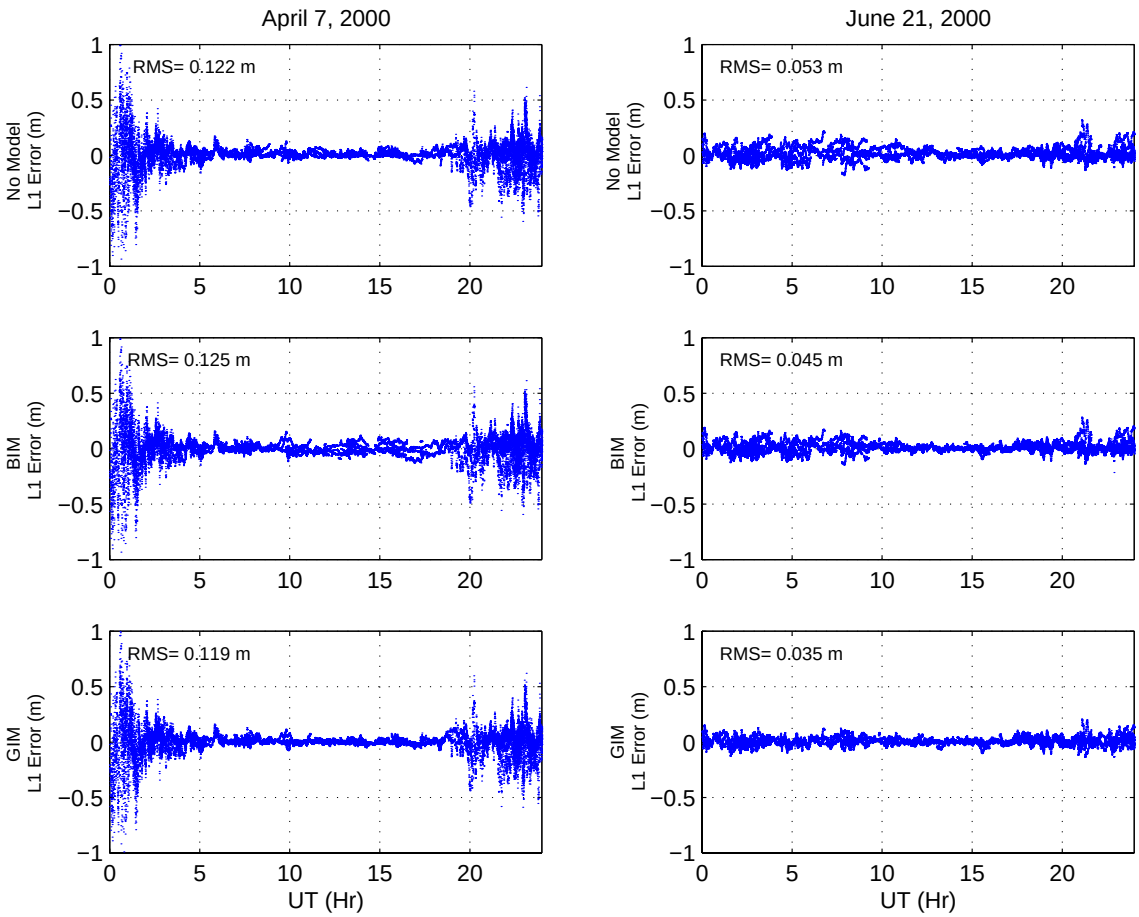

Figure 3.10: The Impact of Ionosphere Models on Double Difference L1 Measurements Over 35 km Baseline, ONSA-GOTE

magnitude varies from a few millimetres in the polar region to 40 cm at zenith in tropical regions (Brunner and Welsch, 1993). The *Total Zenith Delay* (TZD) is the sum of both wet and dry delays at the local zenith. The troposphere delays for both carrier and code on L1 or L2 are all identical. The index of refraction varies with atmospheric density, and integration along the path has to be performed:

$$\delta_{trop} = \int_S (N_{dry} + N_{wet}) dS \tag{3.23}$$

The slant troposphere delay is related to the TZD by a mapping function. The available mapping functions can be grouped into three major classes: Hopfield's quadric profile, Marini's continuous function, and Saastamoinen's cosecant law. The cosecant rule effectively removes the first order effect assuming a flat Earth with a constant refractivity and is used in the total troposphere delay models that follow.

3.2.1 Troposphere Modelling

The simplest approach, though inadequate, to estimate the TZD is through one of many empirical models. The common ones are the Saastamoinen Model (Equation 3.27) and Modified Hopfield Model (Equation 3.29) with meteorological inputs such as the barometric pressure, temperature, and relative humidity. The meteorological input can either be a standard model based on a nominal set (Equations 3.24, 3.25, 3.26), or from actual surface measurements. Another approach of much greater accuracy is a combination of *Water Vapour Radiometer* (WVR) and barometric measurements. The WVR measures the radiating water vapour resonance energy with a potential resolution of 1mm in the wet component. Adding the dry component estimated from a barometric measurement then forms the TZD. The

disadvantages with WVR are that calibration is cumbersome to a sufficient level of accuracy, and it does not operate in rain or reliably at low elevations.

Standard Model (Berg, 1948):

$$P = P_r[1 - 0.0000226(Ht - Ht_r)]^{5.225} \quad (3.24)$$

$$T = T_r - 0.0065(Ht - Ht_r) \quad (3.25)$$

$$H = Hr[e^{-0.0006396(Ht - Ht_r)}] \quad (3.26)$$

The typical meteorological references are: $Ht_r = 0$ m, $P_r = 1013.25$ mBar, $T_r = 291.15°$ K (18° C), and $H_r = 50\%$ (Rothacher and Mervert, 1996). The input height, Ht, is in metres.

Saastamoinen Model (Saastamoinen, 1973):

$$\delta_{trop} = 0.002277 \csc z \left\{ P + (\frac{1255}{T} + 0.05)e - tan^2 z \right\} \quad (3.27)$$

where, the partial water vapour pressure e in mBar,

$$e = H \cdot exp(-37.2465 + 0.213166T - 0.000256908T^2) \quad (3.28)$$

where, z is the satellite zenith angle in degrees, H, T, and P are the input standard meteorological parameters from Equations 3.24 to 3.26, in units of mBar, Kelvin, and relative humidity (%).

Modified Hopfield (Goad and Goodman, 1974):

$$\delta_{trop} = 0.002277 \csc z \Big(1 + 0.0026 cos(2z) + 0.00028H\Big) \Big\{ P + (\frac{1255}{T} + 0.05)e \Big\} \quad (3.29)$$

3.2.2 Inverse GPS Method

Instead of solving for the positional parameters, the absolute total zenith delay can be extracted from the ionosphere free L3 observables by holding the positions fixed. The tropospheric delay parameter can be estimated sequentially using an optimal filter such as a Kalman filter. The GPS approach provides a 24-hour "all-weather" troposphere monitoring system without requiring special hardware and achieves a sub-centimetre level of accuracy. This is comparable with the WVR approach without the need for the cumbersome system calibration (Tralli and Lichten, 1990; Bevis et al., 1992; Businger et al., 1996; Darin et al., 1998).

Figure 3.11 provides a comparative performance of various TZD estimation methods for Sept 16, 1998 at Station Onsala. The plots shown were all computed specifically for comparison purposes. Both Saastamoinen and Modified Hopfield Models agreed to better than 2 mm. Note that the WVR sensors do not operate well under precipitation conditions. The conditions were apparent by the scatter signature as shown in the plot. Either the Saastamoinen or the Modified Hopfield empirical models with the surface meteorological data agreed with the WVR reading by 33 mm. Both empirical models with standard meteorological parameters agreed by 42 mm. And the GPS method agreed with the WVR method within 10 mm.

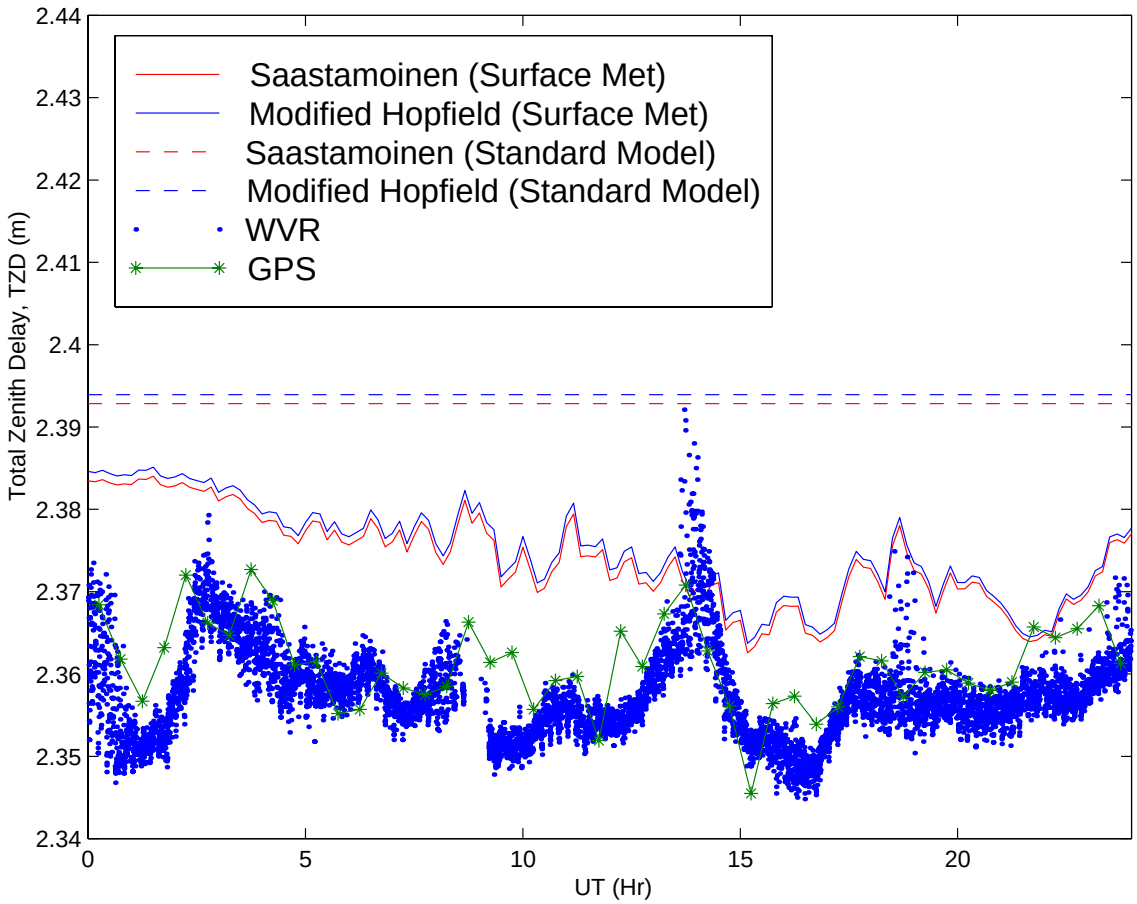

Figure 3.11: Empirical, WVR, GPS TZD Estimations, Sept 16, 1998 at Station Onsala

Chapter 4

Implementation

4.1 Overview of the Kalman Filter

The Kalman Filter is a recursive mode of state-time operation such that the present state is estimated with the aid of the previous state. It combines all available measurements with prior knowledge of the system and the measuring device characteristics to produce a set of estimates whose error is statistically minimized. It is different from the typical sequential least-squares adjustment in that the estimates can be time-variant, making it suitable for dynamic applications, and the estimates will not necessarily improve with increasing number of measurements over time. Also, the operation is a combination of prediction and filtering, and not strictly an adjustment; thus, the number of measurements can be less than the number of estimates and have a non-uniform data coverage at any point in time (Schwarz, 1987).

The recursive processing mode of operation can continue indefinitely and has a definite advantage over the non-recursive mode from computational and memory perspectives. However, as with any linear system modelling, both measurements and the system are subject to inherent stochastic noise resulting in directional bias (Blais, 1988). The divergence of a Kalman Filter may occur due to the noise, round-off errors, and modelling errors. The notation used here is adapted from (Brown and Hwang, 1997) for its conciseness.

System Model

$$\hat{x}_{k+1}^{-} = \Phi_k \hat{x}_k + w_k \tag{4.1}$$

$$P_{k+1}^{-} = \Phi_k P_k \Phi_k^T + Q_k \tag{4.2}$$

where, $\hat{x}_k$ is the state vector at epoch k, Φ_k the state transition matrix, and w_k the assumed system white process noise sequence. The initial state, $\hat{x}_k$, is projected ahead by Equation 4.1 yielding, $\hat{x}_{k+1}^{-}$. The corresponding (co)variance matrices are symbolized by P_k and P_{k+1}^{-}, respectively. The state transition matrix, Φ_k, takes the form of an identity matrix in the implementation.

With the following assumptions, the Filter Equations 4.7-4.9 are derived:

$$E\{w_k \cdot w_l^T\} = \begin{cases} Q_k & \text{if } k = l \\ 0 & \text{if } k \neq l \end{cases} \tag{4.3}$$

$$E\{v_k \cdot v_l^T\} = \begin{cases} R_k & \text{if } k = l \\ 0 & \text{if } k \neq l \end{cases} \tag{4.4}$$

$$E\{w_k \cdot v_l^T\} = 0 \quad \text{for all } k \text{ and } l \tag{4.5}$$

where $E\{.\}$ is the expectation operator.

Measurement Model

$$z_k = H_k \hat{x}_k^{-} + v_k \tag{4.6}$$

Filter Equations

$$\hat{x}_k = \hat{x}_k^- + K_k(z_k - \underbrace{H_k\hat{x}_k^-}_{z_o}) \tag{4.7}$$

$$P_k = (I - K_k H_k)P_{k-1} \tag{4.8}$$

$$K_k = P_k^- H_k^T (H_k P_k^- H_k^T + R_k)^{-1} \tag{4.9}$$

where z_k is the measurement vector, H_k is the design matrix relating measurement to the state vectors at epoch k, v_k is the assumed white measurement noise sequence, z_o is the approximate measurements transformed from the last state vector at epoch, $k-1$, and K_k is the gain matrix. The standard Kalman Filter is best summarized by Figure 4.1.

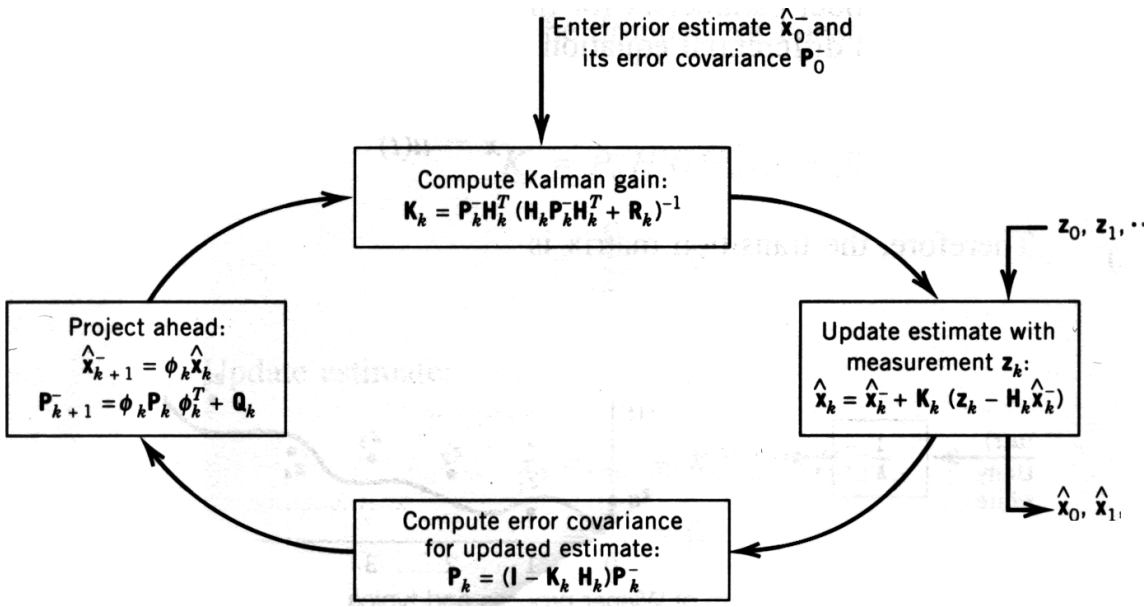

Figure 4.1: Standard Kalman Filter Algorithms (Brown and Hwang 1997)

4.2 Non-Linear Measurement Model

GPS measurement models are non-linear with respect to the estimates. The standard Kalman Filter equations are intended for linear models, and applying them on non-linear models may induce a significant bias depending on both the closeness of the point of expansion, z_o, to the truth and the degree of non-linearity. In Brown and Hwang (ibid) two variations of linearization are mentioned, neither requires iteration. The *Extended Kalman Filter* uses a constant initial value as a point of expansion. The *Linearized Kalman Filter* requires an external input, serving as a point of expansion. Neither is suited for stand-alone kinematic GPS applications. A better approach, suggested by Salzmann (1993), employs the Gauss-Newton iteration within single epoch, k, to minimize the bias, i.e.

$$\hat{x}_{k,i+1} = \hat{x}_{k,i} + \frac{\partial_{k,x} H(\hat{x}_{k,i})^T R^{-1}}{\partial_x H(\hat{x}_{k,i})^T R^{-1} \partial_x H(\hat{x}_{k,i})} [z - H(\hat{x}_{k,i})] \tag{4.10}$$

with tolerance criteria,

$$\|\hat{x}_{k,i+1} - \hat{x}_{k,i}\|_P = \sqrt{(\hat{x}_{k,i+1} - \hat{x}_{k,i})^T P^{-1} (\hat{x}_{k,i+1} - \hat{x}_{k,i})} < \varepsilon \tag{4.11}$$

where, i is the iteration step at epoch k, $\partial_x H(\hat{x}_{k,i})$ is the Jacobian of $H(\hat{x}_{k,i})$ evaluated at $\hat{x}_{k,i}$, and ε is the tolerance.

Applied to the Kalman Filter, Equations 4.7, 4.9, and 4.8 become,

$$\hat{x}_{k,i+1} = \hat{x}_{k-1} + K_{k,i+1}[z_k - H_k(\hat{x}_{k,i}) - \partial_x H_k(\hat{x}_{k,i})(\hat{x}_{k-1} - \hat{x}_{k,i})] \tag{4.12}$$

$$P_{k,i+1} = [I - K_{k,i+1} \partial_x H_k(\hat{x}_{k,i})] P_{k-1} \tag{4.13}$$

$$K_{k,i+1} = P_{k-1} \partial_x H_k(\hat{x}_{k,i})^T [\partial_x H_k(\hat{x}_{k,i}) P_{k-1} \partial_x H_k(\hat{x}_{k,i})^T]^{-1} \tag{4.14}$$

For instance, static double differenced Ashtech Z-XII dual frequency carrier and code measurements over about 100 km yield a centimetre-level of bias without applying the Gauss-Newton iteration process. If applied, two iterations are typically needed, reducing the bias to sub-millimetre level, i.e. $\varepsilon < 1$ mm in Equation 4.11.

4.3 Random Processes

The time correlated ionosphere disturbances are parameterized in the state vector, whose scalar description of linear dynamic behaviour can be characterized by a number of correlation models (Strang and Borre, 1997).

Random Constant

$$I_k = constant + w_k \tag{4.15}$$

$$\begin{aligned} E\{w_k^2\} &= E\{(I_k - constant)^2\} \\ &= \sigma^2 \end{aligned} \tag{4.16}$$

Random Walk

$$I_k = I_{k-1} + w_k \tag{4.17}$$

$$\begin{aligned} E\{w_k^2\} &= E\{(I_k - I_{k-1})^2\} \\ &= E\{I_k^2\} + E\{I_{k-1}^2\} - 2E\{I_k I_{k-1}\} \\ &= 2\sigma^2 \end{aligned} \tag{4.18}$$

Gauss-Markov

$$
\begin{aligned}
I_k &= e^{-\frac{t_k - t_{k-1}}{T}} I_{k-1} + w_k && (4.19)\\
E\{w_k^2\} &= E\{(I_k - e^{-\frac{t_k - t_{k-1}}{T}} I_{k-1})^2\} \\
&= E\{I_k^2 - 2e^{-\frac{t_k - t_{k-1}}{T}} I_k I_{k-1} + e^{-2\frac{t_k - t_{k-1}}{T}} I_{k-1}^2\} \\
&= E\{I_k^2 - 2e^{-\frac{t_k - t_{k-1}}{T}} e^{-\frac{t_k - t_{k-1}}{T}} I_{k-1}^2 + e^{-2\frac{t_k - t_{k-1}}{T}} I_{k-1}^2\} \\
&= \sigma^2 - \sigma^2 e^{-2\frac{t_k - t_{k-1}}{T}} \\
&= \sigma^2\Big(1 - e^{-2\frac{t_k - t_{k-1}}{T}}\Big) && (4.20)
\end{aligned}
$$

where, σ^2 is the distance dependent variance, T is the so-called *correlation time*, or the $1/e$ point (Gelb, 1996).

A variation of Gauss-Markov process occasionally describes the geophysical phenomena by combining both time and distance correlations (Gelb, ibid):

$$\sigma^2(\tau, d) = \sigma_\circ^2 \; e^{\frac{-|\tau|}{T}} \; e^{\frac{-d}{D}} \qquad (4.21)$$

where, $\sigma_\circ$ is the constant variance, T and D are the first-order time and distance correlations, and $\tau = t_k - t_{k-1}$.

In reality, the first variation of Gauss-Markov process, Equation 4.20, is preferred over the second variation, Equation 4.21, for modelling the double difference random process. The time correlation, T, can be estimated directly from the time-domain autocorrelation function. In contrast, the distance correlation, D, is much harder to estimate, because the distance-domain autocorrelation function requires many baselines preferably of evenly spaced lengths, reaching up to a couple of thousands

Km long. Some researchers have estimated the correlation distance of about 1500 Km (Goad and Yang, 1994).

4.4 Functional Model

The functional model used in the development of the algorithm is taken from Goad and Yang (1994). The traditionally ignored ionosphere term is parameterized in the state vector to account for the residual double difference ionosphere over longer baselines. Each double difference ionosphere term is parameterized independently for each satellite pair. The fictitious *pseudo-observable* (Equation 4.26), is introduced to constrain the double difference ionosphere residual to zero with an appropriate noise level. A tight constraint reduces to the simple case of independent L1 and L2 observations found in the short-baseline model. At the opposite extreme, a loose constraint reduces to the ionosphere-free, L3 observation found in the long-baseline model. A lightly constrained zero ionosphere is an ideal trade-off for a middle-distance model, typically in the several tens of kilometres range. A constraint of 1 to 8 parts per million was suggested by Bock et al (1986).

The L1 and L2 observations Equations, 4.22 and 4.23, shown in the following measurement model are explicitly expressed, not linearly combined. This enables a direct N_{WL} ambiguity resolution, not possible if a linearly combined ionosphere-free observation, L3, were used. The non-integer ambiguity nature of L3 can't extract the widelane integer ambiguity.

$$
\begin{aligned}
L1_{i,j}^{k,l} &= \rho_{i,j}^{k,l} + \lambda_{L1} N_{L1,i,j}^{k,l} - I_{i,j}^{k,l} && (4.22)\\
L2_{i,j}^{k,l} &= \rho_{i,j}^{k,l} + \lambda_{L2} N_{L2,i,j}^{k,l} - \beta I_{i,j}^{k,l} \\
&= \rho_{i,j}^{k,l} + \lambda_{L2} N_{L1,i,j}^{k,l} - \lambda_{L2} N_{L1,i,j}^{k,l} + \lambda_{L2} N_{L2,i,j}^{k,l} - \beta I_{i,j}^{k,l} \\
&= \rho_{i,j}^{k,l} + \lambda_{L2} N_{L1,i,j}^{k,l} - \lambda_{L2} \underbrace{(N_{L1,i,j}^{k,l} - N_{L2,i,j}^{k,l})}_{widelane, N_{WL,i,j}^{k,l}} - \beta I_{i,j}^{k,l} \\
&= \rho_{i,j}^{k,l} + \lambda_{L2} N_{L1,i,j}^{k,l} - \lambda_{L2} N_{WL,i,j}^{k,l} - \beta I_{i,j}^{k,l} && (4.23)\\
P1_{i,j}^{k,l} &= \rho_{i,j}^{k,l} + I_{i,j}^{k,l} && (4.24)\\
P2_{i,j}^{k,l} &= \rho_{i,j}^{k,l} + \beta I_{i,j}^{k,l} && (4.25)\\
I_{i,j}^{k,l} &= 0 && (4.26)
\end{aligned}
$$

where,

$$
\begin{aligned}
\beta &= (f_1/f_2)^2 && (4.27)\\
\rho_{i,j}^{k,l} &= \sqrt{(X^k - X_i)^2 + (Y^k - Y_i)^2 + (Z^k - Z_i)^2} \\
&- \sqrt{(X^l - X_i)^2 + (Y^l - Y_i)^2 + (Z^l - Z_i)^2} \\
&- \sqrt{(X^k - X_j)^2 + (Y^k - Y_j)^2 + (Z^k - Z_j)^2} \\
&+ \sqrt{(X^l - X_j)^2 + (Y^l - Y_j)^2 + (Z^l - Z_j)^2} && (4.28)
\end{aligned}
$$

Through linerization and expressed in matrix form:

$$\underbrace{\begin{pmatrix} L1 - L1_o \\ L2 - L2_o \\ P1 - P1_o \\ P2 - P2_o \\ I - I_o \end{pmatrix}}_{z} = \underbrace{\begin{pmatrix} \frac{\partial f}{\partial X_j} & \frac{\partial f}{\partial Y_j} & \frac{\partial f}{\partial Z_j} & \lambda_{L1} & 0 & -1 \\ \frac{\partial f}{\partial X_j} & \frac{\partial f}{\partial Y_j} & \frac{\partial f}{\partial Z_j} & \lambda_{L2} & -\lambda_{L2} & -\beta \\ \frac{\partial f}{\partial X_j} & \frac{\partial f}{\partial Y_j} & \frac{\partial f}{\partial Z_j} & 0 & 0 & 1 \\ \frac{\partial f}{\partial X_j} & \frac{\partial f}{\partial Y_j} & \frac{\partial f}{\partial Z_j} & 0 & 0 & \beta \\ 0 & 0 & 0 & 0 & 0 & 1 \end{pmatrix}}_{H} \underbrace{\begin{pmatrix} X_j - X_o \\ Y_j - Y_o \\ Z_j - Z_o \\ N_{L1} - N_{L1,o} \\ N_{WL} - N_{WL,o} \\ I - I_o \end{pmatrix}}_{x} \tag{4.29}$$

where,

$$\frac{\partial f}{\partial X_j} = \frac{X^k - X_j}{\rho_j^k} - \frac{X^l - X_j}{\rho_j^l} \tag{4.30}$$

$$\frac{\partial f}{\partial Y_j} = \frac{Y^k - Y_j}{\rho_j^k} - \frac{Y^l - Y_j}{\rho_j^l} \tag{4.31}$$

$$\frac{\partial f}{\partial Z_j} = \frac{Z^k - Z_j}{\rho_j^k} - \frac{Z^l - Z_j}{\rho_j^l} \tag{4.32}$$

and, subscript, o, refers to last state or approximated measurement transformed using the last states.

4.5 Stochastic Model

4.5.1 System Noise

The integer ambiguities are constant as long as a continuous phase lock is maintained. Therefore, the system noise for the ambiguity terms can take a zero value. In the event of cycle slips, a large variance can be assigned to the affected ambiguities, such that their previous states are not carried forward. Similarly, the positional terms can be assigned with a large number in case of mobile receiver, or a zero value, if

stationary. For a cycle-slip free kinematic platform, the process noise matrix has the following form:

$$\mathbf{Q_k} = \begin{pmatrix} \infty & 0 & 0 & 0 & 0 & 0 \\ 0 & \infty & 0 & 0 & 0 & 0 \\ 0 & 0 & \infty & 0 & 0 & 0 \\ 0 & 0 & 0 & 0 & 0 & 0 \\ 0 & 0 & 0 & 0 & 0 & 0 \\ 0 & 0 & 0 & 0 & 0 & E\{w_k^2\} \end{pmatrix} \tag{4.33}$$

The ionosphere system noise, $E\{w_k^2\}$, can be modelled using one of the random process models described in the previous section. In the implementation used herein, the Gauss-Markov process, according to Equation 4.20, is applied.

4.5.2 Measurement Noise

The stochastic behaviour of double difference GPS measurements is a function of constant receiver hardware noise, and elevation and distance dependent atmospheric errors. Further, GPS measurements are often treated as uncorrelated quantities. Under the influence of AS, most manufacturers reconstruct the L2-band measurements with the aid of un-encrypted L1-band measurements that yield a strong correlation between them (Tiberius and Kenselaar, 2000). Correlated measurements would have less information content than the statistically independent ones, and ignoring the correlation property would lead to over optimistic results.

Hardware Dependence

The hardware measurement error, symbolized by ϵ in the fundamental GPS observation Equations, 2.3 and 2.4, can't be easily isolated from other error sources. The one-way hardware measurement noise can only be extracted under a controlled environment such as an anechoic chamber or using a simulator. Short of that, the hardware noise is often estimated from double differencing the actual observed GPS measurements over a zero-baseline. The estimated hardware noise is still contaminated by the elevation dependent errors that will be separated in the stochastic analyses (see Chapter 5) .

Distance Dependence

The double difference observations are an effective way of removing correlated error sources. However, the distance dependent errors remain. The dominant baseline length dependencies are the orbital, ionosphere, and tropospheric errors. The broadcast orbit available in real-time is based on extrapolation of satellite trajectory tracked by the five worldwide monitoring stations with 3 m accuracy (Rothacher and Mervert, 1996). The impact on relative positioning uncertainty by the orbital error can be approximated by Equation 4.34 (Bauersima, 1983), which yields about 0.12 ppm or 12 mm over a 100 km long baseline.

$$\frac{\delta x(m)}{\delta X(m)} \approx \frac{d(km)}{D(km)} \tag{4.34}$$

where, δx is the positional error, δX the orbital error, d the baseline distance, and D the satellite altitude ($\approx$ 25000 km).

Under active ionosphere conditions, the ionospheric effect can be as much as 10 to 50 times greater than the orbital effect. The tropospheric effect is influenced by the local ambient atmospheric environment and may depart from the linear distance assumption.

Both the geometrical and ionospheric effects are linearly dependent on the baseline distance d, i.e.

$$\sigma^2_{geom} \propto d \tag{4.35}$$

$$\sigma^2_{iono} \propto d \tag{4.36}$$

Elevation Dependence

One-way GPS measurements are subjected to elevation-dependent errors. Tropospheric refraction is responsible for increasingly larger range delays and noise scatters as the zenith angle approaches the horizon. However, the largest contributor is the antenna gain, which decreases with decreasing elevation. The elevation dependence can be characterized by the signal-to-noise ratio; however, not all data formats sufficiently support it, if at all. For example the widely used format, Receiver INdependent EXchange, RINEX (Gurtner and Mader, 1990) with a scale of 0 to 9 may not provide a sufficient resolution. Moreover, different GPS receiver manufacturers adhere to their own definitions making receiver mixing problematic.

Two variations of an elevation weighting scheme are presented here. The first applies an exponential function described by three constants, a, b and c (Tiberius,

1998). For example a one-way observation to Satellite k at Station i is expressed by:

$$\sigma(z_i^k) = a + b \cdot exp(\frac{z_i^k}{c}) \tag{4.37}$$

CODE, one of the IGS Analysis Centres, tested many different elevation-dependent weighting functions for the phase observations and adopted a simple cosine function, Equation 4.38, for their routine global data analysis (Rothacher et al, 1997). In this development, the same elevation-dependent weighting scheme is applied.

$$W(z_i^k) = cos^2(z_i^k) \tag{4.38}$$

The ionospheric elevation dependence is somewhat cumbersome to determine as the angles are measured at the shell pierce points located at a nominal altitude of 400 km and not at the station's topocentred zenith. Furthermore, a unit weight assumption at each pierce zenith would not hold as the free electron content varies with respect to the sun-fixed reference frame. Therefore, the ionosphere elevation dependence will not be considered, consistent with other authors, e.g. (Bock et al, 1986), (Goad and Yang, 1994), and (Odijk, 1999).

4.5.3 Measurement (Co)Variance Matrix, R

Four measurements, between two common satellites and two stations, form one double difference observable. The zenith angle, z, of a commonly viewed satellite by an individual station varies with respect to other stations due to the station separations, d. Furthermore, the differential atmospheric errors increase with increasing d. In order to properly weigh these effects, a combination of both distance and elevation

dependence with a double difference operator, $\mathbf{D}$, is proposed here. The corresponding measurement type and ionospheric pseudo-observable (co)variance blocks take the form

$$R_{Mi,Mj} = (\sigma^2_{meas} + \sigma^2_{geom})\mathbf{DWD^T} \tag{4.39}$$

$$R_{I,I} = \sigma^2_{iono}\mathbf{DD^T} \tag{4.40}$$

where, Mi, Mj are the double difference observation (co)variance matrices of measurement types M, i.e. $M = P$ for pseudorange, or $M = L$ for carrier phase; i and j are the corresponding frequencies, i.e. $L = 1$, or $L = 2$; and, σ^2_{meas} is the measurement error, nominally at $\sigma_{L1} = \sigma_{L2} = 3$ mm, and $\sigma_{P1} = \sigma_{P2} = 0.3$ m.

$$\mathbf{D} = \underbrace{\left(\begin{array}{ccccc|ccccc} +1 & -1 & 0 & 0 & \dots & -1 & +1 & 0 & 0 & \dots \\ +1 & 0 & -1 & 0 & \dots & -1 & 0 & +1 & 0 & \dots \\ +1 & 0 & 0 & -1 & \dots & -1 & 0 & 0 & +1 & \dots \\ \vdots & \vdots & \vdots & \vdots & \ddots & \vdots & \vdots & \vdots & \vdots & \ddots \end{array}\right)}_{\text{Satellites } k,l,m,n\text{... at Sta. } i \quad \text{Satellites } k,l,m,n\text{... at Sta. } j} \tag{4.41}$$

$$\text{Diag } \mathbf{W} = \begin{bmatrix} W(z_i^k) & W(z_i^l) & W(z_i^m) & W(z_i^n)\dots & W(z_j^k) & W(z_j^l) & W(z_j^m) & W(z_j^n)\dots \end{bmatrix}$$

The superscripts, $k, l, m, n, ...$ and subscripts, i, j denote Satellites and Stations, respectively. Satellite k and Station i are the respective references. The double difference operator $\mathbf{D}$ (Equation 4.41) is structured such that the first column, k, on both sides, is the reference satellite.

The complete $\mathbf{R}$ takes the form:

$$\mathbf{R} = \begin{pmatrix} R_{L1,L1} & R_{L1,L2} & R_{L1,P1} & R_{L1,P2} & 0 \\ R_{L2,L1} & R_{L2,L2} & R_{L2,P1} & R_{L2,P2} & 0 \\ R_{P1,L1} & R_{P1,L2} & R_{P1,P1} & R_{P1,P2} & 0 \\ R_{P2,L1} & R_{P2,L2} & R_{P2,P1} & R_{P2,P2} & 0 \\ 0 & 0 & 0 & 0 & R_{I,I} \end{pmatrix} \tag{4.42}$$

In the next chapter, the stochastic analyses indicate a strong measurement correlation property between dual-frequency phase measurements, due to the reconstruction of L2 base-band measurement under the AS conditions. Therefore, the $R_{L1,L2}$ and $R_{L2,L1}$ blocks are not nulled. No detectable correlations were found between Ashtech Z-XII's code and phase measurements, and between dual-band code measurements. The stochastic analyses are discussed in the next chapter. Due to the absence of cross-correlation properties, $R_{L1,P1}$, $R_{L1,P2}$, $R_{L2,P1}$, $R_{L2,P2}$, and $R_{P1,P2}$ blocks are set to null. The double difference measurement (co)variance matrix, $\mathbf{R}$ in Equation 4.42, now simplifies to

$$\mathbf{R} = \begin{pmatrix} R_{L1,L1} & R_{L1,L2} & 0 & 0 & 0 \\ R_{L2,L1} & R_{L2,L2} & 0 & 0 & 0 \\ 0 & 0 & R_{P1,P1} & 0 & 0 \\ 0 & 0 & 0 & R_{P2,P2} & 0 \\ 0 & 0 & 0 & 0 & R_{I,I} \end{pmatrix} \tag{4.43}$$

4.6 Ambiguity Resolution: The LAMBDA Method

There are no standard methods for ambiguity resolution. However, most have three components: 1) integer search, 2) validation, and 3) ambiguity fixing. The float ambiguities and their (co)variances are readily available and extracted from the Kalman Filter (Equations 4.7 and 4.8). These are subsequently entered into the integer ambiguity resolution process.

4.6.1 Decorrelation Transformation

The integer search method used herein is the Least-squares AMBiguity Decorrelation Adjustment, LAMBDA, developed by the Delft Geodetic Computing Centre (Teunissen, 1993). GPS carrier phase ambiguities are typically highly correlated over a short time span due to a small change of satellite constellation. Therefore, the elongated integer search space defined by the (co)variance matrix can stretch over a considerable range of cycles as a result of low precision in each of the ambiguities. Prior to integer search, the LAMBDA method optimizes the stochastic structure of the ambiguities by applying a decorrelating Z-transformation to minimize the correlation and to improve precision, while retaining the integer characteristics. Standard diagonalization is not permitted due to the integer preserving requirements. The admissible transformation matrix Z must satisfy three conditions: 1) all entries must be integers; 2) all entries of Z^{-1} must be integers; and 3) the determinant of Z is $\pm$ 1. Thus,

$$\hat{z} \;=\; Z^T \hat{N} \tag{4.44}$$

$$Q_{\hat{z}} = Z^T Q_{\hat{N}} Z \tag{4.45}$$

The transformed space will be not be a complete sphere because of the integer requirements. Hence, the off-diagonal elements are near zero. Decorrelation is not a prerequisite for the ambiguity search; however, it is recommended and will improve the numerical efficiency and reliability of the estimates.

4.6.2 Integer Search

The double difference ambiguities are initially estimated as real quantities with assumed normal distributions. These are mapped from n-dimensional R space to n-dimensional Z space using a mapping function, $F : R^n \mapsto Z^n$. Because of the discrete nature of the Z^n space, the relationship between R^n and Z^n is not one-to-one, but many-to-one. This implies that there will be many sets of float ambiguities that map to one set of integer ambiguities. A subspace $S_z \subset R^n$ that maps to an identical integer set is referred as the *pull-in region* (Teunissen, 1999). Applying the pull-in region, the explicit expression for the ambiguity estimator reads

$$\check{z} = \sum_{z \in Z^n} z s_z(\check{z}) \text{ with } s_z(\hat{z}) = \begin{cases} 1 & \text{if } \hat{z} \in S_z \\ 0 & \text{otherwise} \end{cases} \tag{4.46}$$

A class of admissible integer estimators has the pull-in regions possessing the following three properties:

Property 1: The union of entire pull-in regions covers the entire R^n space:

$$\cup_{z \in Z} S_z = R^n \quad \text{(No Gap)} \tag{4.47}$$

Property 2: There are no overlaps among the pull-in regions, such that each pull-in region maps to a unique integer:

$$S_{z_1} \cup S_{z_2} = \emptyset, \forall z_1, z_2 \in Z^n, z_1 \neq z_2 \quad \text{(No Overlap)} \tag{4.48}$$

Property 3: Remove-Restore The mapping of $F : R^n \mapsto Z^n$ is translation-invariant, implying that shifting by an integer to the float ambiguity is affected by the same amount in the mapped integer ambiguity. The float integers are often large numbers, and this property enables the working of their fractional parts.

$$S_z = z + S_o, \forall z \in Z^n \quad \text{(Shift Invariant)} \tag{4.49}$$

where, S_o is pull-in region at the origin.

4.6.3 Admissible Integer Estimators

The following three estimators are admissible estimators that are commonly found in GPS applications:

Rounding

This is the simplest estimator that can be applied to two trivial cases: a scalar, and multivariate ambiguities with a diagonal (co)variance matrix. The integer ambiguities are simply rounded to the nearest integer using a rounding operator, [.], i.e.

$$\check{z}_i = [\hat{z}_i], \quad i = 1 \ldots n \tag{4.50}$$

Integer Least-squares

Unlike the deterministic standard least-squares in R^n space, the integer least-squares estimates require an exhaustive discrete search for the minimum norm. Often the search space is limited to a region bounded by an ellipsoid, in which the shape and the size are defined by the (co)variance matrix. Some algorithms utilize only the variances to define the search space, resulting in a larger and less efficient rectangular search space. The maximum possible number of search combinations for six satellites over a search window of ± 10 cycles amounts to $21^5 \approx 3.9E6$ (Lu, 1995). Including the off-diagonal entries, the search space resembles an ellipsoid and eliminates an unnecessary grid point search. The search region is given by

$$\min \|\hat{z} - \check{z}\|_{Q_{\hat{z}}^{-1}} < \chi^2 \tag{4.51}$$

The selected χ^2 value must be large enough that the search space contains at least one set of integers. This can be achieved by setting the χ^2 value to the square norm of rounded ambiguities. This will guarantee at least one and most probably not more than a few candidates. Further, setting χ^2 to the second smallest squared norm will guarantee at least two candidate sets.

Bootstrapping

Further computational efficiency is possible through *Sequential Conditional Least-squares*, where the ambiguity, z_n, is estimated sequentially and conditioned to previous estimated integer ambiguities, $\check{z}_{1,\ldots,n-1}$. Each integer is corrected by virtue of its correlation with the previous integers, and the search space shrinks with each successive ambiguity conditioning. Individual ambiguities are found by the following

search sequence:

$$\left\{ \begin{array}{lcl} (\hat{z}_1 - \check{z}_1)^2 & \leq & \sigma^2_{\hat{z}_1}\chi^2 \\ (\hat{z}_{2|1} - \check{z}_2)^2 & \leq & \sigma^2_{\hat{z}_{2|1}}(\chi^2 - (\hat{z}_1 - \check{z}_1)^2/\sigma^2_{\hat{z}_{2|1}}) \\ & \vdots & \\ (\hat{z}_{n|1,\ldots,(n-1)} - \check{z}_n)^2 & \leq & \sigma^2_{\hat{z}_{n|1,\ldots,(n-1)}}(\chi^2 - \sum_{j=1}^{n-1}(\hat{z}_{j|1,\ldots,(j-1)} - \check{z}_j)^2/\sigma^2_{\hat{z}_{j|1,\ldots,(j-1)}}) \end{array} \right\}$$

4.6.4 Validation

Once the set of integer solutions is obtained, the critical decision must be made: to accept or reject it. Here are the two validation conditions used in the implementation herein:

ADOP Test

The *Ambiguity Dilution of Precision* (ADOP), akin to the geometrical counterpart (GDOP), provides an indication of the quality of the estimated float ambiguity. In the implementation, integer ambiguity estimates are rejected if the ADOP is below 0.1 cycle. The tolerance setting is very much dependent on the stochastic weighting of the measurements and the tuning of the filter. Unlike the GDOP, defined as the trace of the (co)variance matrix (i.e. it does not take its correlation information into account), the ADOP applies the off-diagonal entries and is defined as (Teunissen and Odijk, 1997):

$$ADOP = det(Q_{\hat{z}})^{1/n} \tag{4.52}$$

Alternatively, the ADOP can also be obtained using the conditional variances:

$$ADOP = \prod_{i=1}^{n} \sigma^{1/n}_{\hat{z}_{i|I}} \tag{4.53}$$

Ratio Test

The most commonly used criterion is the ratio test between the quadratic residuals of best and the second sets of integers. If the ratio is above some tolerance, ε, the best set is accepted. In the present implementation, the ϵ is set to three. Some literatures falsely assume that the ratio has a Fisher, F-distribution[1] because the quadratic residuals from both sets are not statistically independent. The ratio test takes the form:

$$ratio = \frac{\|\hat{z}_2 - z_2\|_{Q_{\hat{z}_2}}}{\|\hat{z}_1 - z_1\|_{Q_{\hat{z}_1}}} < \varepsilon \tag{4.54}$$

4.6.5 Ambiguity Fixing

Once a reliable set of ambiguities is found by passing either the ADOP or the ratio tests, the integer ambiguities are accepted and constrained. Ambiguity fixing by means of parameter removal will improve the positional estimates. This approach yields a somewhat optimistic statistical estimate for the remaining unknown parameters, because the stochastic property of the fixed integers is ignored. According to the least-squares formulas, the constraint can be applied in the following manner (Lu, 1995):

$$\check{x}|\check{a}_n = \hat{x} - p_n(\hat{a}_n - \check{a}_n)p_{n,n} \tag{4.55}$$

$$P|\check{a}_n = P - p_n p_n^T p_{n,n}^{-1} \tag{4.56}$$

where, p_n is a row vector, $[P_{1,n}, P_{2,n}, P_{3,n}, \ldots, P_{n,n}]^T$, $p_{n,n}$ is a scalar element in matrix $P_{n,n}$, and n is the parameter to be removed.

[1] F-distribution is a ratio of two independent χ^2-distributions.

Note that the ambiguity validation implemented here is based on a binary decision over a complete set of ambiguities, either the widelane or the L1 ambiguities. This implies that ambiguities are either all accepted or rejected epoch-wise, and no partial fixing is performed.

4.7 Summary

The algorithms implemented in this research can be grouped into two modules. The first is the Kalman Filter. It deviates slightly from the traditional approach in that the parameters are iterated by the non-linear measurements using the Gauss-Newton Equations 4.12-4.14. The measurement noise accounts for station specific elevation dependence and the inter-station separation dependence. The measurements are corrected for tropospheric delay using the Modified Hopfield Model with standard atmospheric parameters. In the case of a cycle slip, the responsible satellite is detected by the innovation sequence, and a large weight is assigned to its corresponding entry in the system noise matrix. In the case of a loss or acquired satellite tracking, the corresponding row and column in the state vector ($\mathbf{x}$), system noise matrix ($\mathbf{Q}$), (co)variance matrix ($\mathbf{P}$), measurement weight matrix ($\mathbf{R}$), and the design matrix ($\mathbf{H}$), are adjusted accordingly by removal or insertion.

The second module is the Ambiguity Resolution using the LAMBDA decorrelation and search technique. Two best integer sets contained in the search space are estimated. The appropriate search space is defined by the χ^2. Their quadratic residual norms are compared. If the ratio and ADOP tests are passed, the first can-

didate set is accepted. In a recent publication, only one set of integer ambiguities is estimated, and the validation criteria is based strictly on the corresponding ADOP, that effectively improves the computational efficiency (Teunissen, 1999). Both test criteria will be evaluated in the next chapter. The 86 cm N_{WL} integers are resolved first. If successful, they are constrained and the more challenging 19 cm N_{L1} integer resolution is carried out.

Once both N_{L1} and N_{WL} integer ambiguities are successfully resolved, the N_{L2} integer ambiguities are derived by subtracting the first two, i.e. $N_{L2} = N_{L1} - N_{WL}$. This enables the forming of precise integer constrained ionosphere-free (L3) observables. This is particularly useful for long baselines (>100 km), where the ionospheric effects are effectively removed.

The algorithm implemented in this thesis is best described conceptually by the following flowchart shown in Figure 4.2.

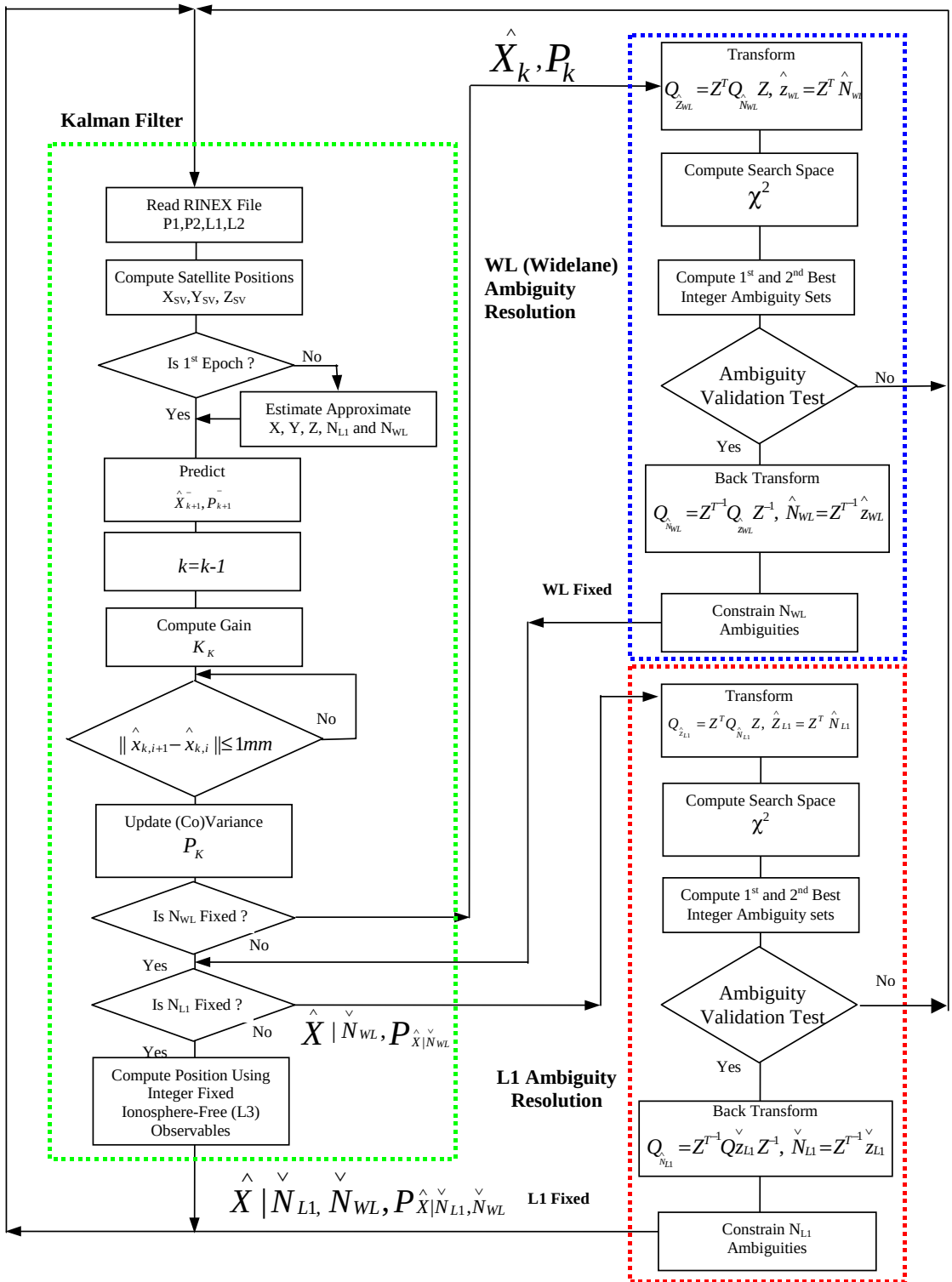

Figure 4.2: Ionosphere Weighted GPS Carrier Phase Ambiguity Resolution Flowchart

Chapter 5

Stochastic Analyses

This chapter examines the stochastic nature of the GPS measurements themselves and atmospheric effects over various baseline lengths. This stochastic approach, combined with the functional model described in the previous chapter, is entered into the estimation of optimal float ambiguity solution. Optimal float ambiguity estimates and the correctness of their (co)variances are prerequisites to reliable and efficient integer ambiguity resolution.

The code and phase measurements are contaminated by various errors as described by the observation models, Equations 2.3 and 2.4. The stochastic behaviour of the actual phase measurement noise and the atmospheric effects are estimated using the double difference observables. These enables the highest precision by constraining the integer ambiguities and the station coordinates. Such precision would not be possible using zero or single difference observables, due to the non-integer nature of the corresponding ambiguities. The constrained station coordinates and the double differenced integer ambiguities are computed using the Bernese GPS Processor Software, V4.2 (Rothacher and Mervert, 1996) with the IGS final precise orbits.

The stochastic analyses are separated into two parts. The first examines the actual measurement characteristics in the absence of external errors, such as the atmospheric and orbital effects, utilizing the double difference zero-baseline observ-

ables. The zero-baseline data sets were recorded at Station Bora on Sept 3, 2000 over a one-hour period at a rate of 1Hz. The second part examines the distance dependence errors using the two 24-hour (April 7 and June 21, 2000) SWEPOS network data sets, decimated to a 15-second sampling rate. Eight stations are selected forming various baseline lengths between 35 km and 407 km. In an effort to simulate real-time applications, broadcast orbits are used.

The Dorne Margolin antenna element used in the data collection has a vertical offset between the L1 and L2 phase centres. The calibrated offsets are taken from the U.S. National Geodetic Survey (NGS)[1] and applied in the computations to reduce the differential phase centering error.

The distance dependent errors can be categorized into two groups - the geometric and ionospheric effects. The term *geometric* is appropriate as it is a combination of all geometrical error terms, including the tropospheric and orbital errors. The geometrical effect equivalently affects all GPS measurements. In contrast, the ionospheric effect is dispersive, implying it is radio frequency dependent, and the signs are opposite for the code and phase measurements.

Direct access of the L1 and L2 P-code measurements by unauthorized users is not possible in presence of A/S. To differentiate the reconstructed P1 and P2 counterparts, they are symbolized by P_r1 and P_r2.

[1]Available from http://www.ngs.noaa.gov/ANTCAL

5.1 Data Set Characterization

A satellite cutoff angle of 15° is used in all of data processing throughout this thesis. This angle was chosen to minimize the multipath and atmospheric effects and to lessen the cycle slip occurrences that dominate at lower elevation angles. Furthermore, the precision of the GPS positions is very much dependent on the number of satellites being tracked and the spatial distribution of these satellites. A simple measure of precision can be expressed by taking the norm of the single model's 3-D positional and clock variances (Leick, 1990). This measure is referred to the *Geometry Dilution of Precision* (GDOP).

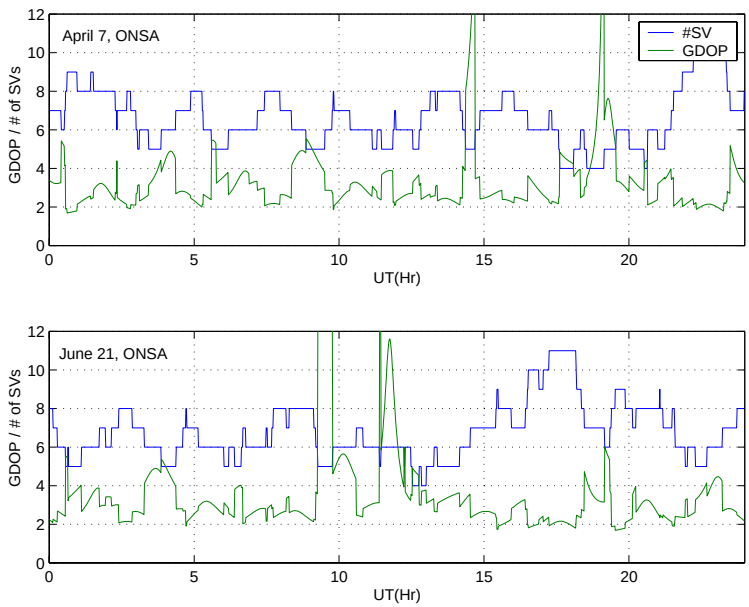

Figure 5.1: GDOP and Number of Satellites Tracked Above 15° at Station Onsala On April 7 and June 21

Figure 5.1 shows the number of satellites being tracked above 15° and the resultant

GDOP for both April 7 and June 21 at Station Onsala (ONSA). Note that the GPS satellites rise and set about four minutes early daily. The five hour lateral shift in time shown between the plots is a direct result of the 75 day difference between April 7 and June 21. These plots are similar, but not completely identical due to the ongoing orbit adjustments.

The GDOP is typically between two and four. And the number of satellites is typically no less than five. There are periods of extreme GDOP spikes of up to 20, i.e. at 14 Hr on April 7 and 09 Hr on June 21. A total of ten satellites is in-view during these periods, but only half of them are above the cut-off angle.

5.2 Measurements

5.2.1 Elevation Dependence

The elevation[2] dependence characteristics in the zero difference observables are extracted from the double difference counterparts with an assumption that the elevation dependence reaches a steady-state above 50°, Equations 5.1, 5.2, and 5.3. This is the same scheme used by Raquet(1998), except that a lower 50° limit was chosen due to a limited number of samples available above this elevation, i.e. 3% of over 20000 total samples. The double differenced code and phase measurement errors over a zero-baseline are tabulated in bins of 5° intervals up to 50° (Table 5.1), and reduced

[2]Elevations are referenced to the horizon, unlike in previous chapters where the angles z are referenced to the zenith

to a zero difference measurement error (Table 5.2).

$$(\sigma_{ij}^{kl})^2 = (\sigma_i^k)^2 + (\sigma_i^l)^2 + (\sigma_j^k)^2 + (\sigma_j^l)^2 \tag{5.1}$$

For a zero-baseline, $i = j$, and let k be the high reference satellite above 50°,

$$(\sigma_i^l)^2 = \frac{(\sigma_{ij}^{kl})^2 - 2(\sigma^*)^2}{2} \tag{5.2}$$

where, the steady-state constant $(\sigma^*)^2$ is the variance of double difference between two high satellites, m and n, above 50°,

$$(\sigma^*)^2 = (\sigma_{ij}^{mn})^2/4 \tag{5.3}$$

There were no short baselines (a few metres) available from the SWEPOS network for the elevation dependence analyses. However, a zero baseline data set collected by Ashtech Z-XII receivers was available. The multipath effects induced on the common antenna are completely removed by differencing. As a result the computed zero difference standard deviations shown in Table 5.2 are optimistic (Teunissen, 2001). These values are later found to be inefficient for ambiguity resolution. A more conservative and widely accepted zenithal standard deviation of 3 mm for both L1 and L2 carrier phase, and 30 cm for the L1 and L2 P-code are applied in the ambiguity resolution implementation.

In theory, the elevation weighting can be modelled from the measurement standard deviations as a function of elevation angle from the tabulated data (Table 5.2). Such a rigorous approach is again futile in the absence of multipath. Therefore, a more traditional cosine weight function (Equation 4.38) is used in the implementation herein.

Table 5.1: Standard Deviation of Double Difference Measurements

Elevation	σ_{L1} (mm)	σ_{L2} (mm)	σ_{C1} (m)	σ_{P_r1} (m)	σ_{P_r2} (m)
$05^\circ - 10^\circ$	1.277	2.987	0.269	0.487	0.475
$10^\circ - 15^\circ$	0.678	1.340	0.173	0.429	0.442
$15^\circ - 20^\circ$	0.565	1.046	0.150	0.410	0.424
$20^\circ - 25^\circ$	0.472	0.963	0.149	0.389	0.401
$25^\circ - 30^\circ$	0.388	0.823	0.123	0.344	0.343
$30^\circ - 35^\circ$	0.346	0.624	0.105	0.262	0.257
$35^\circ - 40^\circ$	0.309	0.488	0.098	0.192	0.188
$40^\circ - 45^\circ$	0.272	0.418	0.103	0.159	0.154
$45^\circ - 50^\circ$	0.263	0.363	0.110	0.136	0.131
$> 50^\circ$	0.244	0.340	0.075	0.119	0.105

Table 5.2: Standard Deviation of Zero Difference Measurements

Elevation	σ_{L1} (mm)	σ_{L2} (mm)	σ_{C1} (m)	σ_{P_r1} (m)	σ_{P_r2} (m)
$05^\circ - 10^\circ$	0.895	2.105	0.187	0.339	0.332
$10^\circ - 15^\circ$	0.464	0.932	0.117	0.297	0.308
$15^\circ - 20^\circ$	0.380	0.720	0.099	0.284	0.295
$20^\circ - 25^\circ$	0.311	0.659	0.099	0.268	0.278
$25^\circ - 30^\circ$	0.246	0.557	0.079	0.236	0.237
$30^\circ - 35^\circ$	0.212	0.407	0.064	0.175	0.174
$35^\circ - 40^\circ$	0.181	0.300	0.059	0.122	0.122
$40^\circ - 45^\circ$	0.149	0.242	0.063	0.095	0.095
$45^\circ - 50^\circ$	0.140	0.192	0.068	0.075	0.076
$> 50^\circ$	0.122	0.170	0.038	0.059	0.052

5.2.2 Measurement Cross-Correlation

Three double difference pairs at high-high ($> 50^\circ$), high-mid ($> 50^\circ$ versus $15^\circ - 40^\circ$), and high-low ($> 50^\circ$ versus $< 15^\circ$) satellite elevation combinations are evaluated for any presence of cross-correlation between L1 and L2, C1 and P_r2, and, P_r1 and P_r2 measurements. Any presence of cross-correlation between two measurement types can be detected by comparing their standard deviations against the standard deviation of their differences according to Equation 5.4. If no correlation exists, the

term $\sigma^2_{A,B}$ would be zero. The correlation coefficients are subsequently computed by applying Equation 5.5. The numerical statistics are shown in Table 5.3, and the correlation coefficients are shown in Table 5.4. The computed correlation coefficients are negligible between the C1 and P_r2, and P_r1 and P_r2 code measurements. Both P-codes are reconstructed, and there appears to be surprisingly very little or no correlation between them. The reason for this is unclear. The correlation between the L1 and L2, however, is quite significant at $\rho \approx 0.5$ as a result of the cross-correlation technique to reconstruct the L2 carrier phase. No detectable correlations are found between code and carrier phase measurements. The double difference measurement noises of L1, L2, C1, P_r1, and P_r2, over the zero-baseline are shown in Figures A.1, A.2, and A.3 in Appendix A. The Ashtech Z-XII correlation coefficients found here are consistent with other publications such as Tiberius et el. (1999) and Tiberius and Kenselaar (2000).

$$\sigma^2_{A-B} = \sigma^2_A + 2\sigma_{A,B} + \sigma^2_B \tag{5.4}$$

And the correlation coefficient, ρ,

$$\rho = \frac{\sigma_{A,B}}{\sigma_A \ \sigma_B} \tag{5.5}$$

Table 5.3: Summary of Double Difference Noise Level

Elevation†	σ_{L1} (mm)	σ_{L2} (mm)	σ_{C1} (m)	σ_{P_r1} (m)	σ_{P_r2} (m)	σ_{L1-L2} (mm)	σ_{C1-P_r2} (m)	$\sigma_{P_r1-P_r2}$ (m)
High-Low	0.682	1.225	0.181	0.440	0.425	1.063	0.463	0.588
High-Mid	0.514	1.003	0.121	0.409	0.419	0.906	0.443	0.612
High-High	0.255	0.377	0.107	0.144	0.135	0.334	0.174	0.195

†$High > 40° > Mid > 15° > Low$

Table 5.4: Summary of Correlation Coefficients

Elevation	$L1, L2$	$C1, P_r2$	P_r1, P_r2
High-Low	0.50	0.05	0.04
High-Mid	0.44	-0.06	-0.01
High-High	0.50	-0.02	0.02

5.2.3 Measurement Time Correlation

Applying the definition of *Stationary Autocorrelation*, Equation 5.6 (Strang and Borre, 1997), the time correlation effect of all measurement types are plotted in Figure 5.2. The L1 carrier phase shows no sign of time correlation from the 1 Hz data. However, there exist several seconds of correlation in the L2 carrier phase and in both P-codes on L1 and L2 frequency bands. The C/A-code exhibits a long time decay of approximately 60 seconds. The manufacturer's intentional smoothing using the carrier phase likely causes this. This is indicated by its lower measurement standard deviations compared to the P_r-code on both L1 and L2, i.e. 18 cm versus 44 cm of P-code (L1) in the high and low satellite elevation pair (referring to Table 5.3). Typically, the C/A-code multipath effect dominates at low elevations. This is not the case if smoothed by the less susceptible carrier phase. Both P_r1 and P_r2

exhibit a small time correlation of about several seconds, and it is not clear if some smoothing or any have been applied. In order to simplify the algorithms, the C/A-code measurements are not utilized in the implementation herein. By doing so, the time correlation characteristics are assumed absent from the measurements.

$$Rx(\tau) = E\{x(t)x(t+\tau)^T\} \tag{5.6}$$

Where, $\tau = t_2 - t_1$, is the time difference.

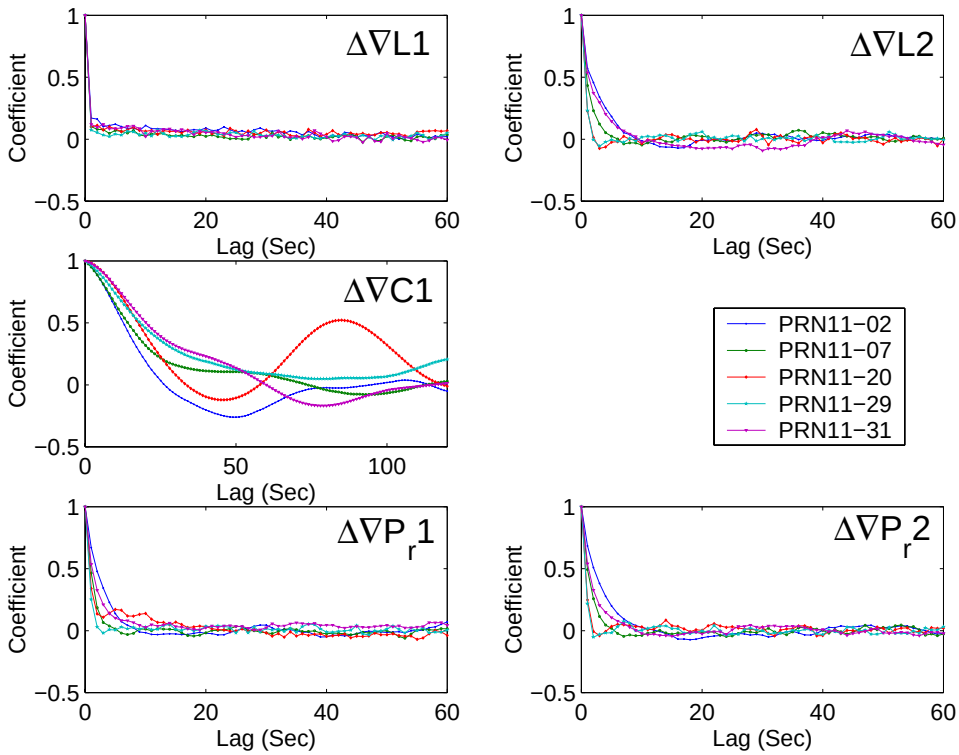

Figure 5.2: Double Difference Time Correlations

5.3 Distance Dependence

The dominant distance dependent errors are the orbital, tropospheric, and ionospheric effects. The first two can be extracted in lump using the ionosphere-free L3 linear combination. The third can be effectively extracted from the geometry-free L4 linear combination. From the eight selected SWEPOS stations, a total of 21 baselines of various distances are formed for analyses. These baselines are summarized in Table 5.5.

Table 5.5: Summary of Baselines Evaluated

From	*To*	*Length* (km)	ΔHgt (m)	*From*	*To*	*Length* (km)	ΔHgt (m)
ONSA	GOTE	35	11	KARL	LEKS	162	364
GOTE	BORA	55	163	JONH	KARL	192	-146
BORA	JONH	67	40	BORA	KARL	196	-106
ONSA	BORA	68	174	GOTE	KARL	213	58
GOTE	VANE	110	113	ONSA	KARL	246	69
VANE	KARL	119	-55	VANE	LEKS	277	308
BORA	VANE	120	-50	JONH	LEKS	335	218
GOTE	JONH	125	204	BORA	LEKS	354	258
ONSA	JONH	134	214	GOTE	LEKS	375	421
ONSA	VANE	145	124	ONSA	LEKS	407	433
JONH	VANE	159	-91				

5.3.1 Geometrical Errors

Constraining the double difference integer ambiguities and the coordinates of both satellites and stations on ionosphere-free (L3) double difference carrier phase observables yield geometrical errors that include both tropospheric and broadcast orbital effects. Both April 7 and June 21 data sets have been evaluated with and without the tropospheric delay model. The distance dependence parameters, expressed in

unit of *parts-per-million* (ppm), are estimated using least-squares method constraining to the origin. For simplicity, the elevation dependence was ignored. Both days show a consistent 0.8∼0.9 ppm of geometrical error when no model is applied. Deviations of a few centimetres (<5 cm) from the linear trend are detected, and these are direct consequences of large station height differences (>200 m) (Figures 5.3 and 5.4). The Modified Hopfield model (Equation 3.29) with standard sets of meteorological parameters (Equations 3.24, 3.25, and 3.26) appears to be an effective means of reducing the tropospheric effects, resulting in a geometrical error approximately in the 0.1 $\sim$ 0.2 ppm range. Table 5.6 and Table 5.7 show the numerical estimated, least-squares fitted, and residual values for both days.

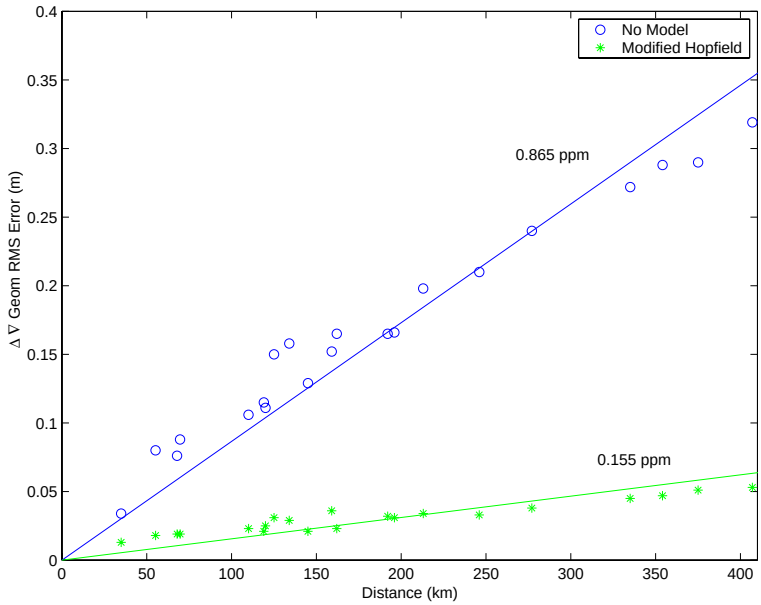

Figure 5.3: Double Difference Geometrical Error, April 7

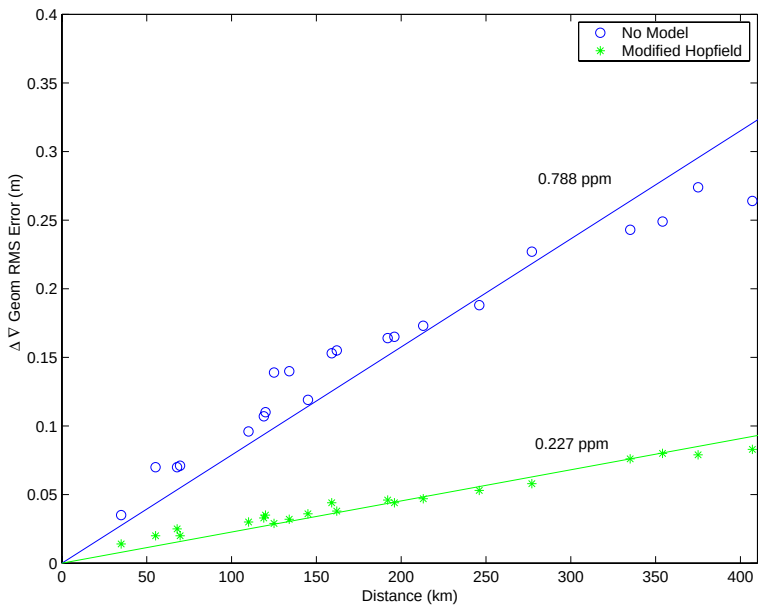

Figure 5.4: Double Difference Geometrical Error, June 21

Table 5.6: Double Difference Geometrical Errors, April 7 (24Hr)

	None			**Modified Hopfield**		
Dist(km)	Estimate(m)	Fitted[1](m)	Residual(m)	Estimate(m)	Fitted[2](m)	Residual(m)
35	0.034	0.030	0.004	0.013	0.005	0.008
55	0.080	0.048	0.032	0.018	0.009	0.009
68	0.076	0.059	0.017	0.019	0.011	0.008
70	0.088	0.060	0.028	0.019	0.011	0.008
110	0.106	0.095	0.011	0.023	0.017	0.006
119	0.115	0.103	0.012	0.021	0.018	0.003
120	0.111	0.104	0.007	0.025	0.019	0.006
125	0.150	0.108	0.042	0.031	0.019	0.012
134	0.158	0.116	0.042	0.029	0.021	0.008
145	0.129	0.125	0.004	0.021	0.023	-0.002
159	0.152	0.138	0.014	0.036	0.025	0.011
162	0.165	0.140	0.025	0.023	0.025	-0.002
192	0.165	0.166	-0.001	0.032	0.030	0.002
196	0.166	0.170	-0.004	0.031	0.030	0.001
213	0.198	0.184	0.014	0.034	0.033	0.001
246	0.210	0.213	-0.003	0.033	0.038	-0.005
277	0.240	0.240	0.000	0.038	0.043	-0.005
335	0.272	0.290	-0.018	0.045	0.052	-0.007
354	0.288	0.306	-0.018	0.047	0.055	-0.008
375	0.290	0.325	-0.035	0.051	0.058	-0.007
407	0.319	0.352	-0.033	0.053	0.063	-0.010
			RMS=0.022			RMS=0.007

Note: Fitted values use the least-squares estimated distance dependence parameter,
1) 0.865 ppm, and 2) 0.155 ppm.

Table 5.7: Double Difference Geometrical Errors, June 21 (24Hr)

	None			**Mododified Hopfield**		
Dist(km)	Estimate(m)	Fitted[1](m)	Residual(m)	Estimate(m)	Fitted[2](m)	Residual(m)
35	0.035	0.028	0.007	0.014	0.008	0.006
55	0.070	0.044	0.026	0.020	0.013	0.007
68	0.070	0.054	0.016	0.025	0.015	0.010
70	0.071	0.055	0.016	0.020	0.016	0.004
110	0.096	0.087	0.009	0.030	0.025	0.005
119	0.107	0.094	0.013	0.033	0.027	0.006
120	0.110	0.095	0.015	0.035	0.027	0.008
125	0.139	0.099	0.040	0.029	0.028	0.001
134	0.140	0.106	0.034	0.032	0.030	0.002
145	0.119	0.114	0.005	0.036	0.033	0.003
159	0.153	0.125	0.028	0.044	0.036	0.008
162	0.155	0.128	0.027	0.038	0.037	0.001
192	0.164	0.151	0.013	0.046	0.044	0.002
196	0.165	0.154	0.011	0.044	0.045	-0.001
213	0.173	0.168	0.005	0.047	0.048	-0.001
246	0.188	0.194	-0.006	0.053	0.056	-0.003
277	0.227	0.218	0.009	0.058	0.063	-0.005
335	0.243	0.264	-0.021	0.076	0.076	-0.000
354	0.249	0.279	-0.030	0.080	0.080	-0.000
375	0.274	0.296	-0.022	0.079	0.085	-0.006
407	0.264	0.321	-0.057	0.083	0.092	-0.009
			RMS=0.023			RMS=0.005

Note: Fitted values use the least-squares estimated distance dependence parameter,
1) 0.788 ppm, and 2) 0.227 ppm.

5.3.2 Ionospheric Errors

The integer ambiguity and the positional constraints are applied to double difference geometry-free L4 observables. Apart from the hardware noise, multipath effect, and differential L1/L2 phase centering aberrations, the resultant estimates are slant ionospheric delay errors and referenced to the L1 carrier frequency.

Figure 5.5 shows the ionospheric errors without ionospheric corrections being applied over the 145 km baseline. The left and right columns are from the respective April 7 and June 21 days. The top row shows the estimated double difference slant ionospheric delays at a 15-second rate over 24 hours. There are multiple data points per epoch, representing all per-epoch ionospheric slant errors. The bottom row shows the per-epoch maximum unsigned ionospheric delay over the baseline length in ppm. The ppm's inferred here are actual ionospheric delays in the range domain.

One can clearly see that the ionospheric condition fluctuates greatly on April 7. For example, the maximum per-epoch slant ionospheric errors are between 5 and 15 ppm during the first and last few hours of April 7. And the maximum per-epoch ppm values over the remaining day are between 1 and 3 ppm. For the less active day, on June 21, the ionospheric condition is consistently less than 4 ppm over the entire day.

The RMS values of 0.271 m (April 7) and 0.151 m (June 21) shown on the top pair of graphs are the averages of all double difference slant errors in metres over the two twenty-four hour periods. As such, it may not be representative of

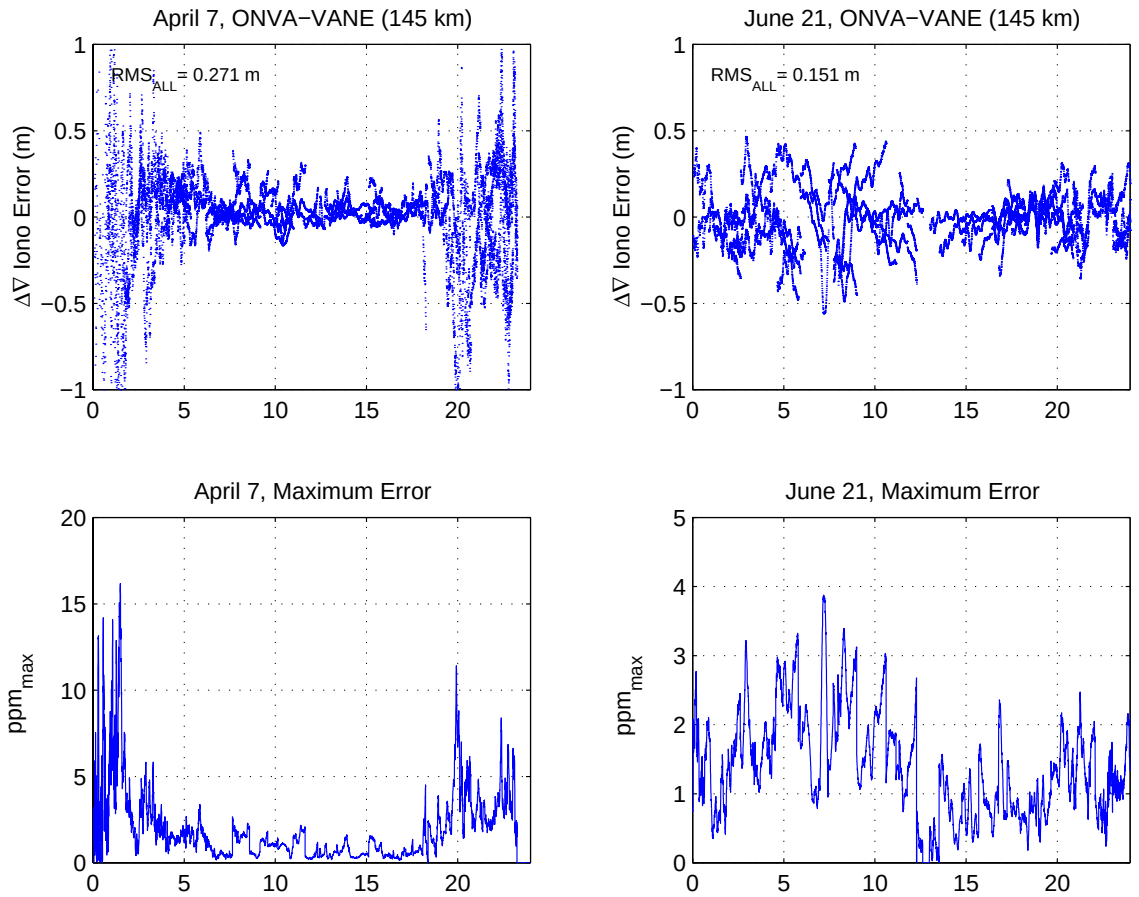

Figure 5.5: Double Difference Ionospheric Error, ONSA-VANE (145 km)

the ionospheric condition, especially when active. However, in order to generalize the distance dependence of the ionospheric dispersion, the 24 hour averaged RMS values from all 21 baselines are fitted linearly using the least-squares method and constraining to the origin (see Figures 5.6 and 5.7). The estimated line-slope parameter is expressed in ppm.

The ionospheric errors are evaluated for a comparison in three different ways for both days (Figures 5.7 and 5.6). The first has no model correction applied. The sec-

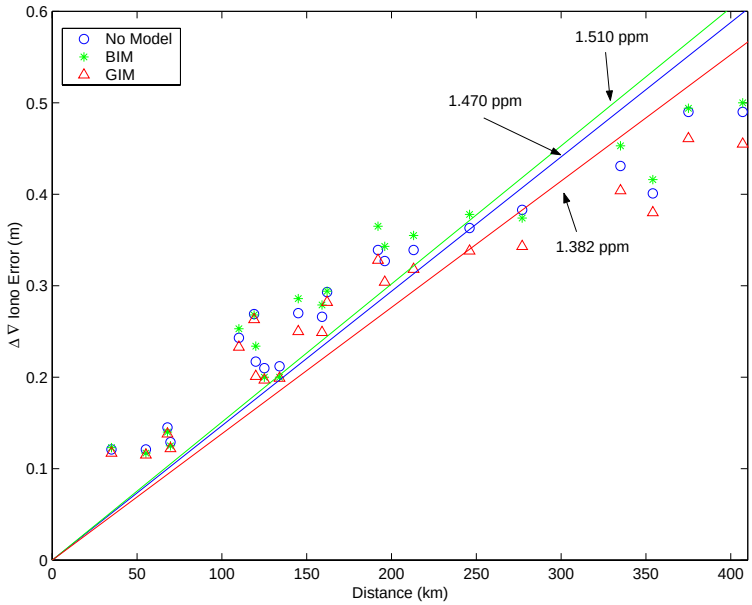

Figure 5.6: Double Difference Ionospheric Error, April 7

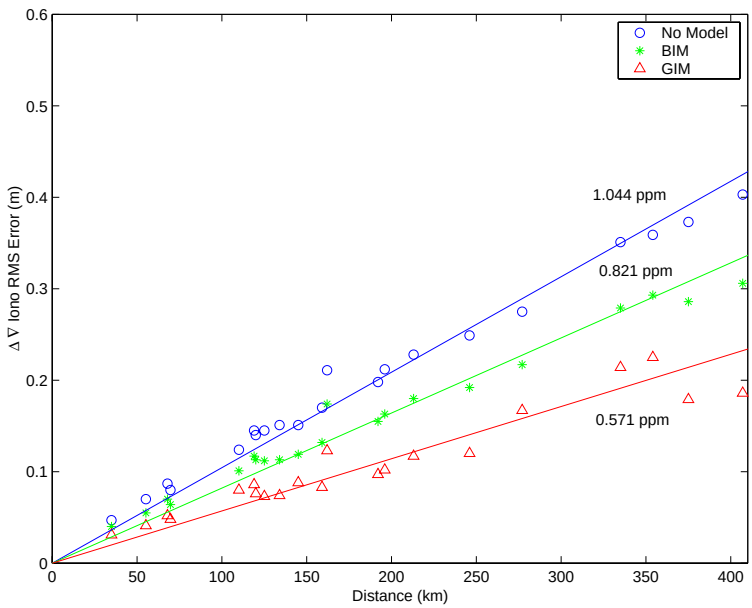

Figure 5.7: Double Difference Ionospheric Error, June 21

Table 5.8: Double Difference Ionosphere Error, April 7 (24Hr)

	None			**BIM**			**GIM**		
Dist(km)	Est(m)	Fit[1](m)	Res(m)	Est(m)	Fit[2](m)	Res(m)	Est(m)	Fit[3](m)	Res(m)
35	0.121	0.051	0.070	0.123	0.053	0.070	0.117	0.048	0.069
55	0.121	0.081	0.040	0.117	0.083	0.034	0.115	0.076	0.039
68	0.145	0.100	0.045	0.140	0.103	0.037	0.138	0.094	0.044
70	0.129	0.102	0.027	0.125	0.105	0.020	0.122	0.096	0.026
110	0.243	0.162	0.081	0.253	0.166	0.087	0.233	0.152	0.081
119	0.269	0.175	0.094	0.268	0.180	0.088	0.263	0.164	0.099
120	0.217	0.176	0.041	0.234	0.181	0.053	0.201	0.166	0.035
125	0.210	0.184	0.026	0.200	0.189	0.011	0.197	0.173	0.024
134	0.212	0.197	0.015	0.200	0.202	-0.002	0.199	0.185	0.014
145	0.270	0.213	0.057	0.286	0.219	0.067	0.250	0.200	0.050
159	0.266	0.234	0.032	0.279	0.240	0.039	0.249	0.220	0.029
162	0.293	0.238	0.055	0.294	0.245	0.049	0.282	0.224	0.058
192	0.339	0.282	0.057	0.365	0.290	0.075	0.328	0.265	0.063
196	0.327	0.288	0.039	0.343	0.296	0.047	0.304	0.271	0.033
213	0.339	0.313	0.026	0.355	0.322	0.033	0.318	0.294	0.024
246	0.363	0.362	0.001	0.378	0.371	0.007	0.338	0.340	-0.002
277	0.383	0.407	-0.024	0.374	0.418	-0.044	0.343	0.383	-0.040
335	0.431	0.493	-0.062	0.453	0.506	-0.053	0.404	0.463	-0.059
354	0.401	0.520	-0.119	0.416	0.534	-0.118	0.380	0.489	-0.109
375	0.490	0.551	-0.061	0.494	0.566	-0.072	0.461	0.518	-0.057
407	0.490	0.598	-0.108	0.500	0.614	-0.114	0.455	0.563	-0.108
			RMS=0.059			RMS=0.062			RMS=0.058

Note: Fitted values use the least-squares estimated distance dependence parameter,
1) 1.470 ppm, 2) 1.510 ppm, and 3) 1.382 ppm.

Table 5.9: Double Difference Ionosphere Error, June 21 (24Hr)

	None			**BIM**			**GIM**		
Dist(km)	Est(m)	Fit[1](m)	Res(m)	Est(m)	Fit[2](m)	Res(m)	Est(m)	Fit[3](m)	Res(m)
35	0.047	0.036	0.011	0.040	0.029	0.011	0.031	0.020	0.011
55	0.070	0.058	0.012	0.055	0.045	0.010	0.041	0.032	0.009
68	0.087	0.071	0.016	0.070	0.056	0.014	0.052	0.039	0.013
70	0.080	0.073	0.007	0.064	0.057	0.007	0.048	0.040	0.008
110	0.124	0.115	0.009	0.101	0.090	0.011	0.080	0.063	0.017
119	0.145	0.124	0.021	0.117	0.098	0.019	0.086	0.068	0.018
120	0.140	0.125	0.015	0.113	0.098	0.015	0.076	0.069	0.007
125	0.145	0.131	0.014	0.112	0.103	0.009	0.073	0.071	0.002
134	0.151	0.140	0.011	0.113	0.110	0.003	0.074	0.077	-0.003
145	0.151	0.151	-0.000	0.119	0.119	0.000	0.088	0.083	0.005
159	0.170	0.166	0.004	0.132	0.130	0.002	0.083	0.091	-0.008
162	0.211	0.169	0.042	0.174	0.133	0.041	0.123	0.093	0.030
192	0.198	0.200	-0.002	0.155	0.158	-0.003	0.097	0.110	-0.013
196	0.212	0.205	0.007	0.163	0.161	0.002	0.102	0.112	-0.010
213	0.228	0.222	0.006	0.180	0.175	0.005	0.117	0.122	-0.005
246	0.249	0.257	-0.008	0.192	0.202	-0.010	0.120	0.141	-0.021
277	0.275	0.289	-0.014	0.217	0.227	-0.010	0.167	0.158	0.009
335	0.351	0.350	0.001	0.279	0.275	0.004	0.214	0.191	0.023
354	0.359	0.370	-0.011	0.293	0.291	0.002	0.225	0.202	0.023
375	0.373	0.392	-0.019	0.286	0.308	-0.022	0.179	0.214	-0.035
407	0.403	0.425	-0.022	0.306	0.334	-0.028	0.186	0.232	-0.046
			RMS=0.061			RMS=0.064			RMS=0.061

Note: Fitted values use the least-squares estimated distance dependence parameter,
1) 1.044 ppm, 2) 0.821 ppm, and 3) 0.571 ppm.

ond and third have ionospheric corrections applied using the Broadcast Ionosphere Model (BIM) and the Global Ionosphere Map (GIM), respectively. During the active ionosphere day on April 7, the application of ionospheric models, either the BIM or the GIM, has no significant impact compared to the results with no model being applied. The application of the BIM reduced the ionospheric error by 0.223 ppm (21%) from 1.044 ppm during the quiet day, but degrades slightly by 0.040 ppm (3%) from 1.470 ppm during the active day. The GIM model, however, shows a consistent reduction of errors for both days, i.e. 0.088 ppm (6%) during the active, and 0.473 ppm (45%) during the quiet days.

Modelling the ionospheric error is not a trivial task as can be seen from the active day (Figures 5.5). In general, the ionospheric effect increases linearly with distance and varies with respective to the sun-fixed reference frame. The ionospheric effect has both temporal and spatial variations. These variations can erupt suddenly exceeding an order of magnitude (10x). During active conditions, localized irregularities known as the *travelling ionospheric disturbances* (TIDs) may cause station dependent variations in TEC. A small scale TID is known to last for several minutes covering an area tens of kilometres (Schaer, 1999). This may explain the departure from the linear assumption as shown in Figure 5.6. The attempt here is to model the distance dependence, rather than the more complex station dependence effects. As such, a linear model is used.

Analyses of Active Period - Referring to Figure 5.5, the ionospheric activities fluctuated during the first and last few hours on April 7. Figure 5.8 shows more

details of the active first two hours (00-02Hr). Note that the averaged error RMS of all slant ionospheric delays is at about 0.707 m, or 4.9 ppm over the 145 km. The maximum error, however, had spiked to 16 ppm. Fitting all RMS values over the twenty-one baselines, the ionospheric dispersion is at about 3.7 ppm with or without the corrections being applied. Table 5.10 provides a summary of the ionospheric dispersions of both days.

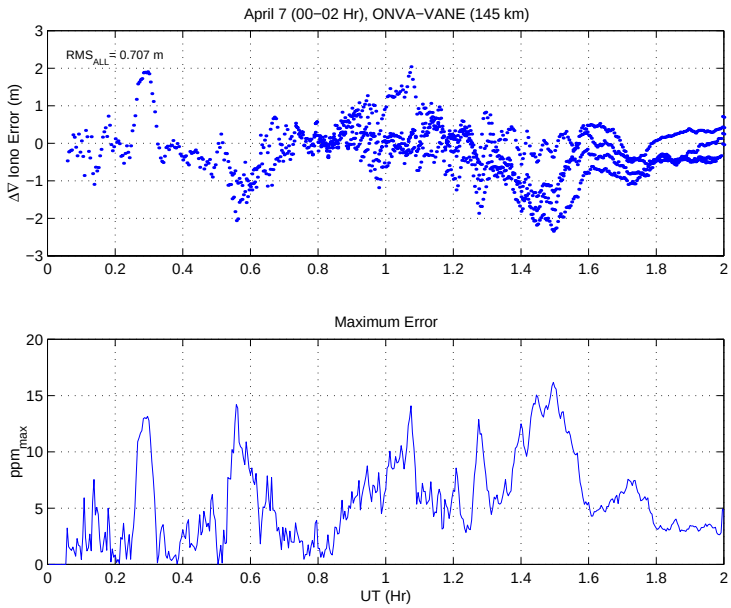

Figure 5.8: Active Ionospheric Error, April 7(00-02Hr)

Table 5.10: Summary of Ionospheric Error

	April 7		June 21
Model	24Hr(ppm)	00-02Hr(ppm)	24Hr(ppm)
NO	1.470	3.736	1.044
BRD	1.510	3.705	0.821
GIM	1.382	3.588	0.571

Ionospheric Delay Distribution - Referring to the histograms shown on Figure 5.9, the uncorrected double difference ionospheric delays, over the 35 km, 196 km, 407 km baselines, are normally distributed centered at zero. And the dispersion grows with distance. Corrected delays either with BIM or GIM produce identical characteristics. These characteristics validate the underlying pseudo-observables model assumptions. Specifically, the pseudo-observables take a value of zero with a distance-dependent dispersion model. The statistical means of double difference ionospheric delays are very close to zero, less than several centimetres in April 7 and less than two centimetres in June 21. Tables 5.11 and 5.12 show the statistical means and standard deviations from both days. For a zero-centred population, both the RMS and the statistical standard deviation are identical.

Table 5.11: Means and Standard Deviations Of Double Difference Ionospheric Delays, April 7 (24Hr)

		No Model		BRD		GIM	
Dist(km)	Sample	Mean(m)	SD(m)	Mean(m)	SD(m)	Mean(m)	SD(m)
35	27242	0.005	0.047	0.004	0.040	0.003	0.031
55	18578	0.003	0.070	0.003	0.055	0.002	0.041
67	22849	0.005	0.087	0.007	0.070	0.008	0.051
68	20487	0.000	0.080	0.002	0.064	0.003	0.048
110	24878	-0.003	0.124	-0.002	0.101	0.000	0.080
119	21906	0.016	0.144	0.016	0.116	0.020	0.084
120	26204	0.006	0.140	0.003	0.113	0.003	0.076
125	19407	0.015	0.144	0.014	0.111	0.009	0.073
134	22326	0.010	0.150	0.010	0.113	0.008	0.073
145	21853	-0.011	0.151	-0.006	0.119	-0.001	0.088
159	21768	-0.019	0.169	-0.012	0.132	-0.006	0.082
162	19136	0.016	0.210	0.017	0.173	0.022	0.121
192	21377	0.017	0.197	0.013	0.154	0.014	0.096
196	20835	0.019	0.211	0.017	0.162	0.019	0.100
213	17219	0.014	0.227	0.017	0.179	0.019	0.116
246	15933	0.005	0.249	0.008	0.191	0.013	0.119
277	22399	-0.004	0.275	-0.003	0.217	0.013	0.167
335	23412	-0.016	0.350	-0.015	0.279	-0.003	0.214
354	20183	-0.022	0.358	-0.022	0.293	-0.003	0.225
375	20250	-0.023	0.373	-0.014	0.284	0.014	0.179
407	19913	-0.024	0.403	-0.008	0.306	0.027	0.184

Table 5.12: Means and Standard Deviations Of Double Difference Ionospheric Delays, June 21 (24Hr)

		No Model		BRD		GIM	
Dist(km)	Sample	Mean(m)	SD(m)	Mean(m)	SD(m)	Mean(m)	SD(m)
35	25555	0.006	0.121	0.002	0.120	0.002	0.117
55	25268	-0.002	0.121	-0.005	0.119	-0.001	0.115
67	25227	0.011	0.144	0.000	0.149	0.011	0.138
68	25249	0.004	0.129	-0.006	0.125	0.000	0.122
110	25452	0.006	0.243	-0.008	0.273	-0.010	0.233
119	26676	0.021	0.268	0.008	0.291	0.011	0.263
120	23896	0.022	0.216	0.010	0.243	0.006	0.201
125	26568	0.006	0.210	-0.008	0.213	0.005	0.197
134	25483	0.009	0.212	-0.019	0.205	0.005	0.199
145	24832	0.022	0.269	-0.008	0.287	0.003	0.249
159	24519	0.023	0.265	0.011	0.323	0.006	0.249
162	22568	0.047	0.289	0.032	0.306	0.029	0.280
192	22198	0.063	0.340	0.048	0.422	0.039	0.326
196	18868	0.061	0.322	0.041	0.341	0.044	0.301
213	23854	0.042	0.336	0.017	0.373	0.020	0.317
246	22120	0.058	0.368	0.020	0.397	0.033	0.345
277	20979	0.051	0.380	0.046	0.413	0.029	0.324
335	21540	0.089	0.422	0.054	0.494	0.048	0.401
354	20696	0.102	0.388	0.065	0.418	0.073	0.373
375	20723	0.074	0.484	0.055	0.493	0.048	0.458
407	20632	0.078	0.484	0.030	0.478	0.052	0.452

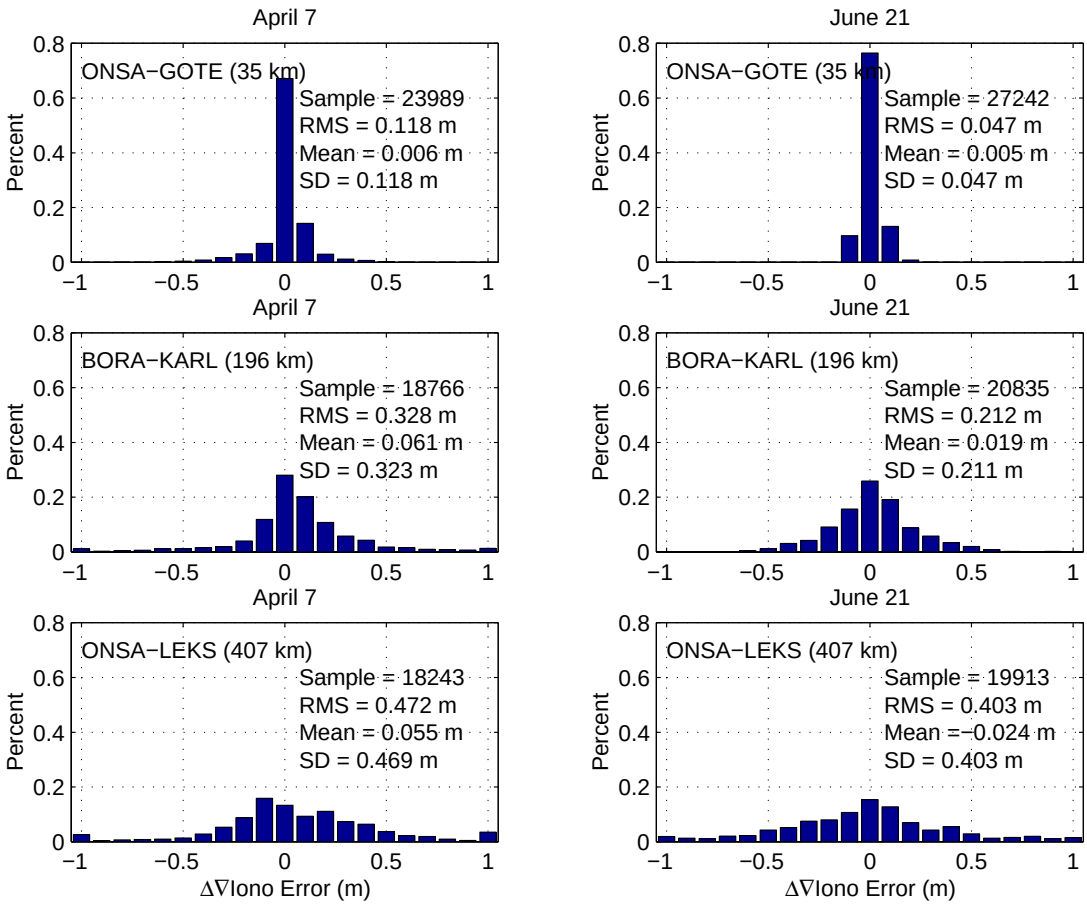

Figure 5.9: Distributions of Double Difference Ionospheric Delay

5.3.3 Ionospheric Time Correlation

The time-correlation parameter, T, is required by the first-order Gauss-Markov process for modelling the ionospheric random process. By definition, the parameter is defined as the time shift when the normalized autocorrelation function decay reaches the $1/e$ point (Gelb, 1996). The autocorrelation functions using identical satellite constellations have been investigated for both days at 1Hz sample rate (Figure 5.10).

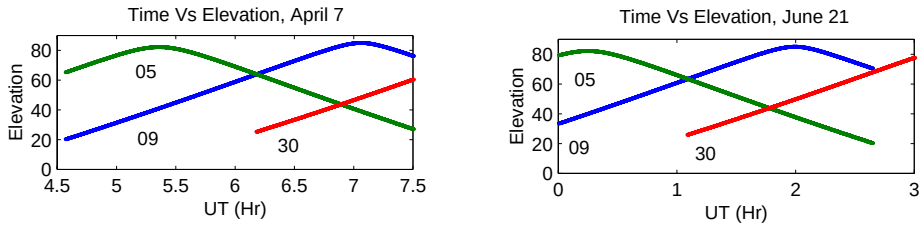

Figure 5.10: Elevations of PRN05, 09, and 30

Further, autocorrelation functions of various baseline lengths have been investigated to determine if there were any consistency over distance. The correlation times computed from the autocorrelation functions over 35 km, 110 km, 196 km, 335 km, and 407 km baseline lengths are tabulated in Table 5.13, and their complete autocorrelation function plots are attached in Appendix B. Interestingly, the degree of decay varies drastically between satellite pairs, as well as the baseline lengths. For example, the correlation times of PRN05-PRN09 and PRN05-PRN30 over the 335 km on April 7, are at 975 seconds and 2300 seconds, respectively (Figure 5.11). Moreover, with the same satellite pair on June 21, PRN05-PRN09, the correlation times vary over the distances, between 660 seconds and 2700 seconds. And there appears no clear distance dependence behaviour, irrespective of baseline length, satellite pairs, or time. In the implementation, a conservative correlation time of 600 seconds is used.

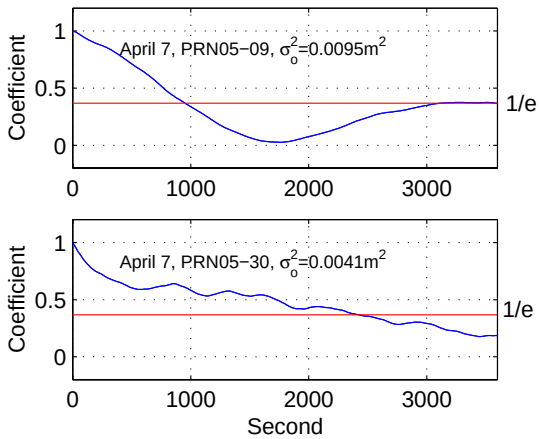

Figure 5.11: Comparison of Ionospheric Autocorrelation between Two Satellite Pairs over JONH-LEKS (335 Km)

Table 5.13: First-Order Correlation Time in Seconds, 1/e Point

Distance	April 7		June 21	
km	PRN05-PRN09	PRN05-PRN30	PRN05-PRN09	PRN05-PRN30
35	675	675	660	600
110	900	750	1680	345
196	1065	1065	3225	510
335	975	2300	3240	1455
407	1170	1605	2700	1260

5.4 Summary

This chapter investigated the stochastic characteristics of a GPS receiver system, specifically, the Ashtech Z-XII with Dorne Margolin chokering antenna, and the distance dependent effects on both days under investigation. The research objective is focused on real-time implementation; therefore, the broadcast orbit and ionospheric corrections (BIM) will be utilized in the performance analyses in the next chapter. The implementation will use the following parameter settings:

- The zenithal measurement errors are - $\sigma_{L1} = \sigma_{L2} = 3$ mm, and $\sigma_{P_r1} = \sigma_{P_r2} =$ 30 cm, combined with the elevation-dependence cosine function model, i.e.:

$$W(z_i^k) = cos^2(z_i^k) \tag{5.7}$$

- Double difference geometrical error - Distance-dependence parameters after applying the Modified Hopfield model with standard meteorological parameters are 0.155 ppm (April 7), and 0.227 ppm (June 21)

- Double difference ionospheric error - Distance-dependence parameters after applying the BIM are 1.510 ppm (April 7), and 0.821 ppm (June 21). These values are used as the scaling bases for ionospheric sensitivity analyses. In separate analyses, a higher 3.705 ppm value is applied to the active period (00-02Hr) in April 7.

- Residual ionospheric time correlation - A conservative correlation time of 600 sec is used.

Chapter 6

Results

The impact of ionospheric pseudo-observables on the performance of integer ambiguity resolution is investigated here using the functional and stochastic models described in the preceding chapters. Three different modes of the ionosphere pseudo-observables - *fixed*, *weighted*, and *floated*[1]- are first compared.

The ionosphere pseudo-observable takes a zero value with a certain dispersion model. The fixed model tightly constrains the pseudo-observables to zero by applying a very small dispersion, i.e. $\sigma_{iono} \rightarrow 0$. This yields the model equivalence of an independent L1/L2 dual-band model. Effectively, it is a short baseline model that completely neglects the ionosphere effects. At the other extreme, the floated model takes an infinite dispersion, i.e. $\sigma_{iono} \rightarrow \infty$. The model yields the model equivalence of an ionosphere-free model, yet preserves the ambiguity integer characteristics, and is well suited for long baselines. The weighted model is a generalization of the two extremes, where the ionospheric dispersion is stochastically tuned in accordance to the baseline length.

In order to evaluate the performance of the ionospheric delay, position, and ambiguity estimates by the various ionospheric weighting schemes, three baselines of

[1]These terms refer to the applied dispersion of the ionospheric pseudo-observables, and should not be confused with the constraining ambiguities.

different lengths are evaluated without constraining the integer ambiguities. The three selected baselines are ONSA-GOTE (36 km), GOTE-VANE (110 km), and BORA-KARL (196 km). The L1 and WL ambiguity resolution performance are investigated later in the chapter.

6.1 Sensitivity of Ionosphere Weighting

The double difference ionospheric delays disperse from the zero mean. The degree of dispersion increases with the baseline length and is related to the ionospheric activities. The dispersion model can be tightly *fixed*, or loosely *floated*, to the pseudo-observables that take a value of zero. This section investigates the impact and the sensitivity of these extreme models, as well as various intermediate weighted models. Three different weighting models have the nominal ionospheric model scaled by factors of one, ten, and twenty.

Plots in Figure 6.1 show the estimate errors of double difference ionospheric delays. The definition of the estimate error implied here is the *observed* minus the *truth*. The observed values are derived from the filter estimates referenced to the L1 frequency. And the truth values are based on the geometry-free (L4) observables constrained to the Bernese V4.0 estimated integer ambiguities and station coordinates. The plots shown are the estimated ionospheric delay errors of two extreme stochastic models over a 110 km baseline during the active day (April 7). The left and the right plots are based on the respective fixed and floated models. The data

points are a composite of 48 independent twenty-minute period runs at 1 Hz rate (i.e. 1200 Epochs). For sake of clarity, only 5% of the data points are plotted. The ionospheric system noise and the measurement noise are set to a small value ($\sim 10^{-6}$ m) for the fixed model, and conversely to a large value ($\sim 10^{6}$ m) for the floated model. Because of the static platform, the positional system noise is set tightly to 0.1 mm, and the ambiguity system noise is also set to a small value ($\sim 10^{-6}$ cycle). If a cycle slip is detected, the filter completely resets. The stochastic dispersion in the left plot is completely clamped to zero. Therefore, each data point is the actual double difference ionospheric delays estimated by the ambiguity-fixed L4 solution. The right plot, however, shows the floated model's estimate errors. The red lines are the averaged RMS values in one-minute intervals.

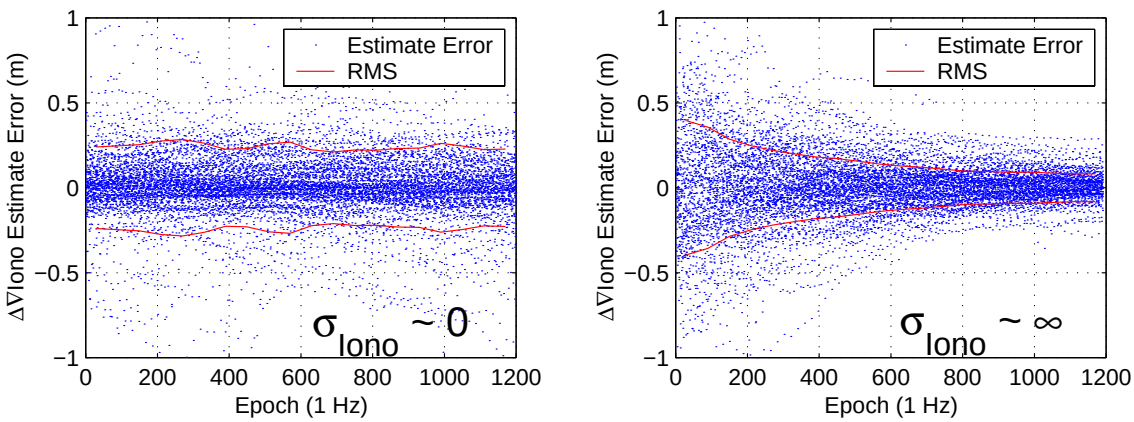

Figure 6.1: Comparative Pseudo-Observable Weightings, GOTE-VANE (110 km), April 7

The RMS values for the fixed model are constant at 25 cm over the entire twenty-minute intervals. The floated model starts with a large RMS of 40 cm and converges

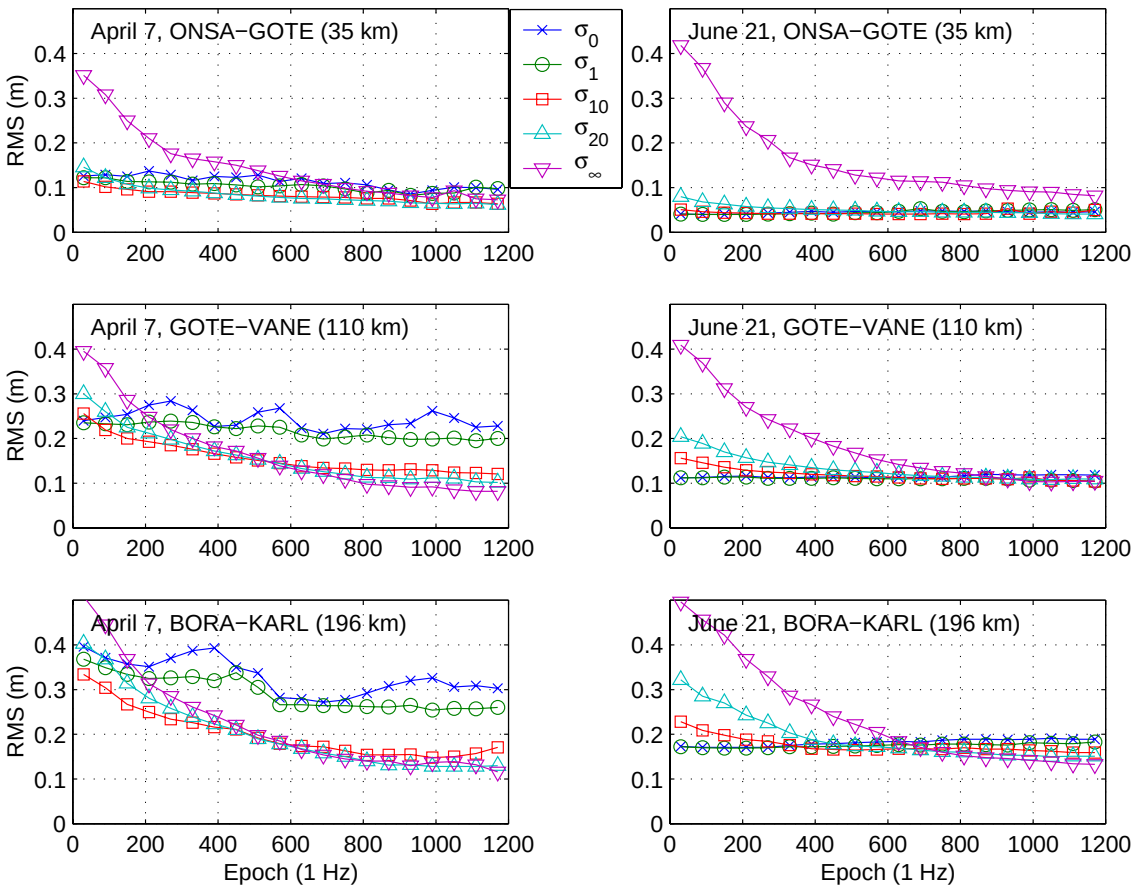

Figure 6.2: Sensitivity of Ionosphere Weighting

to about 8 cm after 20 minutes of filtering. Although the ionospheric system and measurement noise are set to a large number, the apparent convergence of ionosphere estimate error is the result of the tightly constrained positional and ambiguity system noise.

One can see that the floated model reduces the ionospheric estimation error with time at the cost of large errors at the start of the filter. However, the fixed model

starts with smaller RMS, but remains constant during the entire filtering process. One may introduce a stochastically tuned or *weighted* model to compromise between the two extremes. An ideal weighted model would start with a smaller estimate error and have a convergence property.

Two daily averaged network ionospheric models were estimated in the last chapter, i.e. σ_{iono}=1.510 ppm (April 21) and σ_{iono}=0.821 ppm (June 21). These will be applied to the weighted model. In order to gauge the sensitivity of ionospheric models, various scaling factors are applied to the model, i.e. 0 (σ_0), 1 (σ_1), 10 (σ_{10}), 20 (σ_{20}), and infinity (σ_∞[†]). The factor of zero (σ_0) is equivalent to the fixed model. Similarly, the factor of infinity (σ_∞) is equivalent to the floated model. The estimate errors from both days are computed over three selected baseline lengths, i.e. 35 km, 110 km, and 196 km. For conciseness, only the RMS values are plotted in Figure 6.2. The numerical RMS values at the first (Epoch 1 to 60) and the last minute (Epoch 1141 to 1200) are tabulated Table 6.1. The complete error plots for both days are attached in Appendices, C.1 and C.2.

Referring to Table 6.1, the floated model (σ_∞) outperforms the weighted models ($\sigma_1, \sigma_{10}, \sigma_{20}$) and the fixed model ($\sigma_0$), if given ample time for the estimate error to converge. The floated model, however, exhibits a larger estimate error at the start of filtering. Such a characteristic is not well suited for fast ambiguity resolution. The fixed model performed better at the shorter baseline length of 35 km under the ionospherically quiet condition in June 21. Of the three weighted models, the σ_1

[†]The notation refers to scaling of the nominal ionospheric model, i.e. $\sigma_n = n \cdot \sigma_{iono}$

Table 6.1: Ionospheric Estimate Errors at the Start and the End of Filtering

	35 km		110 km		196 km	
April 7	Start†	End‡	Start	End	Start	End
Factor[a]	m(%[c])	m(%)	m(%)	m(%)	m(%)	m(%)
σ_0	0.126	0.096	0.240	0.228	0.396	0.303
σ_1	0.122(-3)	0.098(2)	0.235(-2)	0.200(-12)	0.368(-7)	0.260(-14)
σ_{10}	0.114(-10)	0.064(-33)	0.256(7)	0.121(-47)	0.334(-16)	0.171(-43)
σ_{20}	0.146(16)	0.062(-35)	0.300(25)	0.102(-55)	0.403(2)	0.130(-57)
σ_∞	0.351(178)	0.073(-24)	0.395(64)	0.082(-64)	0.508(28)	0.116(-62)
	35 km		110 km		196 km	
June 21	Start	End	Start	End	Start	End
Factor[a]	m(%[c])	m(%)	m(%)	m(%)	m(%)	m(%)
σ_0	0.041	0.046	0.112	0.118	0.173	0.189
σ_1	0.041(0)	0.051(11)	0.112(0)	0.105(-11)	0.172(-1)	0.183(-3)
σ_{10}	0.051(24)	0.050(9)	0.156(39)	0.104(-12)	0.228(32)	0.159(-16)
σ_{20}	0.080(95)	0.041(-11)	0.204(82)	0.109(-8)	0.322(86)	0.151(-20)
σ_∞	0.418(919)	0.082(78)	0.409(265)	0.105(-11)	0.496(187)	0.133(-30)

a - based on a BIM corrected nominal ionospheric model, i.e. σ=1.510 ppm, $\sigma_n = n \cdot \sigma$,
b - based on a BIM corrected nominal ionospheric model, i.e. σ=0.821 ppm, $\sigma_n = n \cdot \sigma$,
c - estimation error changes in percentage with respect to the fix model (σ_0),
a negative % indicates a reduction in error estimate.
† - averaged RMS from the first minute, Epoch 1 through 60, and
‡ - averaged RMS from the last minute, Epoch 1140 through 1200.

model is nearly identical to the fixed model and appears too restrictive in the dispersion model. Though the comparisons between σ_{10} and σ_{20} are somewhat mixed, depending on baseline length and the ionospheric conditions, σ_{10} appears to have a smaller error at the start of filtering.

Active Period Analyses - the ionospheric condition was extremely active during the first few hours of April 7. The ionospheric model based on the average of all ionospheric range delays over the first two hours is estimated at 3.705 ppm versus the day's average model of 1.510 ppm. This section investigates the sensitivity of the ionospheric estimates using a model that is more representative of the condition.

Figure 6.3 provides a comparative performance between two models over the active period (00-02Hr, April 7). The average of first minute filtered estimate error and the average of last minute (20th minute) estimate errors are tabulated in Table 6.2. It appears that the ionospheric delay estimates are rather insensitive to the dispersion settings. The unit scale factor (σ_1) again appears to be too restrictive and performs nearly equivalent to that in the fixed model. The scale factor range between 10 and 20 yields about the same result after a few minutes of filtering. However, a larger scale factor would have a larger estimation error at the start of the filter.

Table 6.2: 24 Hr Model Versus 3 Hr Model

	35 km		110 km		196 km	
00-02Hr	Start	End	Start	End	Start	End
Factor[a]	m(%[c])	m(%)	m(%)	m(%)	m(%)	m(%)
σ_0	0.065	0.068	0.144	0.119	0.305	0.222
σ_1	0.063(-3%[c])	0.040(-41%)	0.193(34%)	0.122(-3%)	0.332(9%)	0.141(-36%)
σ_{10}	0.135(107%)	0.048(-29%)	0.419(190%)	0.055(-54%)	0.517(70%)	0.065(-71%)
σ_{20}	0.279(329%)	0.055(-19%)	0.594(313%)	0.058(-51%)	0.526(72%)	0.067(-69%)
σ_∞	0.495(661%)	0.059(-13%)	0.756(425%)	0.059(-53%)	0.636(109%)	0.068(-69%)
	35 km		110 km		196 km	
00-02Hr	Start	End	Start	End	Start	End
Factor[b]	m(%[c])	m(%)	m(%)	m(%)	m(%)	m(%)
σ_0	0.065	0.068	0.144	0.125	0.305	0.222
σ_1	0.061(-6%)	0.044(-35%)	0.155(8%)	0.168(34%)	0.266(-13%)	0.211(-5%)
σ_{10}	0.099(52%)	0.027(-60%)	0.181(26%)	0.107(-14%)	0.298(-2%)	0.059(-73%)
σ_{20}	0.139(113%)	0.045(-33%)	0.390(171%)	0.055(-56%)	0.517(70%)	0.064(-71%)
σ_∞	0.495(661%)	0.059(-13%)	0.756(425%)	0.059(-53%)	0.636(109%)	0.068(-69%)

a - based on BIM corrected nominal ionospheric model computed from 00-02Hr, σ=3.750 ppm, $\sigma_n = n \cdot \sigma$
b - based on BIM corrected nominal ionospheric model computed from the entire day, σ=1.510 ppm, $\sigma_n = n \cdot \sigma$
c - estimation error changes in percentage with respect to the fix model (σ_0),
a negative % indicates a reduction in error estimate.

From the sensitivity analyses, the ionospheric weighted model appears insensitive to the nominal ionospheric models (σ_1), and a scale factor of 10 appears reasonable.

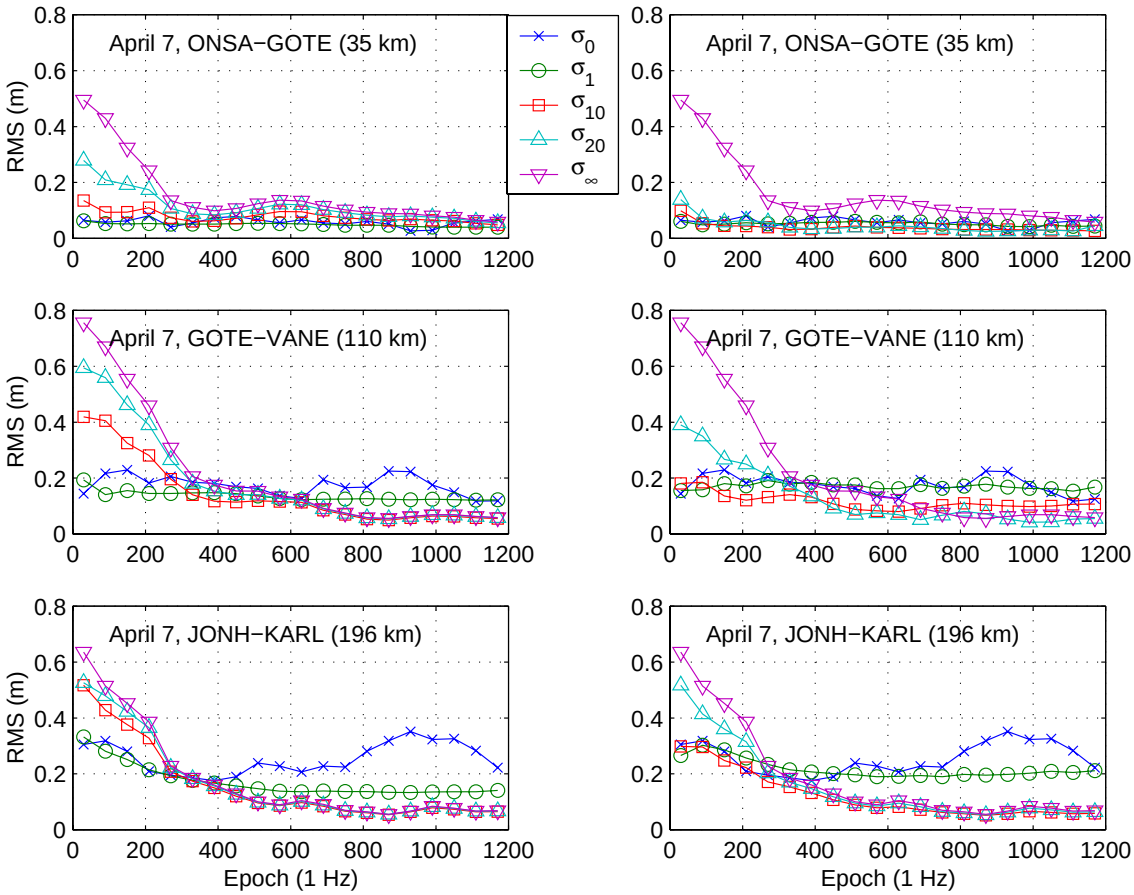

Figure 6.3: Comparative Performance Between 2 Hr and 24 Hr Ionospheric Models, April 7

The ionospheric model derived from one day's solution is acceptable, because of the apparent trade-off in the magnitude of the ionospheric weighting. A tighter dispersion setting will have smaller initial estimation errors, but the estimation error will not converge. Conversely, a looser dispersion setting will have a larger initial estimation error, but the estimate errors will decrease with time. If one does not require a fast ambiguity resolution requirement, the floated model (σ_∞) may be suitable. The

fixed model is only suitable for shorter baselines under a few tens of kilometres and under ionospherically quiet conditions.

A factor of ten will be applied to the daily nominal ionospheric dispersion model in all subsequent analyses.

6.2 Unconstrained Ambiguity Solution

The estimates are subtracted from the Bernese V4.0 solution that define the *estimate errors*, which are illustrated at 90-Percentile for both April 7 and June 21. Figures 6.4 and 6.5 represent the horizontal and the vertical components, and Figures 6.6 and 6.7 represent the WL and L1 ambiguity estimate errors.

Each baseline is processed every 30 minutes over 24 hours, with each run lasting 20 minutes. Each bin represents one minute elapsed from the initialization. Certain characteristics can be derived from the histograms. It is evident that the ionosphere fixed estimates is rather unstable especially during the active ionosphere day. This is the direct result of the functional model incorrectly ignoring the ionospheric effect. However, the initial estimate errors are typically smaller than the float estimate errors. In contrast, the floated estimate errors are stable and converge over time. However, the ionosphere float estimate errors are consistently higher in the first several minutes than the fixed errors before tapering. This is due to the infinite variance assigned to the ionosphere, and they rapidly converge through filtering.

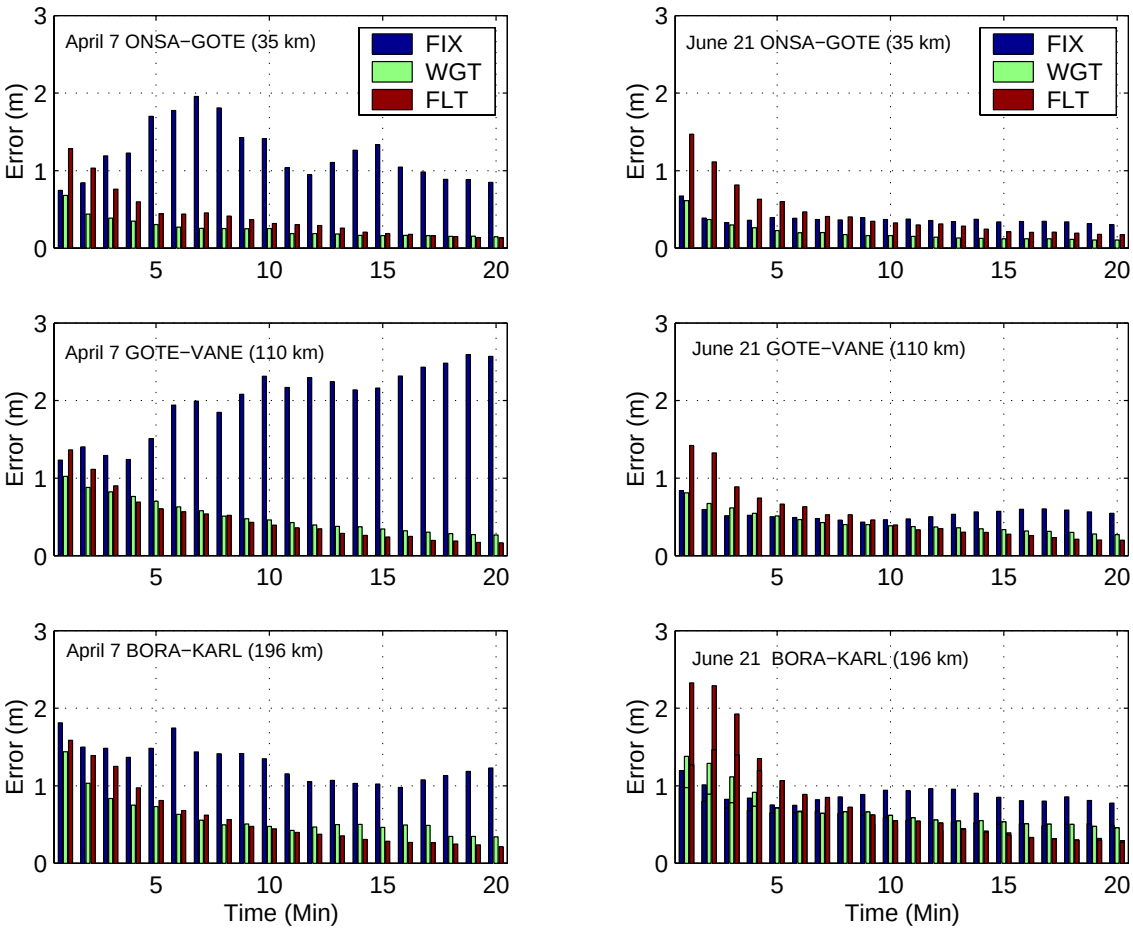

Figure 6.4: Horizontal Accuracy at 90-Percentile

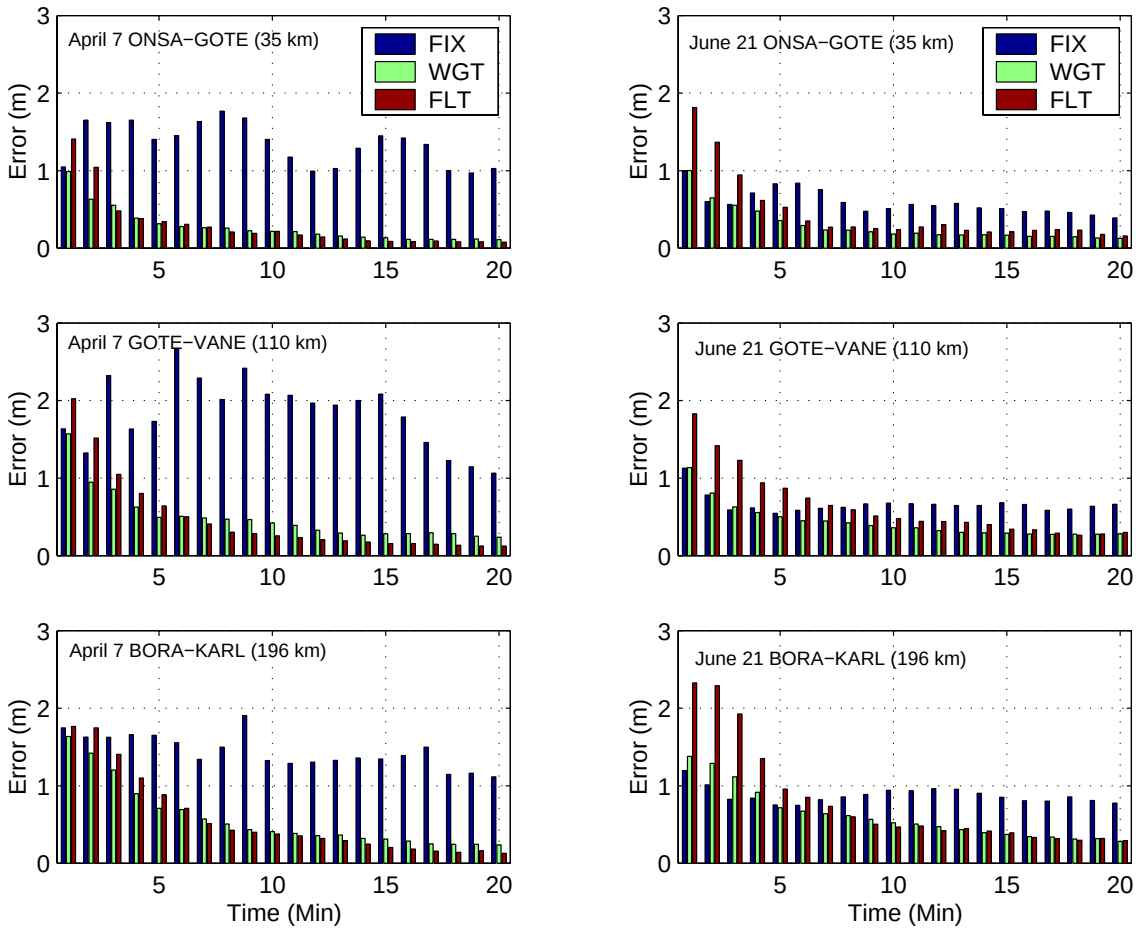

Figure 6.5: Vertical Accuracy at 90-Percentile

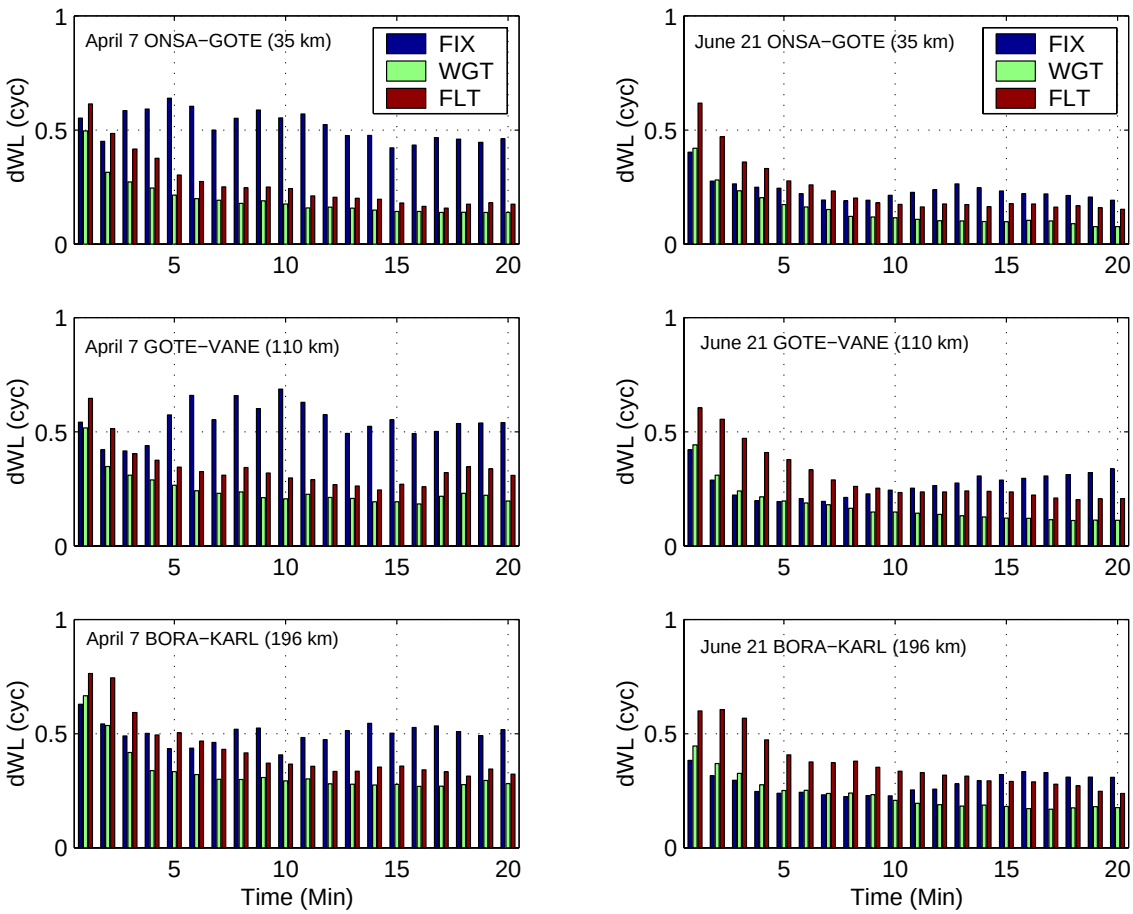

Figure 6.6: Unconstrained N_{WL} Ambiguity Accuracy at 90-Percentile

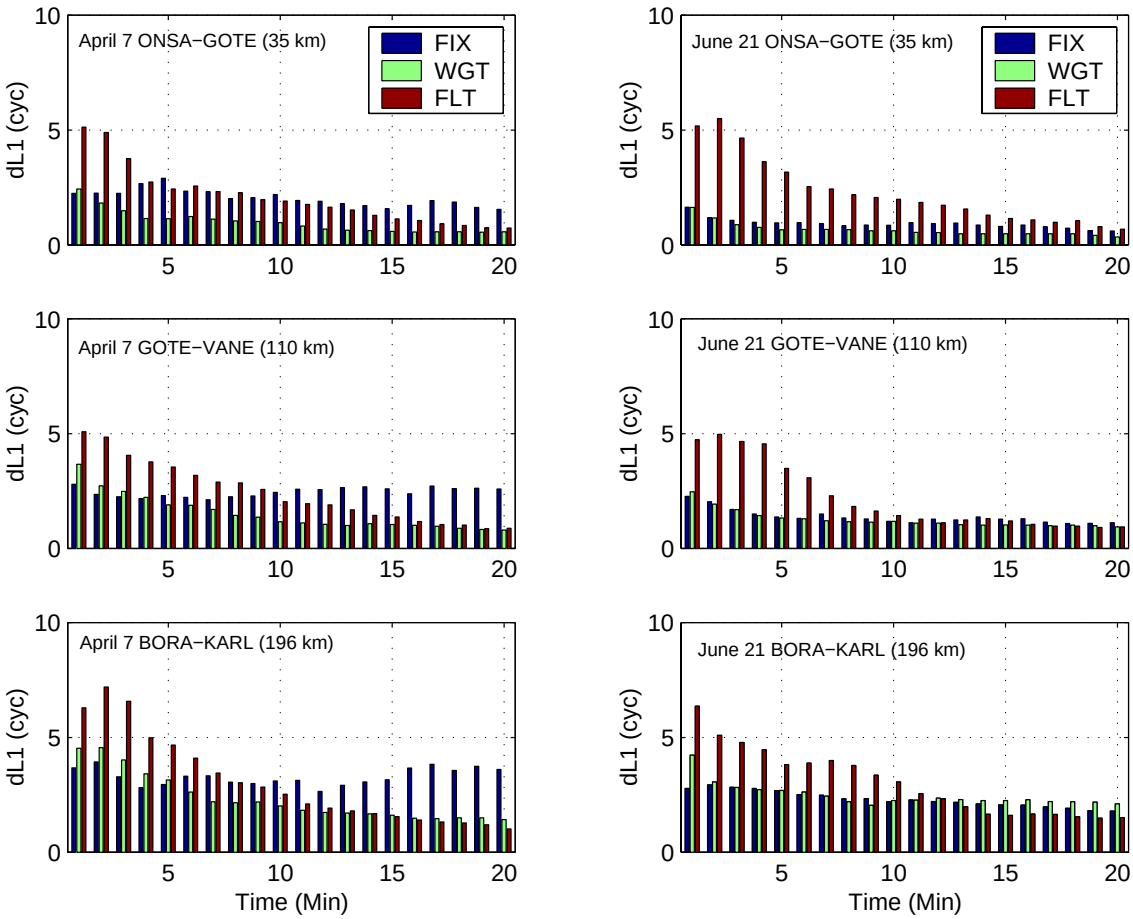

Figure 6.7: Unconstrained N_{L1} Ambiguity Accuracy at 90-Percentile

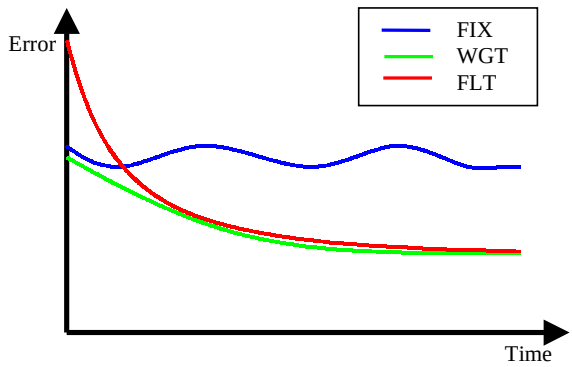

Figure 6.8: Characteristics of Ionosphere Fixed, Weighted, and Floated Pseudo-Observables

The ionosphere weighted scheme possesses the positive characteristics of both the fixed and the weighted schemes and appears optimal, at least with these baselines over 36 km. Specifically, the instantaneous estimate errors are small, compared with the fixed estimate errors, and have the convergence property that the accuracy improves with time. These characteristics are illustrated in Figure 6.8.

Table 6.3: Summary of Estimate Errors At 90-Percentile †

	April 7				June 21			
Distance (km)	*Horz* (m)	*Vert* (m)	N_{L1} (cyc)	N_{WL} (cyc)	*Horz* (m)	*Vert* (m)	N_{L1} (cyc)	N_{WL} (cyc)
35	0.148	0.112	0.565	0.139	0.107	0.127	0.341	0.077
110	0.266	0.237	0.801	0.197	0.272	0.282	0.944	0.112
196	0.342	0.237	1.421	0.281	0.458	0.281	2.109	0.176
335	0.466	0.235	1.816	0.359	0.689	0.382	2.171	0.240
407	0.356	0.227	1.902	0.435	0.671	0.557	2.862	0.192

† After filtered for 20 minutes without constraining the ambiguities.

Table 6.3 shows the position and ambiguity error estimates at 90-precentiles af-

ter 20 minutes of filtering without constraining the ambiguities. The error estimates from both days, April 7 and June 21, show a clear distance-dependent error growth. For the ionospherically less active day on June 21, however, the error appears larger than in the more active day in April. The residual double difference tropospheric effect is greater on June 21, which may be the cause of worsen results. There may be other unknown factors, because the troposphere effects are only 5 cm (0.136 ppm, Table 5.4) and 10 cm (0.226 ppm, Table 5.3) at 407 km for the respective days. One important fact that can be derived from Table 6.3 is that the widelane ambiguity, N_{WL}, estimate errors are consistently smaller than 0.5 cycle even at 407 km. Integer N_{WL} resolution is the topic of the next section.

6.3 Widelane Ambiguity Resolution Performance

The weighted ionosphere method generally gives the least error estimates over the entire 20 minutes of filtering and is more optimal than the fixed or the floated schemes, as demonstrated in the last section. This section now looks into the integer ambiguity validation tests. The two schemes, *ADOP* and the *ratio* tests, are compared by resolving the double difference integer N_{WL} ambiguities over 20 baselines, whose lengths varies between 35 km and 402 km, for both April 7 (Figure 6.9) and June 24 (Figure 6.10). Each data point plotted in the table represents an average of 48 independent 20-minute runs.

The tolerance criteria are set to 0.1 for ADOP and 3.0 for the ratio tests. These

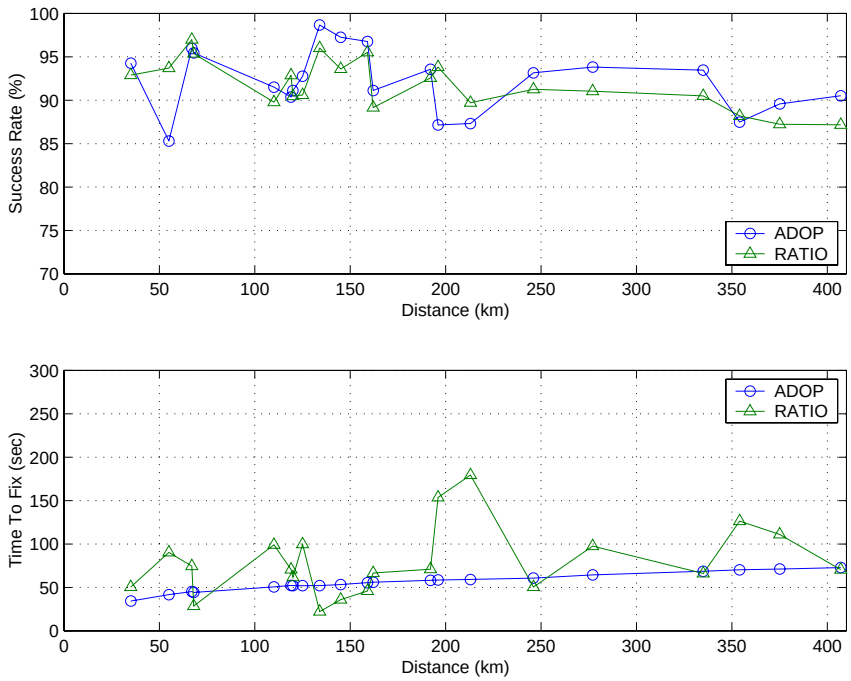

Figure 6.9: Widelane Ambiguity Resolution Performance, April 7

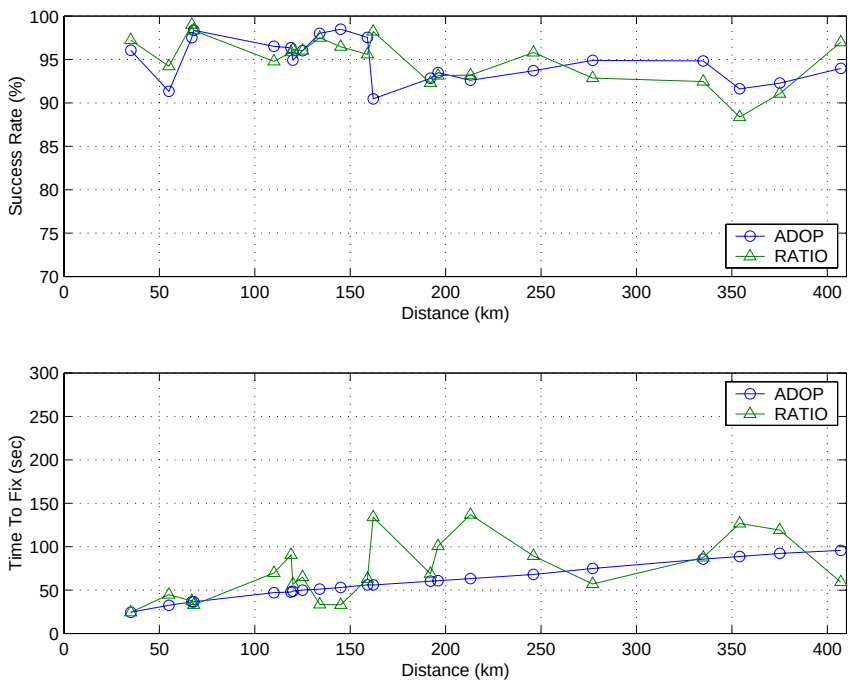

Figure 6.10: Widelane Ambiguity Resolution Performance, June 21

settings appear reasonable after a few test runs. In terms of reliability, both tests are comparable. However, the time-to-fix performance is quite different. The time-to-fix for the ADOP test increases with distance. This is a direct result of the distance dependent stochastic modelling of the measurements. In contrast, the performance of the ratio test varies drastically, from an average of 30 seconds to 3 minutes. It is well known that GPS measurements are often subjected to unpredictable sudden degradations, such as multipath and atmospheric effects. The filter implemented in the analysis herein does not have the adaptive capability, and the prior system and measurement error models may not be accurate, leading to an unreliable ADOP value. Therefore, the ratio test is preferred over the ADOP test in this analysis.

The success rates in resolving the integer widelane, N_{WL}, ambiguity over baseline lengths up to 402 km are consistently at about 90% and 95% for April 7 and June 21, respectively. And the time-to-fix is typically under 2 minutes. Such high rates of success are consistent with the unconstrained estimates that the errors are well below 0.5 cycle as shown in previous section.

6.3.1 Widelane Constrained Position and L1 Ambiguity Estimates

Once the integer widelane ambiguities are successfully resolved, they are constrained by the parameter removal (Equations 4.55 and 4.56). The impact of the integer widelane, N_{WL}, constraint on position and N_{L1} estimates is now investigated.

In Table 6.4 are the N_{WL} fixed error estimates after 20 minutes of filtering at 90-

percentiles over 48 independent process runs. Typically the N_{WL}'s are resolved and constrained within the first two minutes. The effect of the N_{WL} constraint appears to be most effective for baselines greater than 196 km, where the estimate errors are reduced by up to 59% for both position and ambiguity components, compared to the unconstrained estimates. Shorter baselines, less than 196 km, in contrast, tend to increase the error estimates. The aberration may be a result of an incorrect ambiguity (co)variance matrix entered into the parameter removal process. The resolved N_{WL} are removed and the precision of the remaining unknown parameters are enhanced by virtue of their (co)variance data.

One can conclude that, based on the algorithms implemented, the N_{WL} constraint N_{L1} error estimates are greater than 0.5 cycle over 20 minute data sample sets, even at 35 km at 90-precentile, making the N_{L1} integer resolution problematic.

Table 6.4: Summary of Error Estimates At 90-Percentile With Constrained N_{WL} †

	April 7				June 21			
Distance (km)	*Horz* (m)	*Vert* (m)	N_{L1} (cyc)	N_{WL} (cyc)	*Horz* (m)	*Vert* (m)	N_{L1} (cyc)	N_{WL} (cyc)
35	0.188	0.121	0.561	-	0.122	0.074	0.570	-
110	0.161	0.207	0.933	-	0.277	0.171	1.207	-
196	0.140	0.132	1.079	-	0.432	0.239	2.120	-
335	0.227	0.164	1.225	-	0.315	0.225	1.031	-
407	0.260	0.190	1.604	-	0.469	0.259	2.490	-
	Improvement over Unconstrained N_{WL} (%)							
35	-27	-8	1	100	-14	41	-67	100
110	39	13	-16	100	-2	39	-28	100
196	59	44	24	100	6	15	-1	100
335	51	30	33	100	54	41	53	100
407	27	16	16	100	30	54	13	100

† After filtered for 20 minutes, based on independent 48 runs over a 24-hour data set.

6.4 L1 Integer Ambiguity Resolution Performance

This section attempts to evaluate the performance of resolving the integer N_{L1} ambiguities. The ambiguity validation tests used here are a combination of both ADOP and ratio tests. The ADOP test is included to provide an adequate time for the unknown parameters to filter and avoid erroneous ambiguity fixes.

Fig 6.11 and 6.12 illustrate the performance for both days. The success rates are poor, with less than 30%, for all baselines between 35 km and 407 km on April 7. A somewhat better performance is detected for the less ionospherically active day on June 21, with a success rate of 70% at 35 km and a rapid decay with distance to 20% at 150 km.

6.5 Ionosphere-Free Solution

The integer N_{WL} ambiguities can be resolved without much difficulty. In contrast, resolving the integer N_{L1} is much more problematic for baselines over tens of kilometres. Assuming both integer N_{L1} and N_{WL} ambiguities were resolved successfully, the integer N_{L2} ambiguity can be directly derived from the arithmetical relationship (Equation 2.40). The integer constrained ionosphere-free (L3) solution (Equation 2.20) can be formed to eliminate the first-order ionosphere effect. This section investigates the comparative positional accuracy between the ionosphere-weighted and ionosphere-free solutions.

In the ionosphere-weighted scheme, the N_{WL} integers are first constrained, then

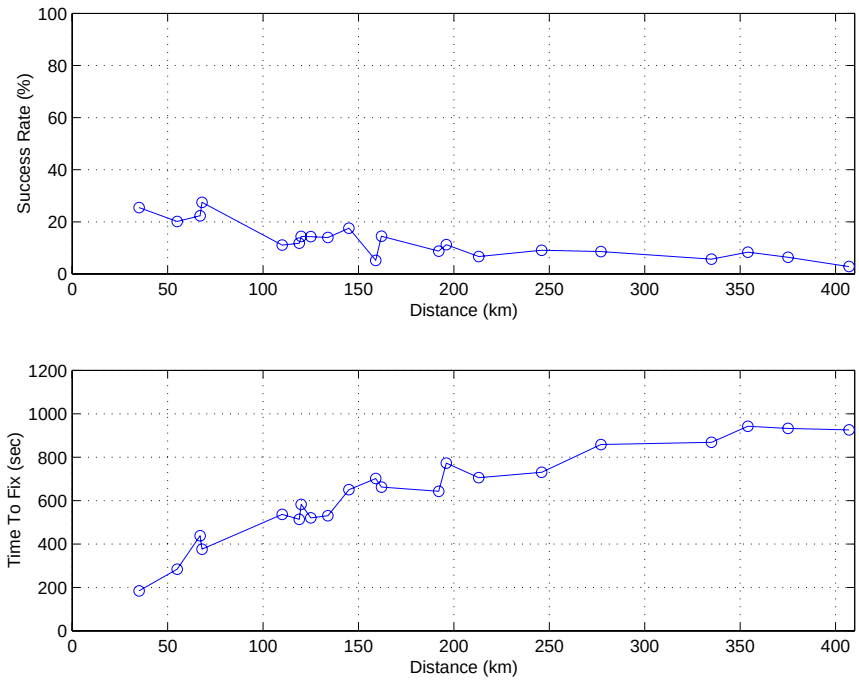

Figure 6.11: L1 Ambiguity Resolution Performance, April 7

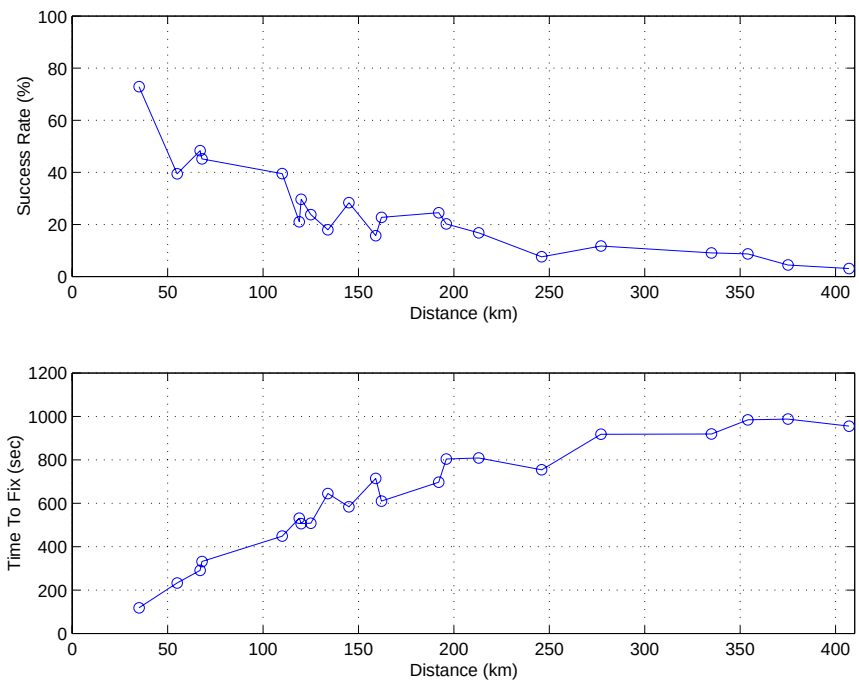

Figure 6.12: L1 Ambiguity Resolution Performance, June 21

followed by the N_{N1} integers. The unknown positions, along with the ionosphere states, are sequentially filtered epochwise. A slight modification was made to the algorithm to accommodate the ionosphere-free solution. Once the N_{WL} and N_{L1} are resolved, the N_{L2} integers are derived to form the integer fixed L3 linear combination observables. It is then treated as an ultra-precise code range replacing the P1 in the measurement vector. The remaining observation types are de-weighted and the ionosphere vectors are tightly constrained to zero.

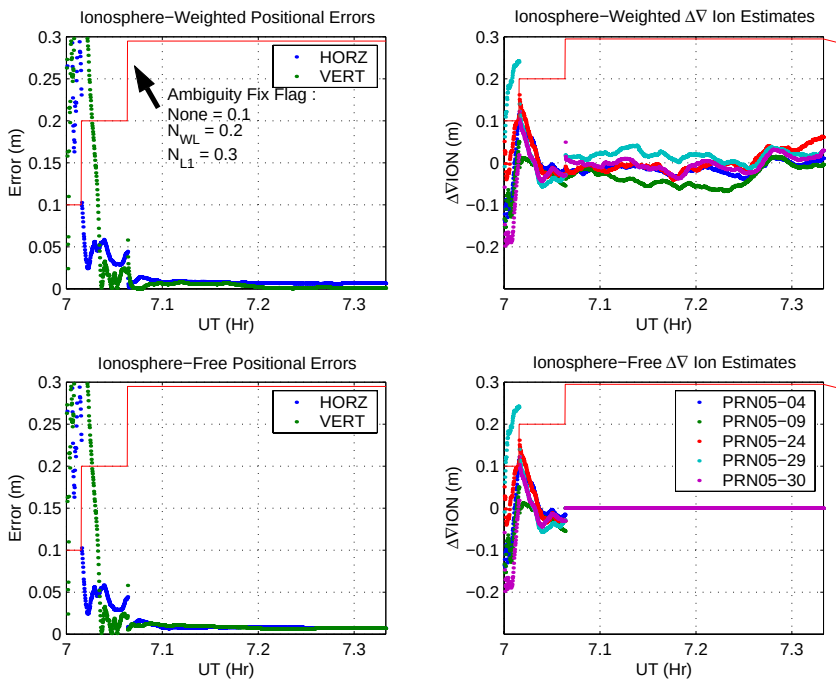

Figure 6.13: Comparative Positional Accuracy Between Integer Ambiguity Constrained Ionosphere-Weighted and Ionosphere-Free Solutions (Static Mode)

Figure 6.13 illustrates the comparative performance in the positional domain over a single run starting at 07:00 UT on April 7, 2001 on a 68 km baseline between ONSA

and BORA. The solid red lines indicate the integer fixing conditions, i.e. 0.1 for no ambiguity fixing, 0.2 for N_{WL} fixing, and 0.3 for N_{L1} fixing. The positional system noise is tightly set to simulate a static platform. The top row plots are derived from the ionosphere-weighted solution, and the bottom plots are from the ionosphere-free solution. Note that the double differenced ionosphere estimates in the ionosphere-weighted solution are not constrained to zero, resulting in a bandwidth of 50 cm ionospheric compensation to the positional estimates. Unlike the ionosphere-free counterpart, the ionosphere estimates are constrained to zero and the ionosphere effect is removed by the ionosphere-free linear combination. Interestingly, both approaches yield a very similar performance. The ionosphere-weighted approach yields the horizontal and vertical RMS estimate error of 8 mm and 5 mm after filtering for 20 minutes. The ionosphere-free solution yields a RMS value of 9 mm for both the horizontal and the vertical components.

To better assess the comparative performance, the positional system noise levels are infinitely increased. By doing so, the previous positional estimates are not carried forward, simulating a dynamic platform. Figure 6.14 shows an increase in the positional estimate error noise levels. The horizontal and vertical RMS noise levels are at 11 mm and 11 mm for the ionosphere-weighted solution. The increased noise levels of the ionosphere-free solution are nearly equivalent at 11 mm and 10 mm.

The tightly constrained ionosphere-fixed and loosely constrained ionosphere-floated solutions are also compared (Figure 6.15). Infinite positional noise levels are again applied. The plots shown on the top and bottom rows reflect the respective tightly

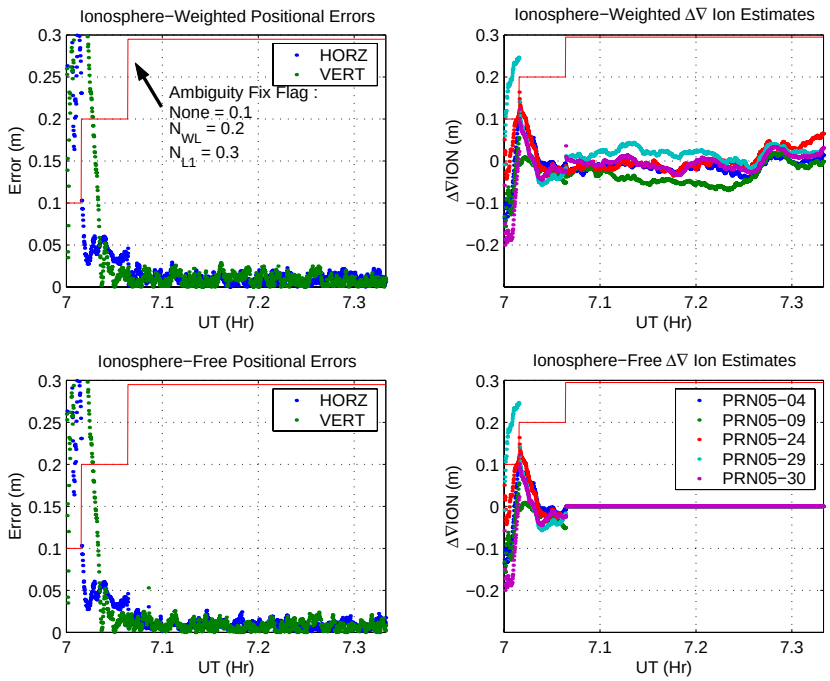

Figure 6.14: Comparative Positional Accuracy Between Integer Ambiguity Constrained Ionosphere-Weighted and Ionosphere-Free Solutions (Dynamic Mode)

and loosely constrained ionosphere pseudo-observables to a zero constant.

The successful instantaneous N_{WL} and N_{L1} resolution by the ionosphere-fixed solution shown in the plot are purely coincidental. In fact, neglecting the ionosphere effect by fixing the ionosphere effect to zero is quite problematic in resolving the N_{L1} integer ambiguity. This can be seen by the rather unstable nature of the positional estimates that deviate as much as 10 cm.

Large positional errors shown in the bottom left plot is a direct consequence of fixing ambiguities to a wrong set of integers, reflecting the difficulties in resolving

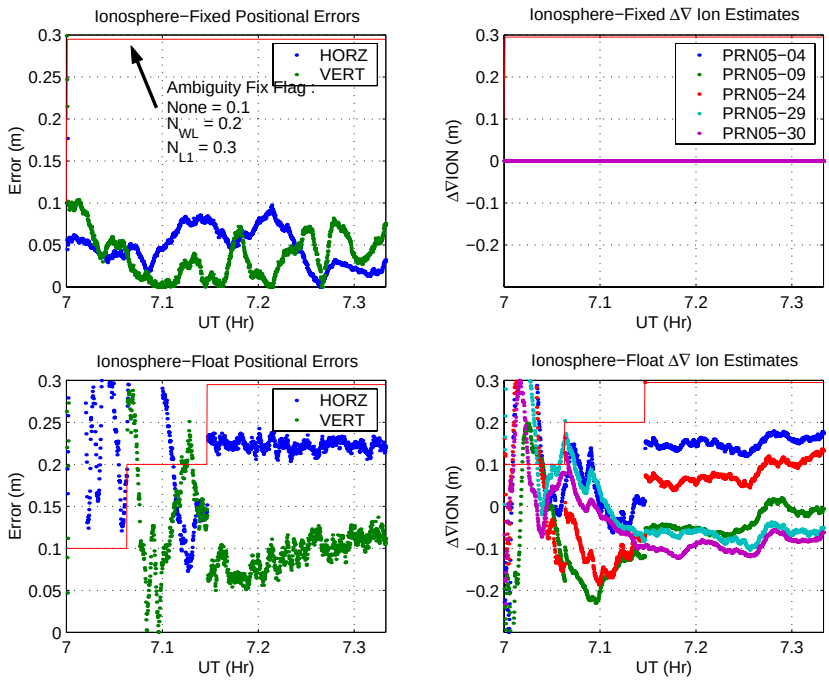

Figure 6.15: Comparative Positional Accuracy Between Integer Ambiguity Constrained Ionosphere-Fixed and Ionosphere-Floated Solutions (Dynamic Mode)

the integer N_{L1} ambiguities with infinitely weighted ionosphere pseudo-observables.

6.6 Summary

Three ionospheric weighting schemes - fixed, weighted, and floated - were compared over various baseline lengths. Their unconstrained ambiguity filtered solutions converged with time, except for the fixed scheme on an ionospherically active day. The floated model yielded higher initial estimate errors, but converged rapidly. The weighted scheme provided smaller initial estimate errors and also converged. Three

facts can be deduced from above. First, the filter algorithm implemented herein is valid. Second, neglecting the ionosphere effect by tightly fixing the ionospheric delay to zero can lead to a sub-optimal filter. And third, the stochastically tuned or weighted scheme gave the optimal filtering performance, particularly for applications requiring fast ambiguity resolution capabilities.

Incorporating the LAMBDA method to the filtered solutions, the widelane ambiguities were successfully resolved at better than 90-percentile for all baselines, even at 407 km. The required time-to-fix was generally less than 2 minutes. Subsequent attempt to resolve the L1 ambiguities proved to be problematic. The success rates were about 25% for April 7 and 45% for June 21, for baselines up to 68 km. The required time-to-fix were about 7 minutes.

The standard approach to eliminate the first-order ionosphere effect by forming the ionosphere-free (L3) linear combination observables can also be accomplished by introducing properly weighted ionosphere pseudo-observables.

Chapter 7

Conclusions and Recommendations

7.1 Conclusions

This thesis investigated an alternative approach to mitigate the ionospheric effects on GPS measurements by including a stochastically tuned ionosphere pseudo-observable into the functional model.

Precise positioning is hampered by the inability to resolve and constrain the integer ambiguities caused by the ionospheric delay and other error sources. The traditional approach to mitigate the ionospheric effect had been to linearly combine the dual-band L1/L2 measurements and form an ionosphere-free (L3) observable. Through combination, the integer characteristic of ambiguity is lost and cannot be constrained to improve the estimated precision. Often the integer characteristics of L1 ($\lambda_{L1} \approx 19$ cm) and L2 ($\lambda_{L2} \approx 24$ cm) are recovered by combining the integer widelane (WL, $\lambda_{WL} \approx 86$ cm) and narrowlane (NL, $\lambda_{NL} \approx 11$ cm) ambiguities. The wider wavelength of WL could be resolved more successfully. However, the narrower wavelength of NL is much more problematic, and the ambiguity resolution by this approach is only possible through long, static observation. The alternative approach, introduced here, preserves the full wavelength of L1 and takes advantage of the 86 cm widelane ambiguity.

Three schemes of ionosphere stochastic weightings were compared. The dispersion of pseudo-observable can be tightly *fixed* (i.e. constrained to zero) yielding the model equivalence of an independent L1/L2 dual-band model. At the other extreme, an infinite *floated* weight gives the equivalence of an ionosphere-free model. A stochastically tuned, or *weighted*, model provides a compromise between the two extremes. The weighted model yields smaller error estimates for the first few minutes, comparable to the characteristics found in the fixed model, and the error reduces over time through filtering, similar to the characteristics found in the floated model. Therefore, the weighted scheme appears to be the optimal choice.

Once both L1 and WL integer ambiguities are found, these can be constrained to form a precise ionosphere-free (L3) observation. It was shown that the independent L1 and L2 observables together with weighted ionospheric pseudo-observables have the same effect as the integer constrained L3 observable. Their estimate errors are equivalent.

A fast (<2 minutes) successful (>90%) widelane, N_{WL}, ambiguities resolution for baselines over 400 km was consistently achieved with the inclusion of ionosphere pseudo-observables. Upon constraining the 86 cm N_{WL}, other unknown parameter precision improved for long baselines over several tens of kilometers. However, the level of improvement is not adequate to resolve the more challenging 19 cm N_{L1} integer ambiguities, even after filtering for 20 minutes.

This research has demonstrated that the successful widelane ambiguity resolution

is possible, even during adverse ionospheric conditions. Further research is warranted to resolve the L1 ambiguity.

7.2 Recommendations

The following is a list of recommendations for subsequent research:

- Stochastic Modelling - The presence of time-correlation is detected in GPS measurements, as a result of reconstructing the L2 measurements under the A/S condition, and can be eliminated either by state augmentation or orthogonalization (Salzmann, 1993).

- Adaptive Filtering - GPS measurements are subjected to sudden unexpected degradations. A reliable ambiguity resolution requires accurate real ambiguity estimates and their realistic (co)variance matrix. This necessitates an automatic real-time adaptation yielding an optimal Kalman filter.

- Partial Ambiguity Fixing - The integer ambiguity search algorithms implemented are based on an epoch-wise binary decision over a complete set of ambiguities. If the corresponding (co)variance information can be accurately modelled, certain ambiguities with higher confidence levels could be partially constrained to enhance unresolved ambiguity resolution in the subsequent epochs.

- Ionosphere Model - In addition to the GIM and BIM, other ionosphere models are available. The ionosphere delay consists of two components, the deterministic and stochastic. These can be easily incorporated into the algorithm. With

a more accurate ionospheric model, the L1 ambiguity resolution performance may be improved.

- External Measurement Corrections - GPS measurements can be enhanced by applying a covariance function derived from a network of multiple reference stations. The initial results using FLYKIN has shown an improved WL ambiguity resolution success rate of 70% at 242 km from 45% without corrections (Raquet, 1998). The algorithm implemented here yields a consistent success rate of 90% or better for baselines up to 402 km without any external corrections. The L1 ambiguity resolution performance may improve by applying the corrections.

- External Meteorological Input - The tropospheric delay model based on a standard set of meteorological parameters may not be adequate to resolve the L1 ambiguities. A better delay model could be sought.

References

Ashjaee, J. and Lorenz, R. (1992). "Precise GPS Surveying After Y-Code". In *Proceedings of the 5th International Technical Meeting of the Satellite Division of the Institute of Navigation (ION GPS-92)*, pages 657-659. Albuquerque, New Mexico.

Bauersima, I. (1993). "NAVSTAR/Global Positioning System(GPS), Mitteilungen der Satelliten Beobachtungsstation Zimmerwald", No.10, II. Astronomical Institute, University of Berne.

Berg, H. (1948). "Algemeine Meteorologie". Dümmler's Verlag, Bonn.

Bevis, M., Businger, T., Herring, T.A., Rocken, C., Anthes, R.A., and Ware, R.H. (1992). "GPS Meteorology: Remote Sensing of Atmospheric Water Vapor using the Global Positioning System". *Journal of Geophysical Research*, Vol.97, No.15, pages 787-801.

Blais, J.A.R. (1998). "Estimation and Spectral Analysis". University of Calgary Press. Calgary, Alberta.

Blewitt, G. (1989). "Carrier Phase Ambiguity Resolution for the Global Positioning System Applied to Geodetic Baselines up to 2000Km". *Journal Geophysical Research*, Vol.94, No.B8, pages 10187-10203.

Blewitt, G. (1998). "Chapter 6: GPS Data Processing Methodology" in *GPS for Geodesy*, Teunissen, P.J.G., Kleusberg, A. (Editors). Springer, Berlin.

Bock, T., Gourevitch, S., Counselman, C.C., King, R.W., and Abbot, R.I. (1986). "Interferometric Analysis of GPS Phase Observations", *Manuscripta Geodaetica*, Vol.11, pages 282-288.

Brown, R.G. and Hwang, P.Y.C. (1997) "Introduction to Random Signals and Applied Kalman Filtering". John Wiley and Sons, New York.

Brunner, F.K. and Gu, M. (1991) "An Improved Model for the Dual Frequency Ionospheric Correction of GPS Observatons", *Manuscripta Geodaetica*, Vol.16, pages 205-214.

Brunner, F.K. and Welsch, W.M. (1993) "Effect of the Troposphere on GPS Measurements", *GPS World*, Vol.4, No.1, pages 42-51.

Businger, S., Chiswell, S.R., Bevis, M., Duan, J., Anthes, R.A., Rocken, C., Ware, R.H., Exner, M., Van Hove, T., and Solheim, F.S. (1996). "The Promise of GPS in Atmospheric Monitoring". *Bulletin of the American Meteorological Society*, Vol.77, No.1.

Chen, D. (1994). "Development of a Fast Ambiguity Search Filtering Method for GPS Carrier Phase Ambiguity Resolution". PhD Thesis, UCGE Report No.20071,

Department of Geomatics Engineering, The University of Calgary

Councelman, C.C. and Gourevitch, S.A. (1981). "Miniture Interferometer Terminals for Earth Surveying: Ambiguity and Multipath with the Global Positioning System". Reprint from the *IEEE Transactions on Geoscience and Remote Sensing*, Vol.GE-19, No.4

Darin, F., Johansson, J., Carlsson, R., Elgered, G., Jarlemark, P., and Ronnang, B. (1997). "Continuous Monitoring of the Atmosphere Using GPS". In *Proceedings of the 10th International Technical Meeting of the Satellite Division of the Institute of Navigation (ION GPS-97)*, pages 199-205. Kansas City, Missouri

de Jong, P. and Tiberius, C. (1996). "The LAMBDA Method fo Integer Ambiguity Estimation: Implementation Aspects". Delft Geodetic Computing Centre, Delft University of Technology, Faculty of Geodetic Engineering.

Department of Defence (2001). Global Positioning System Standard Positioning Service Performance Standard. Office of the Assistance Secretary of Defence for Command, Control, Communications, and Intelligence. Washington, DC.

Duan, J., Bevis, M., Fang, P., Bock, Y., Chiswell, S.R., Businger, S., Rocken, C., Solheim, F., Van Hove, T., Ware, R.H., McClusky, S., Herring, T.A., and King, R.W. (1996). "GPS Meteorology: Direct Estimation of the Absolute Value of Precipitable Water", *Journal of Applied Meteorology*, Vol.35, No.6

Fortes, L.P.S., Cannon, M.E., Ryan, S., Marceau, G., Wee, S., and Raquet, J. (2000a). "Use of a Multi-Reference GPS Stations Network for Precise 3D Positioning in the St.Lawrenece Seaway". *International Hydrographic Review*, Vol.1-1.

Fortes, L.P.S., Cannon, M.E., and Lachapelle, G. (2000b). "Testing a Multi-Reference GPS Station Network for OTF Positioning in Brazil", *In Proceedings of the 13th International Technical Meeting of the Satellite Division of the Institute of Navigation (ION GPS-00)*. Salt Lake City, Utah.

Gao, Y., Heroux, P., Kouba, J. (1994). "Estimation of GPS Receiver and Satellite L1/L2 Signal Delay Biases Using Data From CACS". In *Proceedings of the International Symposium on Kinematic Systems in Geodesy, Geomatics and Navigation (KIS94)*, pages 109-117. Banff, Alberta.

Gelb, A. (Editor) (1996). "Applied Optimal Estimation", 4th Printing. The MIT Press. Cambridge, Massachusetts

Goad, C.C. and Goodman, L. (1974) "A Modified Tropospheric Refraction Correction Model". Presented at the *American Geophysical Union Annual Fall Meeting*, San Francisco, California.

Goad, C.C. and Yang, M. (1994). "On Automatic Precision Airborne GPS Positioning". In *Proceedings of the International Symposium on Kinematic Systems in*

Geodesy, Geomatics and Navigation (KIS94), pages 131-138. Banff, Alberta.

Gurtner, W. and Mader, G. (1990). "Receiver Independent Exchange Format Version 2", *CSTG GPS Bulletin*, Vol.3, No.3. National Geodetic Survey. Rockville, Maryland.

Hatch, R. (1990). "Instantaneous Ambiguity Resolution, Kinematic Systems in Geodesy, Surveying, and Remote Sensing". *International Association of Geodesy Symposia 107*. Springer-Verlag, New York.

Hoffmann-Wellenhof, B., Lichtenegger, H., and Collins, J. (1992). "GPS: Theory and Practice, 3rd Edition". Springer-Verlag, New York.

Komjathy, A. and Langley, R.B. (1996). "An Assessment of Predicted and Measured Ionospheric Total Electron Content Using a Regional GPS Network". In *Proceedings of the National Technical Meeting of the Institute of Navigation*. Santa Monica, California

Klobachar, J.A. (1996), "Chapter 12: Ionospheric Effects of GPS" in *Global Positioning System: Theory and Applications, Vol.1*, 4th Printing, Parkinson, B., and Spilker, J. (Editors), The American Institute of Aeronautics and Astronautics, Inc.

Kunysz, W. (1996). "A Novel GPS Survey Antenna". NovAtel Inc. Calgary, Alberta.

Lachapelle, G., Cannon, M.E., and Lu, G. (1992). "High Precision GPS Navigation with Emphasis on Carrier Phase Ambiguity Resolution". *Marine Geodesy*, 14(4). pages 253-269.

Lachapelle, G., Alves, P., Fortes, L.P., and Cannon, M.E. (2000) "DGPS RTK Positioning Using a Reference Network". In *Proceedings of the 13th International Technical Meeting of the Satellite Division of the Institute of Navigation (ION GPS-00)*, pages 1165-1171. Salt Lake City, Utah.

Landau, H., Euler, H-J. (1992). "On-the-Fly Ambiguity Resolution for Precise Differential Positioning". In *Proceedings of the 5th International Technical Meeting of the Satellite Division of the Institute of Navigation (ION GPS-92).* Albuquerque, New Mexico.

Langley, R.B. (1991). "The GPS Receiver:An Introduction". *GPS World*, Vol.4, No.4, pages 50-53.

Langley, R.B. (1998a). "Chapter 3: Propagation of the GPS Signal" in *GPS for Geodesy*, Teunissen, P.J.G., Kleusberg, A.(Editors). Springer-Verlag, Berlin.

Langley, R.B. (1998b). "Chapter 4: GPS Receivers and the Observables" in *GPS for Geodesy.* Teunissen, P.J.G. and Kleusberg, A.(Editors). Springer-Verlag, Berlin.

Langley, R.B., (2000). "GPS, the Ionosphere, and the Solar Maximum", *GPS World.*

pages 44-49. July

Leick, A. (1990). *GPS Satellite Surveying*, John Wiley and Sons, New York.

Lu, G. (1995). "Develeopment of a GPS Multi-Antenna System for Attitude Determination". PhD Thesis, UCGE Report No.20073, Department of Geomatics Engineering, The University of Calgary.

Mervart, L. (1995). "Ambiguity Resolution Techniques in Geodetic and Geodynamic Applications of the Global Positioning System". *Geodätisch-geophysikalische Arbeiten in der Schweiz*, Bd.53. Zurich, Switzerland.

Mannucci, A.J., Wilson, B.D., and Edwards, C.D. (1993). "A New Method for Monitoring the Earth's Ionospheric Total Electron Contect Using the GPS Global Network". In *Proceedings to the 6th International Technical Meeting of the Satellite Division of the Institute of Navigation (ION GPS-93)*, pages 1223-1323. Salt Lake City, Utah

NASA (2001) National Aeronautics and Space Administration, Marshall Space Flight Center, http://science.msfc.nasa.gov.

NOAA (2001). National Oceanic and Atmospheric Administration, Space Environment Office, http://www.sec.noaa.gov.

Odijk, D. (1999). "Stochastic Modelling of the Ionosphere for Fast GPS Ambiguity Resolution". *In Geodesy Beyond 2000, The Challenges of the First Decade*. IAG General Assembly, Vol. 121. Birmingham, U.K.

Raquet, J., Lachapelle,G., and Melgård,T.E. (1998). "Test of a 400Km x 600Km Network of Reference Receivers for Precise Kinematic Carrier-Phase Positioning in Norway". In *Proceedings of the 11th International Technical Meeting of the Satellite Division of The Institute of Navigation (ION GPS-98)*, pages 407-416. Nashville, Tennessee.

Raquet, J. (1998). "Development of a Method for Kinematic GPS Carrier-Phase Ambiguity Resolution Using Multiple Reference Receivers". PhD Thesis, UCGE Report No.20116, Department of Geomatics Engineering, The University of Calgary.

Rothacher, M. and Mervart, L. (Editors) (1996), "Bernese GPS Software V4.0". Astronomical Institute University of Berne.

Rothacher, T., Springer, T.A., Schaer, S., and Beutler, G. (1998). "Processing Strategies for Regional GPS Network". *International Association of Geodesy Symposia*, Vol.118, Brunner, F.K. (Editor). Springer-Verlag, Berlin, Heidelberg.

Saastamoinen, J. (1973). "Contribution to the Theory of Atmospheric Refraction". *Bulletin Geodésiqué*, 107, pages 13-34.

Salzmann, M. (1993). "Least-Squares Filtering and Testing for Geodetic Navigation Applications". Netherlands Geodetic Commission. Delft, The Netherlands.

Sandhoo, K., Turner, D., and Shaw, M. (2000). "Modernization of the Global Positioning System". In *Proceedings of the 13th International Technical Meeting of the Satellite Division of the Institute of Navigation (ION GPS-00)*, pages 2175-2183. Salt Lake City, Utah.

Schaer, S. (1997). "How to use CODE's Global Ionosphere Maps". Astronomical Institute, University of Berne.

Schaer, S. (1999). "Mapping and Prediciting the Earth's Ionosphere Using the Global Positioning System". *Geoätisch-geophysikalische Arbeiten in der Schweiz*, Bd.59. Zurich, Switzerland.

Schwarz, K.P. (1987). "Kalman Filtering and Optimal Smoothing". In *Papers for the CISM Adjustment And Analysis Seminar*. Krawkiwsky, E. (Editor). The Canadian Institute of Surveying and Mapping. Ottawa, Ontario.

Skone, S. (1998). "Wide Area Ionosphere Grid Modelling in the Auroral Region". PhD thesis, UCGE Report No.20123, Department of Geomatics Engineering, The University of Calgary.

Spilker, J., (1996), "Chapter 3: GPS Signal Structure and Theoretical Performance".

In *Global Positioning System: Theory and Applications, Vol.1*, 4th Printing, Parkinson, B., and Spilker, J. (Editors), The American Institute of Aeronautics and Astronautics, Inc.

Strang, G. and Borre, K. (1997). "Linear Algebra Geodesy, and GPS", Wellesley-Cambridge Press. Wellesley, Massachusetts.

SWEPOS (2001). National Land Survey of Sweden, http://swepos.lmv.lm.se

Teunissen,P.J.G. (1993). "Least-Squares Estimation of the Integer GPS Ambiguity". General Meeting of the International Association of Geodesy. Beijing, China.

Teunissen, P.J.G. (1995). "The Least-Squares Ambiguity Decorrelation Adjustment: A Method for Fast GPS Integer Ambiguity Estimation". *Journal of Geodesy*, (70)1-2, pages 65-82

Teunissen, P.J.G. and Odijk, D. (1997). "Ambiguity Dilution of Precision: Definition, Properties, and Application". In *Proceedings of 10th International Technical Meeting of the Satellite Division of the Institute of Navigation (ION GPS-97)*, pages 891-899. Kanasas City, Missouri.

Teunissen, P.J.G. (1999). "An Optimality Property of the Integer Least-squares Estimator". *Journal of Geodesy*, 73, pages 587-593

Teunissen, P.J.G. (2001). Personal Communication, June.

Tiberius, C. (1999). "The GPS Data Weight Matrix: What Are the Issues ?", In *Proceedings of the National Technical Meeting of the Institute of Navigation*. San Diego, California.

Tiberius, C. and Kenselaar, F. (2000). "Estimation of the Stochastic Model for GPS Code and Phase Observables". *Survey Review*, 35(277), pages 152-159.

Tiberius, C., Jonkman, N., and Kenselaar, F. (1999). "The Stochastics of GPS Observables". *GPS World*, 10(2), pages 49-54.

Tiberius, C. (1998). "Recursive Data Processing for Kinematic GPS Surveying". Netherlands Geodetic Commission, Publication No.45. Delft, The Netherlands.

Tralli, D.M. and Lichten, S.M. (1990). "Stochastic Estimation of Tropospheric Path Delays in Global Positioning System". *Bulletin Geodésiqué*, 64, pages 127-159.

Van Dierendonck, A.J., Fenton, P., and Ford, T. (1992). "Theory and Performance of Narrow Correlator Technology in GPS Receiver". *Navigation: Journal of the Institute of Navigation*, Vol.39, No.3, pages 265-283.

Van Dierendonck, A.J. (1994). "Understanding GPS Receiver Terminology: A Tutorial on What Those Words Mean". In *Proceedings of the International Symposium*

on Kinematic Systems in Geodesy, Geomatics and Navigation (KIS94), pages 15-24. Banff, Alberta.

Van Dierendonck, A.J. (1996), "Chapter 8: GPS Receivers" in *Global Positioning System: Theory and Applications, Vol.1*, 4th Printing, Parkinson, B., and Spilker, J. (Editors), The American Institute of Aeronautics and Astronautics, Inc.

Wilson, B.D. and Mannucci, A.J. (1993). "Instrumental Biases in Ionospheric Measurements Derived from GPS Data". In *Proceedings of the 6th International Technical Meeting of the Satellite Division of the Institute of Navigation (ION GPS-93)*. Salt Lake City, Utah.

White House Press Release (2000), Washington, DC.

Appendix A

Double Difference Zero-Baseline Measurement Noise

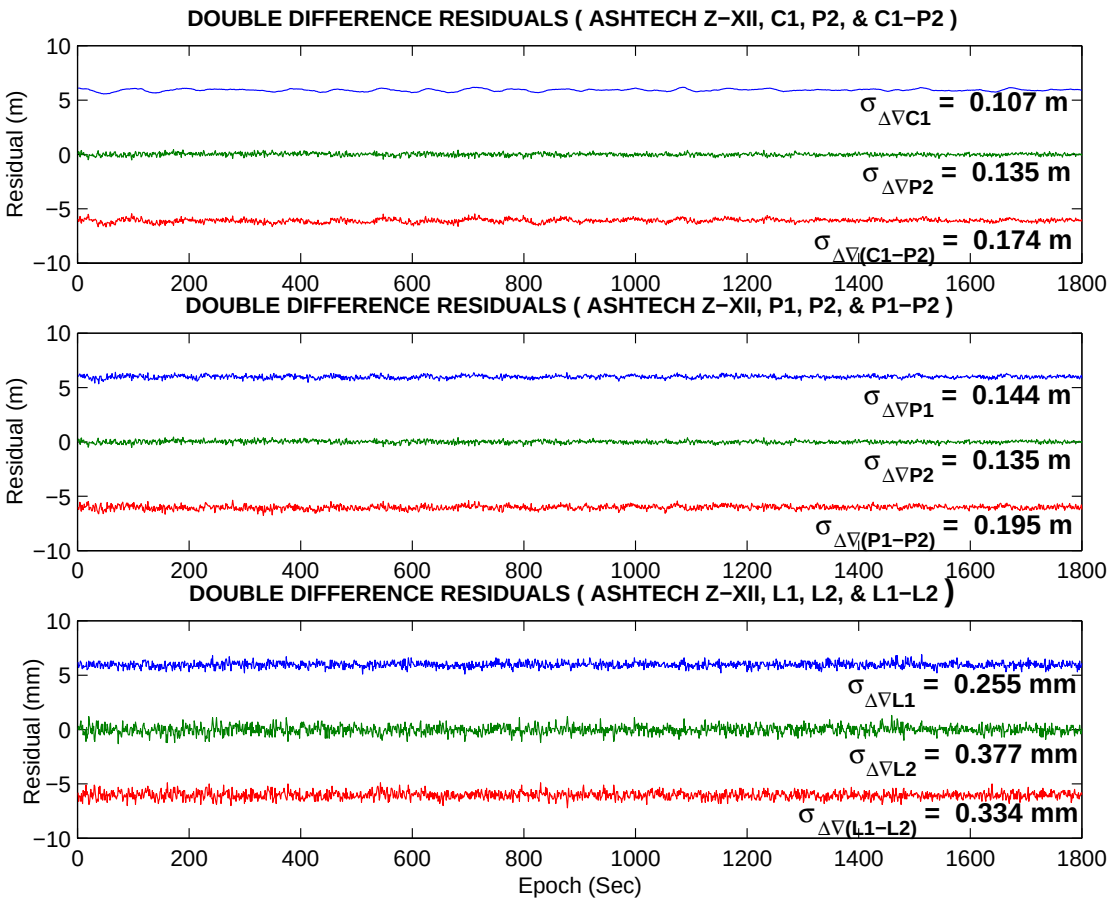

Figure A.1: Double Difference Measurement Noise Between PRN 11 and PRN 20 ($> 70°$ versus $> 40°$) Over Zero Baseline

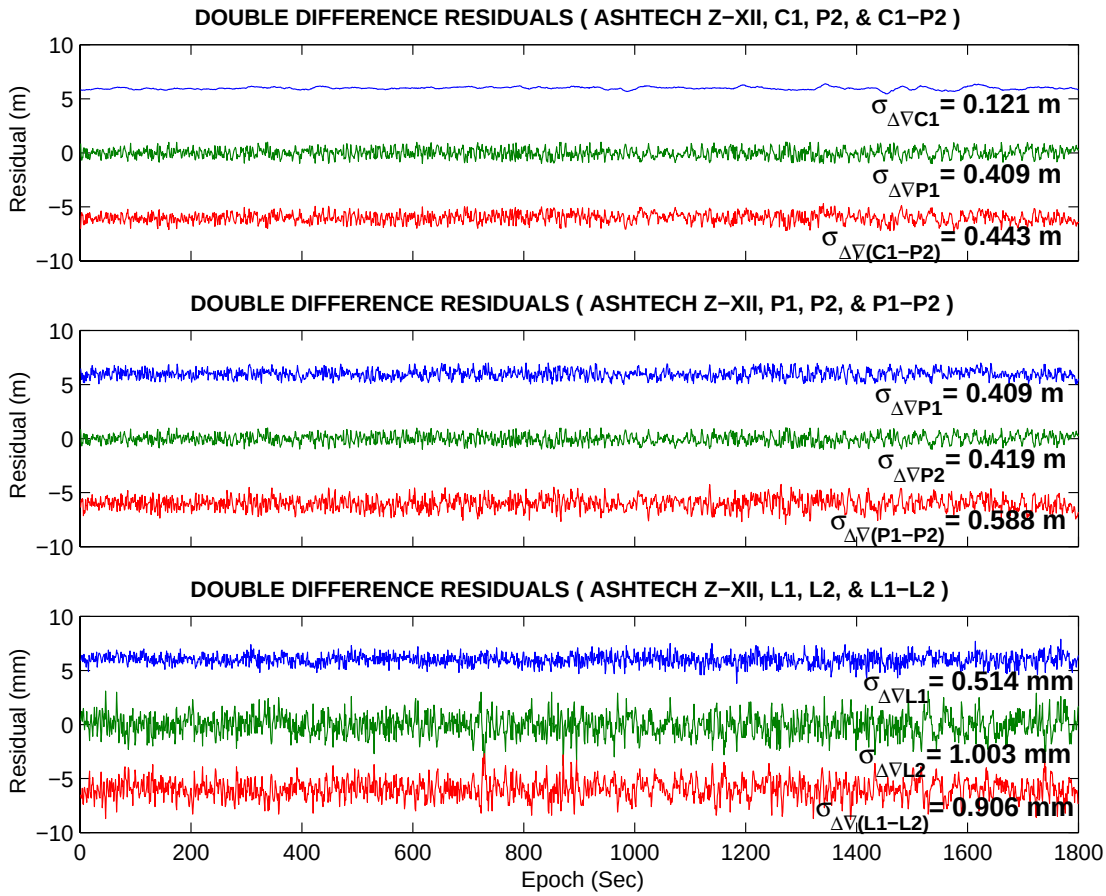

Figure A.2: Double Difference Measurement Noise Between PRN 11 and PRN 21 ($> 70°$ versus $15° \sim 25°$) Over Zero Baseline

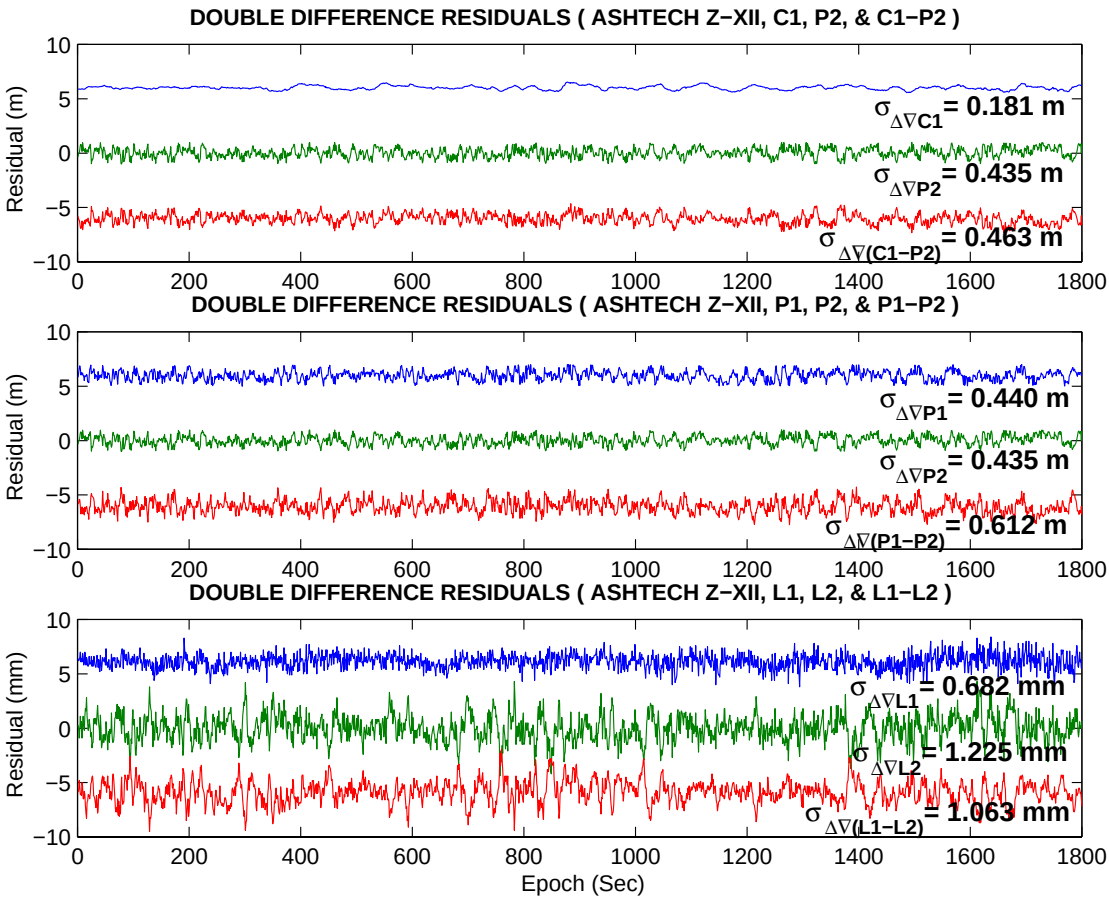

Figure A.3: Double Difference Measurement Noise Between PRN 11 and PRN 02 ($> 70°$ versus $7° \sim 15°$) Over Zero Baseline

Appendix B

Autocorrelation Functions of Double Difference Ionosphere

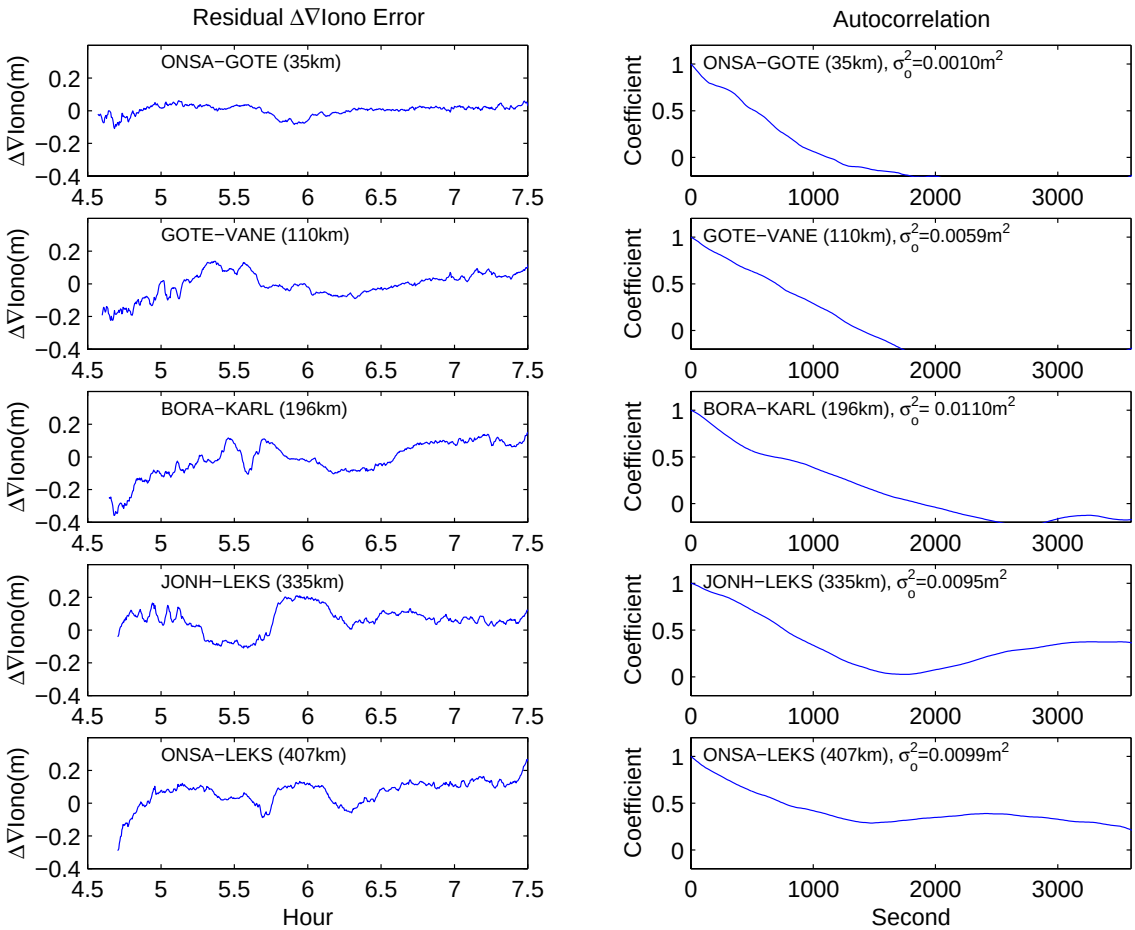

Figure B.1: Autocorrelation of Residual Double Difference Ionospheric Delay Between PRN05 and PRN09, April 7

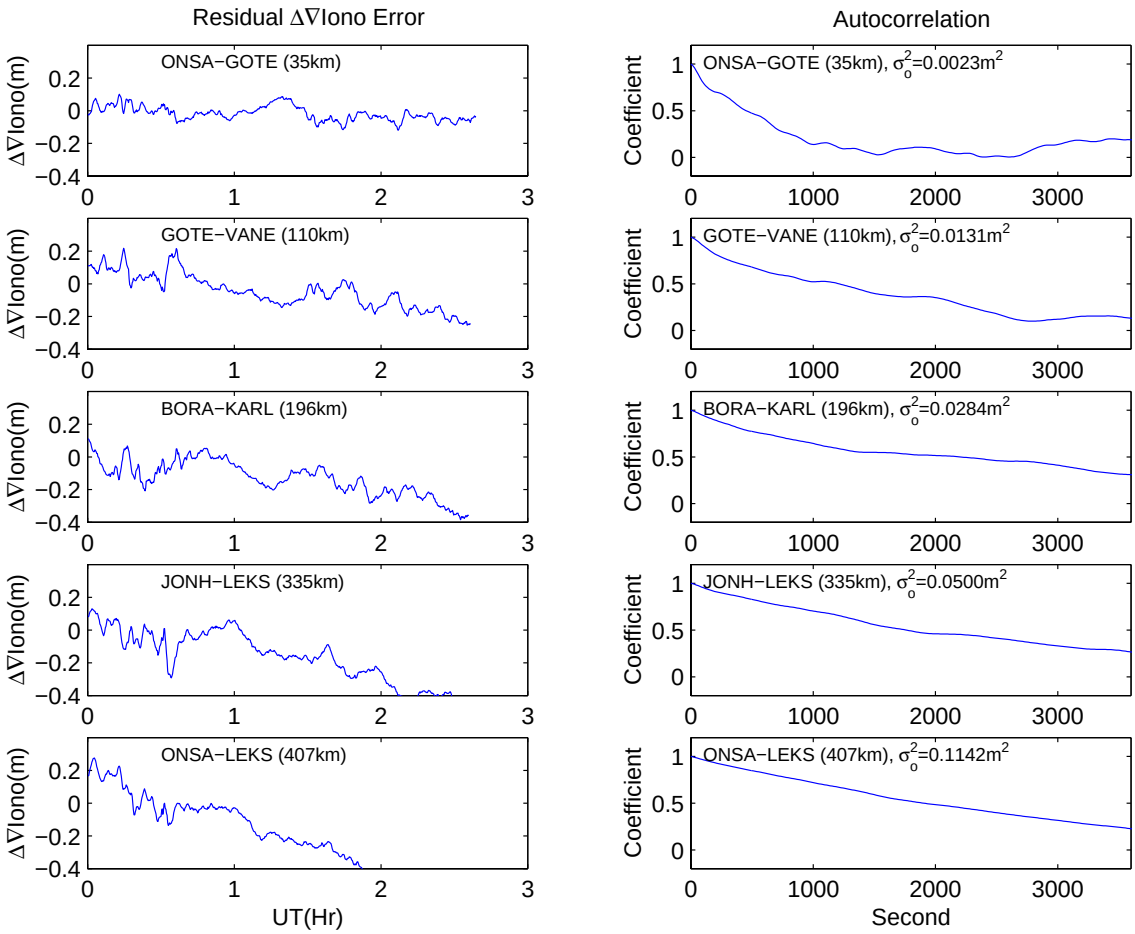

Figure B.2: Autocorrelation of Residual Double Difference Ionospheric Delay Between PRN05 and PRN09, June 21

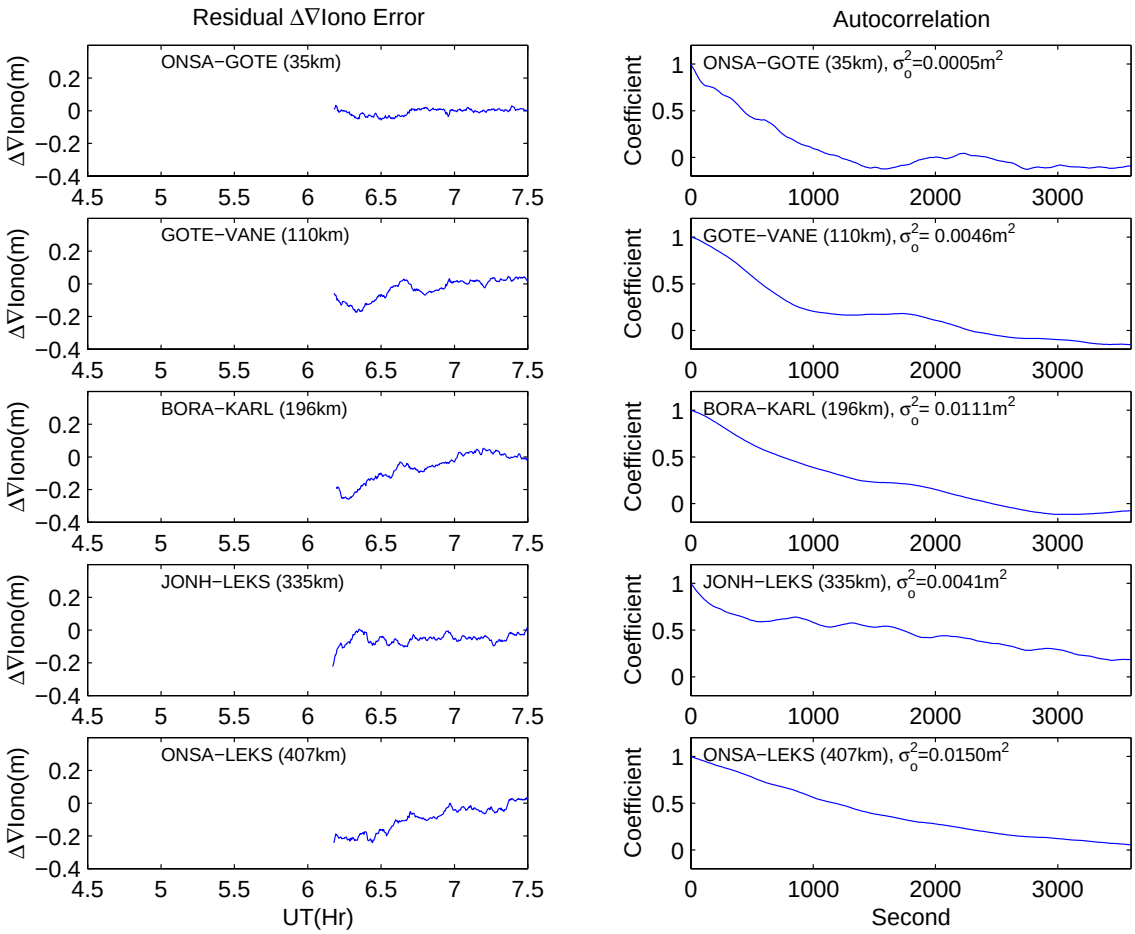

Figure B.3: Autocorrelation of Residual Double Difference Ionospheric Delay Between PRN05 and PRN30, April 7

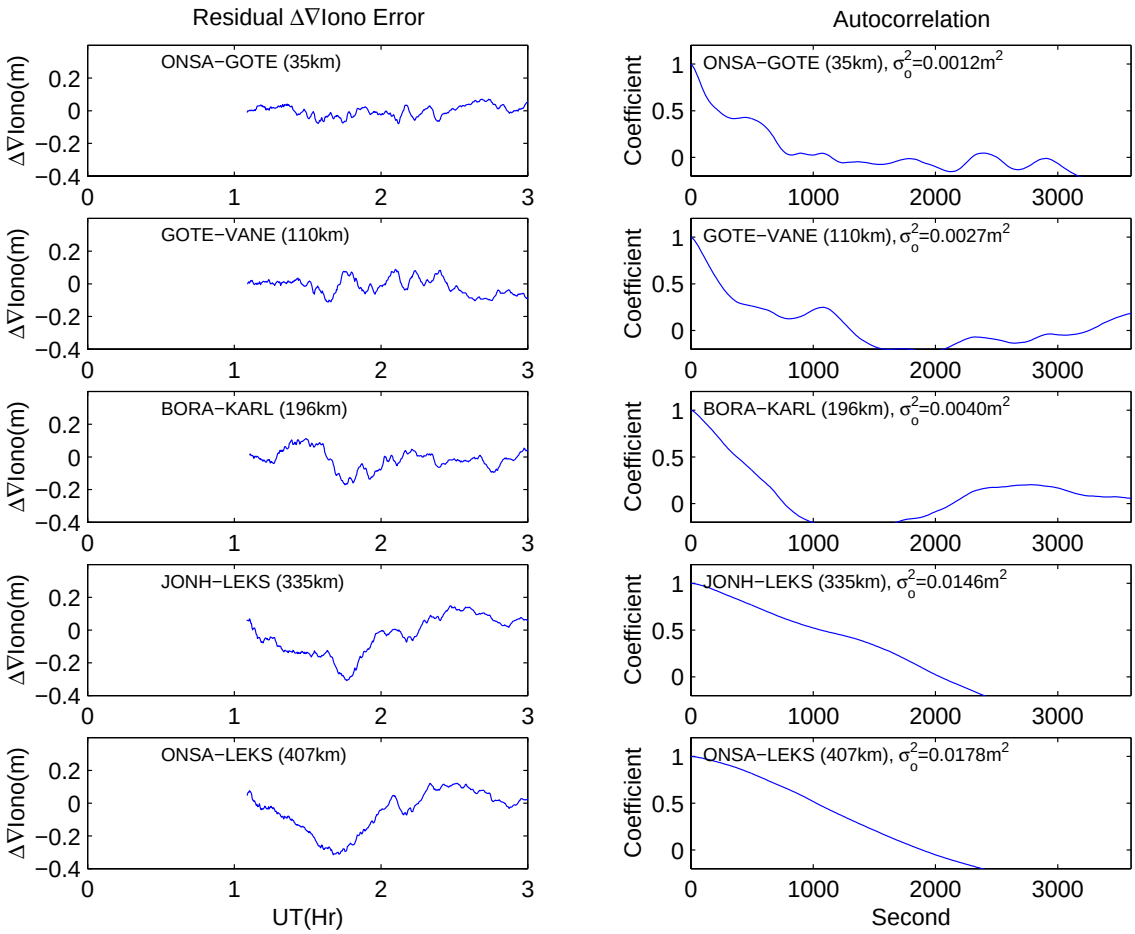

Figure B.4: Autocorrelation of Residual Double Difference Ionospheric Delay Between PRN05 and PRN30, June 21

Appendix C

Sensitivity of Ionosphere Weighting

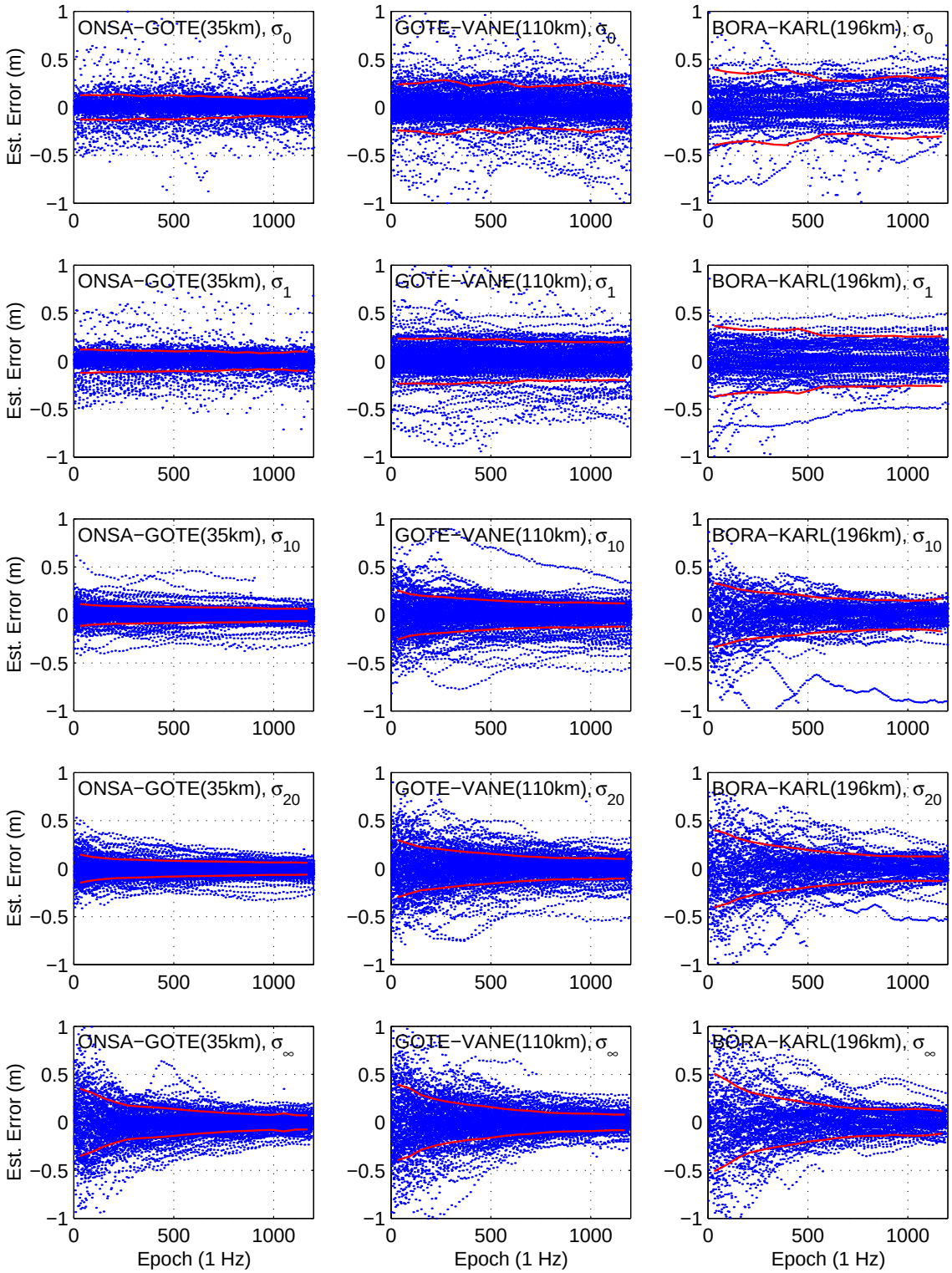

Figure C.1: Double Difference Ionospheric Delay Estimation Error, April 7

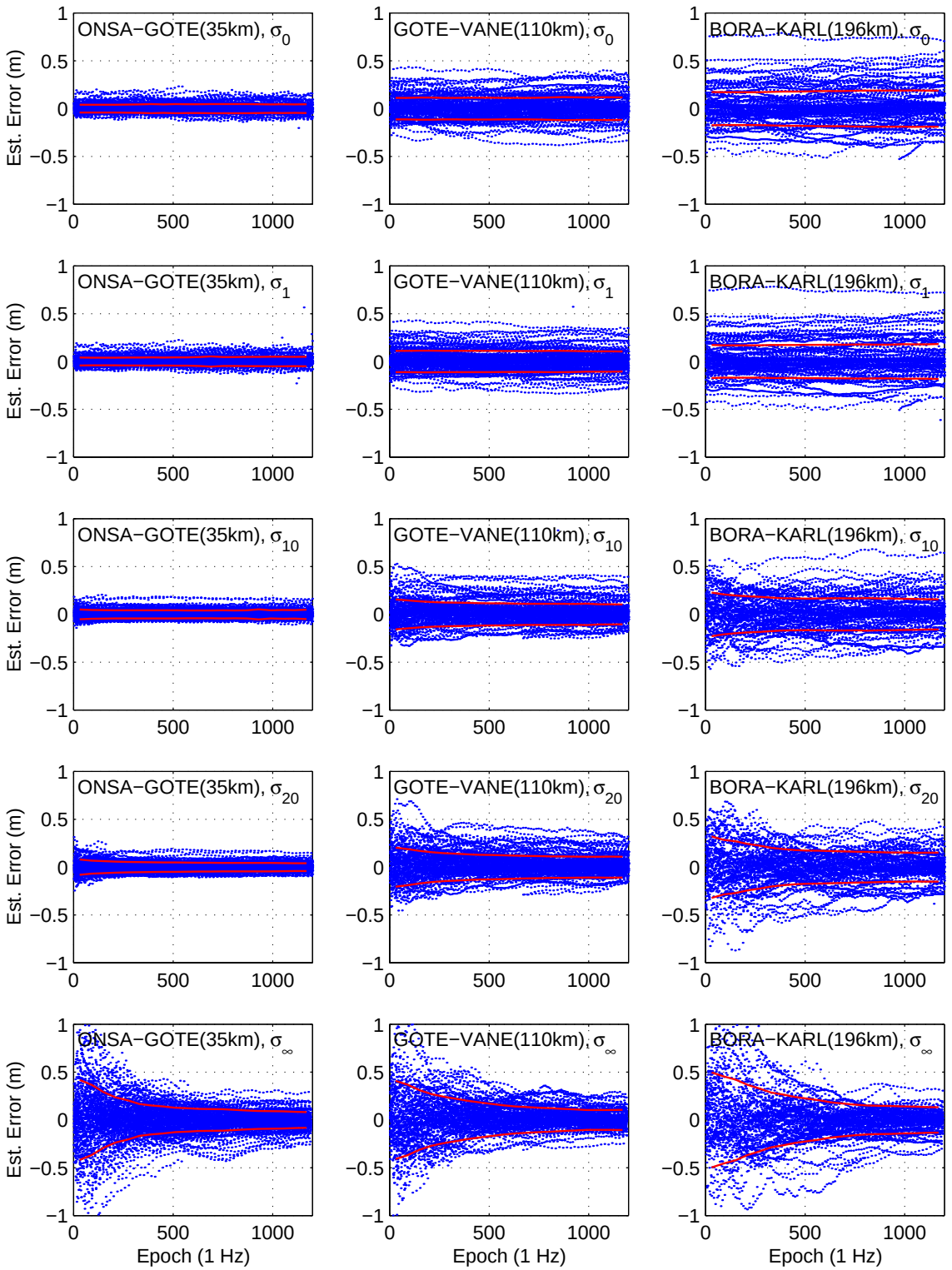

Figure C.2: Double Difference Ionospheric Delay Estimation Error, June 21